Universitat Autònoma de Barcelona

Living Photonics: Lab-on-a-chip technologies for light coupling into biological cells

Tobias Nils Ackermann

Universitat Autònoma de Barcelona

Chemical Transducers Group (GTQ)

Institut de Microelectrònica de Barcelona (IMB-CNM)

Consejo Superior de Investigaciones Científicas (CSIC)

Programa de Doctorat en Física
Thesis submitted to obtain the degree of Doctor in Philosophy

---

Living Photonics: Lab-on-a-chip technologies for light coupling into biological cells

Doctoral Dissertation of:
Tobias Nils Ackermann

Supervisors:
Dr. Andreu Llobera Adàn

and
Dr. Xavier Muñoz Berbel

Tutor:
Prof. Dr. Verònica Ahufinger

September 2017

En Andreu Llobera Adan, Investigador del Consell Superior d'Investigacions Científiques (CSIC) a l'Institut de Microelectrònica de Barcelona (IMB-CNM) i en Xavier Muñoz Berbel, Investigador "Ramón y Cajal" a l'Institut de Microelectrònica de Barcelona (IMB-CNM)

CERTIFIQUEN:

Que la present memòria titulada "Fotònica viva: Tecnologies lab-on-a-chip per l'acoblament de la llum en cel.lules biològiques" ha estat realitzada sota la seva direcció per Tobias Nils Ackermann, Màster Universitari en fotònica per la Universitat Autònoma de Barcelona, la Universitat de Barcelona i la Universitat Politècnica de Catalunya.

Bellaterra, Barcelona
Agost 2017

Andreu Llobera Adan

Xavier Muñoz-Berbel

Abstract

This dissertation encompasses our research on Lab-on-a-Chip (LoC) technologies enabling light coupling into biological cell layers like bacterial biofilms or monolayers of eukaryotes, with the aim of making the cells act as *living photonic* components in the dual role of optical transducer and reporter. The concept of living photonics suggests a host of possibilities in terms of contactless and minimal invasive monitoring of biological processes based on a self-referenced spectral response over time. The implementation of such living photonic elements however presented a very multifaceted challenge, ranging from biological aspects over numerical simulations and optical design, advancements in low-cost micro-fabrication and adaptation of novel materials for PhLoC fabrication and cell culture to optical interfacing and data processing. In particular, we focussed on monitoring bacterial biofilms and mammalian cell monolayers for their relevance in public health. Bacterial biofilms are a major risk due to their ubiquity, resistance to biocides and dynamism and therefore require an intensive control, for which miniaturised and affordable instrumentation would be ideal, very few though is available. Cell monolayers on the other hand are studied extensively in relation with chronic conditions like cardiovascular diseases or diabetes,

Our contributions regarding optical interfacing focus on robust and standardised optical connections to and from a PhLoC using a low-cost fast prototyping approach based on CO_2-laser processing. In particular, careful characterisation of poly-methylmetacrylate (PMMA) laser machining allowed reliable 'plug' connections to standard *SMA* fiber-optics connectors, which were benchmarked against commercial counterparts and applied to light coupling in thin film polymeric waveguides in a high Signal-to-Noise ratio (SNR) PhLoC configuration. Here, optical simulations were mainly employed in the design. In addition, we developed a modular software interface for integral control of laboratory equipment based on the cross platform and open source programming language Python. Besides taking care of the rather extensive data processing implicit in long-term spectral monitoring via efficient number crunching modules like Numpy, interfacing with the Qt software development kit proved apt for real time graphical feedback with fast response times.

Our contributions regarding miniaturised monitoring instrumentation of bacterial biofilms focus on integrating photonic components in thermoplastic substrates - in particular commercial grade PMMA - to provide a cheap platform for the study of biofilm colonisation in water distribution systems. By locally modifying the surface in the detection zone, we achieved preferential adhesion and early optical detection of bacteria in static conditions via fiber-optics segments embedded in the modified substrates. For the implementation of prototypes resembling the flux

and pressure conditions in real water distribution systems, we also explored the integration of polymeric waveguides with fluidic channels, successfully implementing novel fabrication strategies for the encapsulation of photolithographically obtained SU-8 structures in PMMA PhLoCs . Using these devices, and exploiting our positive results in terms of optical interconnects and software interface, monitoring of a circulating bacterial population suggested that bacterial surface colonisation can in such circumstances indeed be associated with a distinct spectral response over time.

Last, we investigated the adjustments to the PhLoC paradigm necessary regarding the implementation of the much thinner mammalian cell monolayers as living photonics. Concretely, we focussed our efforts on the numerical evaluation an optimisation of light confinement in thin irregular layers in low-refractive index environments and the development of suitable strategies to couple light to such structures, taking into account the biological constrains, which were much more pronounced here as compared to biofilms. To that end, different materials were studied in terms of compatibility with the established material parameters, available microfabrication techniques and bio-compatibility. Finally, based on the results regarding suitable materials, we applied two of the resulting PhLoC architectures to *in vitro* cell cultures in different stages of differentiation or inflammatory processes, respectively.

Resumen

Esta disertación abarca una investigación en tecnologías Lab-on-a-Chip (LoC) que permiten acoplar luz a capas biológicas celulares como biofilms bacterianos o monocapas de eucariotas, con el objetivo de transformar células en componentes fotónicos vivos adquiriendo un rol óptico dual: transdusor y elemento de medición. El concepto de componentes fotónicos vivos supone múltiples posibilidades en su monitoreo sin contacto y mínima invasión del proceso biológico basado en una respuesta espectral autoreferencial a lo largo del tiempo del ensayo. Sin embargo, la implementación de los ya mencionados elementos fotónicos vivos presenta retos multifacéticos: los aspectos biológicos, las simulaciones numéricas, el diseño óptico, los avances en la microfabricación a bajo costo y la adaptación de nuevos materiales para fabricación PhLOC y cultivo celular en la interfaz óptica y el procesamiento de datos. Particularmente, nos centramos en monitorear biofilms bacterianos y monocapas de células de mamífero debido a su relevancia en la salud pública. Los biofilms bacterianos son un gran riesgo a la salud debido a su ubicuidad, dinamismo y resistencia a los biocidas. Razón por la cual requiere un control intensivo, idealmente con disposición de instrumentación miniaturizada. Por otro lado, las monocapas celulares se han estudiado extensivamente por su relación con las afectaciones crónicas como la diabetes y enfermedades cardiovasculares. Nuestras contribuciones sobre las interfaces ópticas se enfocan en conexiones ópticas robustas y estandarizadas desde y hacia PhLoCs, usando un prototipado rápido y económico basado en procesamiento de un laser de CO_2. Una caracterización detallada de Polimetilmetacrilato (PMMA) mecanizada por laser permite crear conexiones ”plug” a conectores de fibra óptica SMA estándar, que se han comparado con sus homólogos comerciales y las cuales son viables para un acoplamiento de luz en guías de onda de capas finas de polímero en una configuración de PhLOC de alta relación Señal-Ruido (SNR). Así mismo, se desarrolló un software modular de interfaces para el control integral del equipo de laboratorio. Este se basó en una el lenguaje de programación libre ”Python”. Además de encargarse del extensivo procesamiento de datos implícito en el monitoreo de un respuesta espectral, la interacción con el kit de desarrollo de software Qt demostró buenos resultados para representaciones gráficas en tiempo real. Nuestra contribución sobre la instrumentación miniaturizada para la monitorización de las capas de bacterias estaba dirigida a la integración de componentes fotónicos en sustratos termoplásticos (particularmente el PMMA). Esto proporciona una plataforma de bajo costo para el estudio de la colonización de superfície en sistemas de distribución de aguas. Al modificar localmente la superficie de la zona de detección, logramos una adhesión preferencial y una detección óptica de bacterias en estadios tempranos de adhesion superficial en condiciones estáticas a través de los segmentos de fibra óptica empotradas en los sustratos modificados. Para la implementación de prototipos que simulen el flujo y las condiciones de presión en los sistemas reales

de distribución de agua, también pudimos explorar la integración de guias de onda de polímero con canales de fluido; poniendo en práctica favorablemente nuevas estrategias de fabricación para el encapsulado en PMMA de estructuras SU-8 obtenidas por fotolitografía. Utilizando estos dispositivos y explotando nuestros resultados positivos en términos de interconectores ópticos y interfaz informática el monitoreo de una población circular bacteriana arrojó que, bajo estas condiciones, la colonización de superficie bacteriana podría ser asociada con una respuesta espectral característica con el tiempo. . Finalmente, se han investigado los ajustes necesarios al paradigma PhLoC para la implementación de monocapas celulares de mamífero como componentes fotónicos vivos. Concretamente, dirigimos nuestros esfuerzos en la evaluación numérica y optimización del confinamiento de luz en capas irregulares de ambientes con bajo índice de refracción y el desarrollo de estrategias adecuadas para el confinamiento de luz en dichas estructuras, tomando en cuenta las restricciones biológicas, mucho más evidentes aquí que en el caso de los biofilms. Con este fin, se estudiaron diferentes materiales tanto en cuestión de compatibilidad con las propiedades previamente establecidas, como las técnicas viables de microfabricación y bio compatibilidad. A fin de cuentas, basados en los resultados de los materiales adecuados, se aplicaron dos opciones de arquitecturas PhLoc a culturas celulares in vitro en diferentes etapas de diferenciación o procesos de inflamación, respectivamente.

Contents

List of Figures

List of Tables

Glossary

ATCC United Kingdom (U.K.), Guernsey, Ireland, Jersey and Liechtenstein, LGC Standards, Queens Road, Teddington, Middlesex TW11 0LY, UK. 70

Dow Corning Corp. Midland, Michigan, USA. 102

Ferreteria Maranges S.A. Ferreteria Maranges S.A., Ctra. De Barcelona,79-83, 08290 Cerdanyola Valles, Barcelona.. 32, 52, 56

IMB-CNM Institut de Microelectrònica de Barcelona (IMB-CNM, CSIC), Campus UAB, Cerdanyola del Vallès (E-08193), Barcelona, Spain.. 25

JD PHOTO DATA Photodata House, Knowl Piece, Wilbury Way, Hitchin, Herts SG4 0TY, United Kingdom. 33

MicroChem Corp MicroChem Corp, 200 Flanders Road, Westborough, MA 01581. 32, 52, 102

Microplanet Laboratorios, S,L. MICROPLANET LABORATORIOS, S.L. C/ Mercé Rodoreda, 2, 08172 Sant Cugat - Barcelona, Spain. 52

Norland Products, Inc. 2540 Route 130, Suite 100
Cranbury, NJ 08512, USA. 53, 59

Ocean Optics, Inc. Maybachstrasse 11, D-73760 Ostfildern, Germany. 83

PhLoC photonic lab-on-a-chip. i, ii, viii, xi–xvi, 3–7, 25, 27, 28, 30–32, 37, 43, 51, 52, 54, 56, 63, 66–69, 81, 83, 84, 91, 98–101, 110, 112, 114–119, 123, 124

RS Components Ltd. RS Components Ltd. Birchington Road, Corby, Northants, NN17 9RS, UK. 32

SÜSS MICROTEC AG SÜSS MICROTEC AG, Schleissheimer Str. 90, 85748 Garching, Germany. 33

SCHOTT Suisse SA SCHOTT Suisse SA, Yverdon, 2, Rue Galilée, 1401 Yverdon-les-Bains VD, Schweiz. 32

SDK software development kit. 31, 47

Sigma-Aldrich Co. LLC Sigma-Aldrich Quimica SL, Madrid, Spain. 66

SU-8 Negative tone photoresist developed by IBM. 12

Thorlabs, Inc. Thorlabs GmbH, Dachau/Munich, Germany. 52

Abbreviations

CWI Chip-to-World Interface. 30–33, 36, 81

EPS extracellular polymeric substances. 49, 73

LoC Lab-on-a-Chip. i, 2–8, 13, 25, 29, 30, 89, 90, 102

MEMS micro electromechanical systems. 2, 9, 13, 101
min minute. 173–175, 177
MY-polymer MY-polymer. 174–177

PDMS poly-dimethylsiloxane. 3, 6, 89, 90, 174–177
PEB post exposure bake. viii, 11, 12, 33, 57
PET Poly-ethylene terephthalate. xiv, 103
PL photolithography. 10, 13, 14, 56, 57, 62, 94
PMMA poly-methylmetacrylate. i, ii, 15, 32, 33, 52, 70, 73, 90, 124
PoC point-of-care. 3, 7

rpm rotations per minute. 11, 12

SB softbake. 33
sec second. 173, 176, 177
Si silicon. viii, 3, 9–11, 15
SNR Signal-to-Noise ratio. i

TIR total internal reflection. ix, 6, 20, 21, 84, 101, 116

UV ultra-violet. 10, 12, 174, 175, 177

WG Waveguide. 31–33, 82

Colophon

This document was typeset using the XeTeX typesetting system created by the Non-Roman Script Initiative and the memoir class created by Peter Wilson. The body text is set 12pt with the Libertinus font family, which is a fork of the Linux Libertine and Linux Biolinum fonts and is available under the terms of Open Font License version 1.1. Most of the drawings are created using Inkscape, most plots were created using the Matplotlib graphics environment by John Hunter [Hunter, 2007].

Introduction 1

This chapter is intended to provide the reader with the tools and fundamentals necessary to understand and judge adequately the reasoning and motivation behind the different approaches towards that end and the technological decisions made in the course of this research. After shortly stating the motives for which this line of research was started and giving a brief historic context, we will dive into the 'state of the art' of the research realized previously in this department and the related available technologies. We then proceed with some fundamentals of light-matter interactions, spectroscopy and light guiding, which lead to more specific considerations concerning the implementation of living photonics.

1.1 Motivation

The possibility to create miniature devices containing (at least some of) the functionalities of an entire chemical and biological laboratory has fascinated many researchers since the first mention of the concept. Over the last two decades, a multitude of such Lab-on-a-Chips have been proposed based on different technological tools and mostly aimed at very specific functions, i. e. acting as chemical and bio-chemical reactors. As of 2014, the by far most prominent field of applications was *cell biology* [Sackmann et al., 2014]. Despite the technological achievements, the transition from proof-of-principle experiments to real applications with a tangible impact on biomedical research or even industry is all too often lacking [Blow, 2009, Becker, 2009, Mark

et al., 2010, Volpatti and Yetisen, 2014]. On the one hand, this may be due to the fact that although electro-chemical, impedance and optical sensors are very promising candidates for direct integration of detection schemes into microfluidic networks, only few LoCs actually integrate a complete analytical transduction mechanism. Instead, most still rely heavily on bulky external equipment. On the other hand, although 'microfluidic methods may in some cases be technologically superior to traditional assays, they are often only iterative improvements on methods that already exist' [Sackmann et al., 2014]. If the LoC device merely replaces the specimen holder in a time-tested routine assay, in day-to-day laboratory work the added complexity in handling is simply not justified.

Sackmann et al. [2014] identify in their review *'The present and future role of microfluidics in biomedical research'* three main categories of applications, in which microfluidic methods have demonstrable advantages over traditional methods: diagnostic devices for low-resource settings, the rapid processing of biofluids for research and clinical applications and more physiologically relevant in vitro models for drug discovery, diagnostics and research applications. The efforts summarized in this thesis were mainly directed towards the latter scenario.

Cell cultures in microfluidic channels have been given increased attention in recent years due to the possibility to achieve more physiologically relevant conditions, e. g. controlled flow profiles and shear stresses, as compared to the macroscale solutions. Under the concept 'organ on chip', interconnected in vitro models combining several interacting cell types in a microfluidic platform are proscribed great potencial 'for the investigation of basic mechanisms of organ physiology and disease' [Bhatia and Ingber, 2014].

In this context, integrated photonics present a unique tool for contactless and minimal invasive interrogation of cultured cells and their responses to environmental cues. Further, implementing cell layers as active parts of the integrated optical transducers may provide specific and quantitative information about cell-cell contacts and cell-layer height and thus add an unprecedented component to the currently mostly visual feedback.

1.2 Historic context

Miniaturisation science or microfabrication originated in the semiconductor industry and integrated circuits, making use of technological advancements like photolithography to create the first micromechanical systems, from then on referred to as micro electromechanical systems (MEMS),

Later in the early nineties and starting with the work of Manz et al. [1990], those miniaturisation processes in silicon and especially glass were adopted to create novel tools for analytical chem-

istry. Joining several steps of an analytical assay on a small substrate, they started the dream of a miniaturised total chemical analysis system (μTas). By confining the liquid phases of the reagents in capillaries with cross-section edge lengths in the micrometer range, now commonly referred to as 'microfluidic channels', they could benefit from low reagent consumption, lateral flow (no turbulence) and consequently purely diffusion driven and highly controlled mixing of the reagents. Due to the small sample volumes involved, reaction and diffusion speed could also be increased compared to standard laboratory procedures. This development eventually led to the concept of LoC, promising compact and portable devices for point-of-care (PoC) testing and field studies, which have been envisioned to have tremendous potential to produce high throughput analytical tools pushing into pharmaceutical and biotech research [Beebe et al., 2002, Haber, 2006].

Indeed, the related market has grown continuously until the present. Today, the 'on chip' integration of laboratory components combined with microfluidics is an extensive and active field of research.

Especially since the introduction of polymeric materials like poly-dimethylsiloxane (PDMS) aside the materials traditionally used in micro-fabrication (i. e. Si and glass), the technological landscape in the field has grown increasingly complex. For fluid transport, a variety of methods, reviewed extensively by Mark et al. [2010] have been developed through integrated components like micro-pumps [Laser and Santiago, 2004, Woias, 2005], -valves [Oh and Ahn, 2006] and -mixers [Hessel et al., 2005, Nguyen and Wu, 2005, Lee et al., 2011]. Recently, paper-based microfluidics [Cate et al., 2015] have again become very popular, where the paper as substrate provides the fluid transport and so supersedes external pumping.

On the sensing side, different detection schemes such as electrochemical [Rackus et al., 2015] or optical measurements [Kuswandi et al., 2007, Mogensen and Kutter, 2009, Estevez et al., 2012] have been validated in proof-of-concept studies, showcasing potential advantages over laboratory tests [Whitesides, 2006, Mark et al., 2010, Pires et al., 2014]

As microfluidic chips are finding increasing use in the optics based detection and analysis of chemical and biological samples, the direct integration of photonic components is of increasing interest. The PhLoC platform developed over the last decade in our group is one example of a simple but robust and effective implementation of integrated optical detection.

1.3 The photonic lab-on-a-chip (PhLoC)

This section is intended not as a comprehensive review, but as a small résumé of the motivation behind the integration of optical transduction mechanisms into microfluidic platforms a well as limitations and remaining challenges. Different approaches found in the literature will be illustrated with a few examples with a focus on the results and efforts invested in this group with regard to PhLoCs. The latter have been published recently as a feature in *Analytical Chemistry* [Rodríguez-Ruiz et al., 2016] and can be reviewed in full reprinted in the appendix A

Many of the concepts and ideas behind the photonic components integrated in LoC platforms in recent years are borrowed from the much earlier development of photonic intergated circuits. In 1977, *Tien* and co-workers already published a comprehensive review about integrated photonic elements discussing theoretical descriptions as well as different fabrication strategies for a number of components including integrated waveguides, light sources, grating- and prism-couplers [Tien, 1977]. In the very beginning of said work they state that 'the integration of components has two goals: One is to apply thin-film technology to the formation of optical devices and circuits. The other is the integration of a large number of optical devices on a small substrate, so forming an optical circuit reminiscent of the integrated circuit in microelectronics.' The recent developments in PhLoCs have added another goal to this endeavour; *providing new functionalities and portability in an ambit which traditionally relies heavily on expensive and bulky laboratory equipment.* Apart from the technological innovation implicit in the adaptation and integration with soft-lithographic polymer processes, the main novel aspect in the development of PhLoCs has been their application to sensing and monitoring of biological processes in applications like bio-assays and environmental studies.

Optical detection schemes have the advantage to be non-invasive, easy to sterilize and potentially highly sensitive even with short integration times. This makes them particularly useful for said applications and the integration of optical/optoelectronic elements with microfluidics has resulted in a new generation of highly sensitive and robust sensors [Mogensen and Kutter, 2009, Estevez et al., 2012, Pires et al., 2014].

A key challenge in using optical detection schemes with microfluidic devices remains the accurate coupling of the incoming light into the microfluidic channel and also the ability to successfully detect the corresponding outgoing optical signal. The majority of the mentioned microsys-

tems use external free space optics [Holmes et al., 2006] or inserted optical fibres [Barat et al., 2010, Golden et al., 2009, Rodríguez-Ruiz et al., 2016], for illumination and detection. While active components like photo-diodes promise fully incorporated detection and readout, such integration with the microfluidic platform is technologically challenging and expensive and in most examples [Horváth et al., 2005, Balslev et al., 2006, Wang et al., 2009, Llobera et al., 2015, de Cesare et al., 2015] either light-source or detection remains 'off-chip' [Kuswandi et al., 2007] or needs external stimuli (e.g. pumping lasers) for the integrated units to work. Alternatively, the integration of passive photonic elements offer greatly simplified fabrication processes, as photonic and fluidic components can be defined in the same step and using low cost materials and processes. They hold however the disadvantage of relying on additional external equipment for in-coupling of light and retrieving the gathered information.
The degree of integration reported in the literature varies from single on-chip components to fully integrated devices comprising all the photonic components necessary for an optical sensor, i. e. light-source, optical transducer and photo-detector. For the sake of simplicity, any LoC device comprising on-chip integrated optical components facilitating or ensuring accurate light coupling into microfluidic channels will be called PhLoC from this point forward. The following paragraphs will be mainly dealing with passive integrated photonic elements.

Integrated lenses and mirrors.

Developments in the area of integrated lenses have demonstrated improved illumination, focusing or collimation in a microfluidic channel, which in turn facilitates enhanced optical signal detection. Most examples have been fabricated in polymers using simple one-step photolithography, moulding or stamping, where the optical alignment with the microfluidic channel(s) is achieved at the device fabrication stage [Camou et al., 2003, Rodríguez-Ruiz et al., 2016, Hsiung et al., 2005, 2009]. Lenses located externally to the microfluidic channel are preferred as they do not interfere with microfluidic flow.
Camou et al. [2003] integrated in plane lenses with microfluidic channels to focus from the end of optical fibres inserted in separate channels for optical illumination and resulting signal collection in a PDMS microfluidic chip. Hsiung et al. [2005] have demonstrated a similar technique in a PMMA based chip. Barat et al. [2010] reported a technique based on direct photolithography in SU-8 with an integrated lens and multimode optical fibres for signal excitation and collection to perform flow cytometry applications on a microfluidic device. Seo and Lee [2004] integrated moulded microfluidic channels and compound in-plane lenses for fibre free lens coupling in a PDMS fabricated chip performed in a single step process.

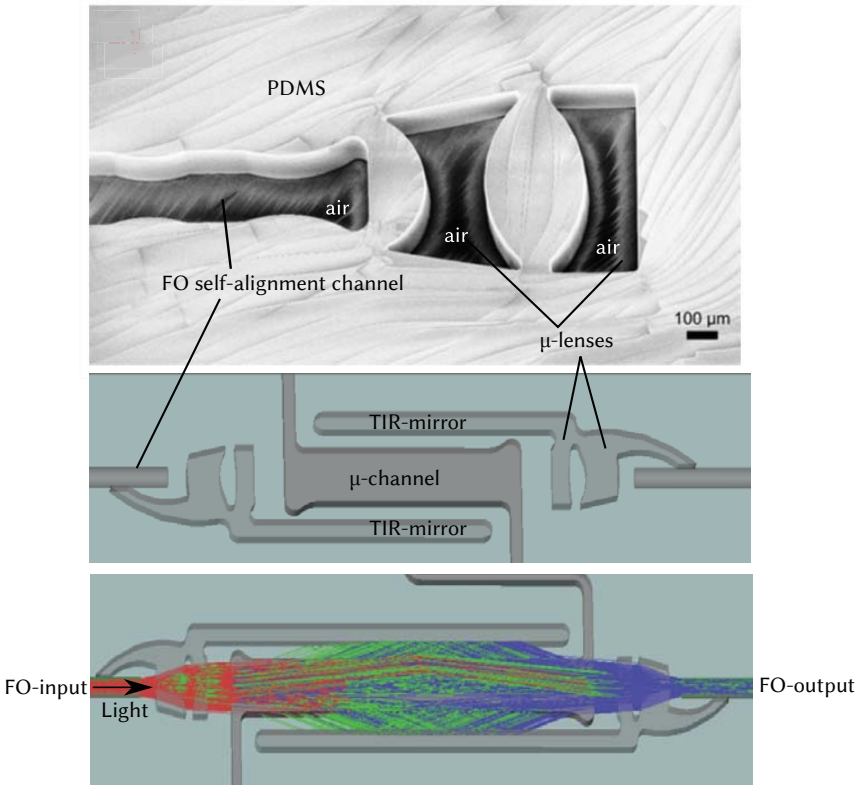

Figure 1.1: Examples of air-PDMS based photonic elements: (a) µ-lenses and self-alignment channel for insertion of pig-tailed fiber-optics ‖citepRodriguez-Ruiz2015; (b) standard configuration of our PhLoCs for colorimetric measurements comprising µ-lenses and TIR-mirrors and in the same structural layer and thus intrinsically aligned with the fluidic µ-channel [Rodríguez-Ruiz et al., 2015a]; (c) Ray-tracing simulation of the configuration depicted in (b), illustrating light propagation guided through the µ-channel by the lens-systems and reflections from the integrated mirrors

The PhLoC as developed and applied in our group [Rodríguez-Ruiz et al., 2016] integrates micro-lenses and -mirrors optimized for spectroscopic and particularly colorimetric measurements of specific target analytes in solution. As depicted in Fig. 1.1, the photonic components are defined by interfaces between the structural material (here PDMS) and well-defined air-pockets inside the latter and as such part of the same structural layer as the microfluidic channels. Air, although often overlooked as functional part in LoCs, serves multiple purposes in this configuration. On the one hand, it provides the simplest possibility of creating a 'compound' structural layer in a single replication step. On the other hand, the high refractive index contrast at the resulting interface can be used to produce lens effects according to a two dimensional design or mirror action based on total internal reflection (TIR) (compare Fig. 1.1).

Various examples of such combinations of pdms-air compound lenses and TIR mirrors have been applied in biochemical sensing applications. For instance, Vila-Planas et al. [2011] used a

combination of cylindrical lenses and focussing mirrors to achieve multiple reflections across a microchannel, thus increasing the optical path while maintaining a small device footprint and sample volume. Rodríguez-Ruiz et al. [2015a] implemented a PhLoC for parallel optical measurements along different path-lengths using optimized micro-lenses for collimation and mirrors to reduce cross-talk between channels.

While well suited for said applications and allowing for simple and low-cost fabrication, this architecture also bears some inherent limitations:

For starters, geometries are defined exclusively in the xy-plane, the third dimension results from the thickness h of the structural layer in the SU-8 master (compare 1.5.1). This locks focussing effects of so defined photonic components ’in plane’. Light whose propagation direction has a non-zero z-component is bound to vanish somewhere along the predefined path. Secondly, the insertion of pig-tailed fiber-optics into the chip (via self-alignment channels) for light in- and out-coupling in turn restricts h to the diameters of commercial fiber-optics. Note that this implies the predetermination of the height of microfluidc channels as well. Lastly, due to the fiber-optics geometry, the optical input presents a gaussian distribution centred in the middle of the channel so that the effective light intensity along the channel-walls is small compared to the total input intensity.

While conventional in plane lenses are attractive due to their design flexibility and simplicity, losses due to diffraction and scattering (which are strongly dependent on the lens system configuration and design) must also be carefully considered. Rodríguez-Ruiz et al. [2017] recently compared light propagation along microchannels of different lengths with and without implementing integrated lenses for beam collimation, finding that for short path-lengths the optical losses produced by the additional interfaces of a lens system outweigh the advantages of a collimated input beam.

1.4 Bottleneck ‘micro to macro interface’

One consequence of the diversity in the technological landscape of LoC is the arising difficulty to bring a successful LoC design from the proof-of-concept stage to a real application. In line with the initial vision, a LoC device would be at its most valuable in a PoC setup with the added value of real portability of laboratory assays. Since microfluidic devices are often only used a few times, – typically only one to avoid cross contamination –, ’it would be desirable to easily insert (or replace) them in a holder (the ’interface’), where the fluidic, optical and maybe even electrical connections are made without any active alignment by the user’. [Mogensen and Kutter, 2009]

Instead, the usual configuratioon involves a chip with micrometric components arranged in a sohpisticated and bulky external setup with a lot of expert skill and knowledge of the particularities of the device. The main obstacle regarding practical, user-friendly implementations of LoCs remains the development of robust connections from the device to the outside world (hereafter named 'interface'), allowing effective handling also by non-experts [Fredrickson and Fan, 2004, Mohammed et al., 2015], Regarding fluidic handling, a variety of robust connectors have been reported during the last decade [Fredrickson and Fan, 2004, Wilhelm et al., 2013, van Swaay et al., 2014, Temiz et al., 2015] However, as of yet such efforts have not been rewarded with widespread application. This lack of success may have several reasons. For one, the prototype oriented technologies usually applied in LoC fabrication are in most cases not quite prepared to produce a great number of devices with comparable performance. An 'industry standard' in terms fabrication as a counterpart to the CMOS process in the semiconductor industry is of yet far from reality and PDMS, although the by far most widely used material in the field, has increasingly earned critical reviews in recent years, especially due to the difficulties in up-scaling it presents. Accordingly, the technology transfer to more large scale applicable materials and technologies has in many cases been either neglected, beyond the scope of the research, too expensive or plainly not possible due to the specific properties of the materials involved in the prototype.

1.5 Microfabrication

Microfabrication, also called micromachining or MEMS originated in the semiconductor industry and the planar processes used to fashion integrated circuits. Due to the strong focus on this area of expertise and the vast cleanroom facilities present at Institut de Microlectrònica de Barcelona (IMB-CNM, CSIC), a range of microfabrication tools was ready at hand for the realization of this thesis. The present chapter is intended to provide a general introduction to the microfabrication techniques employed in this work as a reference for the following chapters.

1.5.1 Cleanroom processes

This section is dedicated to the micromachining techniques employed for this thesis that were carried out in the cleanroom. The description starts with a brief definition of some terminology which will be used frequently in the following chapters and should therefore be introduced initially. Further, it is restricted to those techniques that were actually applied in this work and therefore not a comprehensive one. The interested reader may refer to [Szulczewski et al., 2009, Que, 2008] for more information.

The term microfabrication defines a regime of device fabrication, where at least one dimension of a structural device feature is in the micrometer range. In this size regime, contamination by a dust particle can already lead to failure of the fabricated device. A cleanroom is a space with controlled temperature and air humidity conditions, as well as extensive air particle filters, implemented to provide controlled process conditions and to minimise contamination of devices.

Growth and deposition of thin layers

Thin layers are the principle building blocks in MEMS technology. The first and most basic process step in miniaturization science is therefore the growth or deposition of a thin layer of material. Thermal oxidation of Si is the most common example for controlled layer growth. Silicon oxidation occurs already at room temperature, creating an approximately 2 nm thick native SiO_2 layer on the surface. By heating a silicon wafer to temperatures between 600°C and 1250°C in a stream of steam or in wet or dry oxygen/nitrogen mixtures, further diffusion of oxidant through the already present surface oxide to the silicon interface can be achieved, so that far thicker oxide layers can be formed. The oxidation rate then is a function of various factors

like temperature, concentration of oxidants at the interface and oxide thickness which is very well studied [Szulczewski et al., 2009]. Thus, by controlling the growth time for a given set of gas flows and temperature, thermal oxide layers of very well defined thickness and composition can be grown on silicon wafers.Although this is considered an additive process, it should be mentioned that the oxide growth consumes part of the silicon bulk as indicated in Fig. 1.2. Concretely, the amount of consumed Si is 46 % of the final oxide thickness [Szulczewski et al., 2009].

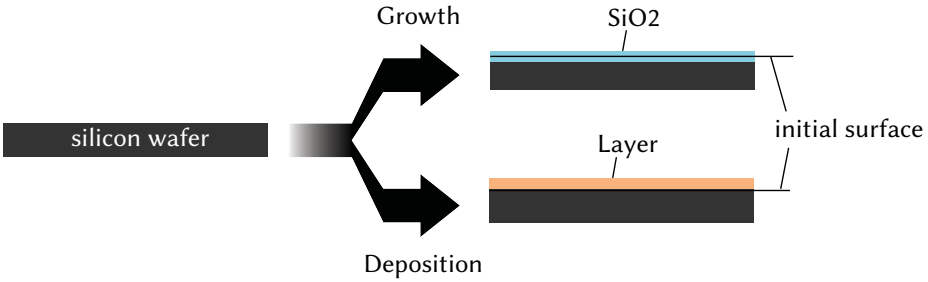

Figure 1.2: Schematic of growth opposed to deposition of layers.

In contrast, the term 'deposition' of a layer will in the following refer to the addition of a film of material without altering or reducing the thickness of the bulk of the substrate. There exist a number of techniques for film deposition ranging from depositing single atomic layers to hundreds of micrometers of material. The one most relevant for this thesis is called spincoating and will be explained as part of the following section.
As a final remark on layers, we should also differentiate sacrificial and structural ones. While the latter will form part of the final device, the former are only used in intermediate fabrication steps to facilitate construction or patterning of one or more of the structural layers and removed chemically afterwards.

Photolithography

Many top-down miniaturization techniques carried out in a cleanroom, and in particular the wafer-scale *planar* techniques described in this section, start with photolithography (PL). This technique is used to create three dimensional micro-patterns by building them up layer by layer from an initially two dimensional design. The essential process step here is the chemical alteration of selected areas of a thin film of material, usually an organic polymer, by illumination with ultra-violet (UV) light. A material which can be altered in that way is said to be *photosensitive* and is in this context usually referred to as *photoresist*. The irradiation process is called *exposure*. The chemical reaction initiated by the irradiation can be constructive, e. g. result in cross-linking of pre-polymer, or destructive, e. g. causing chain scissions. According to the

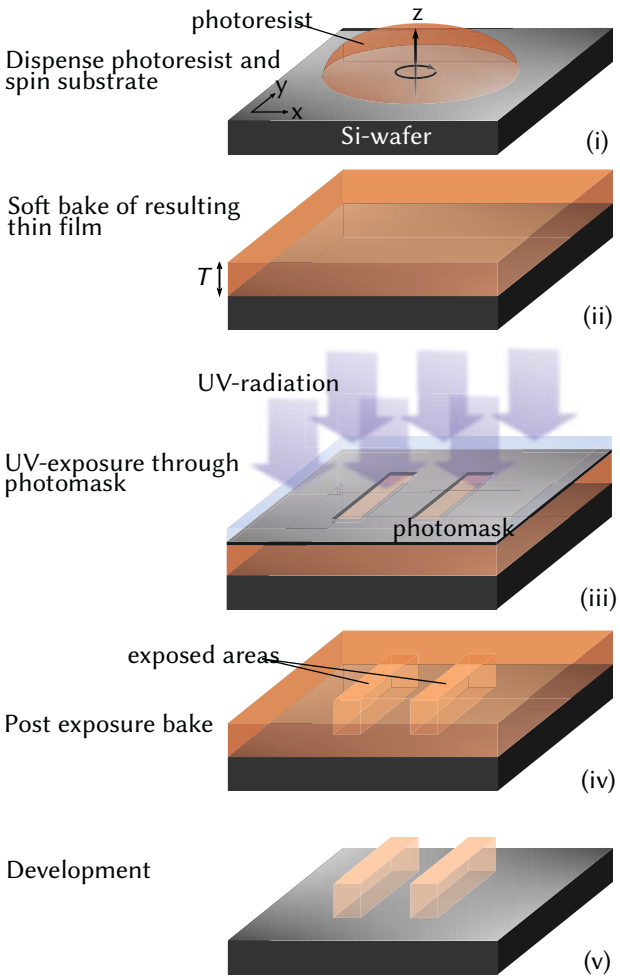

Figure 1.3: Schematic process-scheme of photolithography, i. e. using a negative tone photo-resist: (i) Dispensing resiston substrate and spincoating, (ii) Resist-coated wafer after soft bake, (iii) UV-exposure through photomask aligned with wafer, (iv) Photoresist after exposure and post exposure bake (PEB), (v) Wafer with cross-linked and developed micro-pattern.

type of reaction caused by the UV exposure, the former resists are referred to as *negative tone*, the latter as *positive tone* resists. In order to expose specific areas, a stencil called *photomask* containing the master pattern in form of opaque and transparent areas is placed between light source and photoresist during exposure. Fig. 1.3 summarizes the concrete steps involved in the process using the example of a negative tone photoresist.

At first (Fig. 1.3 i), the resist is dispensed on a clean carrier material, traditionally a Si wafer, from a viscous solution. Subsequently the wafer is spun at high speed in a resist spinner. The arising centrifugal force pushes the solution towards and finally over the edges, such that a uniform thin film is generated, whose thickness T depends on spinning speed, measured in ro-

tations per minute (rpm), and viscosity of the initial resist solution and has been empirically found to follow the expression [Szulczewski et al., 2009]

$$T = \frac{K C^{\beta} \eta^{\gamma}}{\omega^{\alpha}}, \tag{1.1}$$

where K = overall calibration constant, C = polymer concentration in g/100 mL solution, η = intrinsic viscosity and ω = rotations per minute. The exponential factors α, β and γ have to be determined empirically for a given polymer solution and processing conditions such as air humidity and temperature. This information is usually provided along with the photoresist solution in form of a *spincurve* $T(\omega)$. However, eq. 1.1 illustrates that controlling the processing conditions is quite crucial to guarantee a predictable, precise result of the *spincoating* process. Note also that with prolonged storage time and use of the resist solution, solvent evaporation leads to an increase of C and thus the effective thickness after spincoating may deviate from the expected despite otherwise perfectly controlled conditions.

Once the photoresist has been spun onto the substrate, it has lost the gross of its solvent content. To remove the remaining solvents and reduce stress in the film, it is subjected to a heat treatment of (75 to 100)°C . This *softbake* also improves adhesion to the substrate.

The resist-coated wafers (Fig. 1.3 ii) are then transferred to an exposure system comprising a UV lamp providing uniform illumination with well-defined intensity ($W \cdot cm^{-2}$) across the wafers and the means to align them with a photomask. Once wafer and photomask are aligned (compare Fig. 1.3 iii), the photoresist is exposed to the UV radiation during a specific time interval, which depends on resist thickness T and substrate reflectivity. The incident light intensity multiplied by exposure time is called *dose* D ($J \cdot cm^{-2}$). In the case of a *negative tone* photoresist as for instance SU-8 [Lee, 1995], the exposed areas (see Fig. 1.3 iv) undergo a polymerization reaction resulting in cross-linking of the structures. In the specific case of SU-8, cross-linking is achieved by photo-induced Lewis acid generation during UV exposure, which leads to a cationic polymerisation chain-reaction in the resist, rendering the exposed areas insoluble [Que, 2008]. The completion of the chain-reaction is ensured by a second heat treatment of (75 to 100)°C , the so-called *post exposure bake (PEB)*. Subsequently, the latent image formed during exposure is *developed* by immersing the wafer in a solvent for a timed period. During development, the unexposed resist areas are removed as shown in Fig. 1.3 v in the case of a negative tone photoresist, so that the developed pattern represents the negative topology of the one contained in the photomask. Contrariwise, exposure of a positive tone photo-resist results in removal of the exposed portions of the resist during development. Using organic solvents usually induces some swelling in - especially negative - resists, which weakens the adhesion to the substrate. An optional *hard bake* at 120°C concluding the photolithography ensures complete removal of solvent

rests and promotes adhesion of the remaining resist areas. Also, the hardness and thereby the chemical resistance of the film is improved during hard baking, which can be advantageous for subsequent processes.

Pattern transfer: Bulk micromachining

A typical process following PL in the traditional MEMS technology is a transfer of the pattern previously created on the surface of the substrate into the bulk of the substrate itself. The techniques employed to achieve this are commonly summarised with the term *bulk-micromachining*. For bulk micromachining of silicon a variety of methods, which are described at length in [Szulczewski et al., 2009], are available and well established as part of the traditional CMOS processes. For the scope of this thesis, the two etching variants depicted schematically in Fig. 1.4 will suffice to understand some of the particularities. The general principle is the same for both; the patterned substrate, with the pattern now acting as a mask for the subsequent step, is submitted to a chemical reaction that degrades the exposed surfaces. The latter is called *etching* and is governed by several factors. The first one is the *selectivity* of the reaction, which describes the ratio in which the etchant degrades the substrate as compared to the mask material. The second factor is the *directionality* of the etching. The schemes in Fig. 1.4 represent the two extreme cases of isotropic etching on the left and the contrary, directional (anisotropic) etching, on the right. A typical example of an isotropic process is wet chemical etching, where the etchant is applied in form of a liquid, which corrodes the surface at all areas exposed to it with the same rate. Using dry etching methods like plasma etching it is possible to achieve a high degree of anisotropy by combining the chemical corrosion of the material with a pysical attack, i. e. bombarding the surface with a beam of electrically accelerated ions to create damage in the surface and thus facilitate the access for neutral plasma etchant species. At the same time, the volatile reaction products can be extracted by vacuum pumping. In the schematic representation a highly selective etching process is assumed in both cases, such that only the 'material to be etched' is affected by the process. As a result, the reaction stops in depth upon reaching the underlying 'unetchable layer'. After the etching process, the masking layer is removed by a suitable solvent or an additional etching process, which now needs to be selective towards the mask material. This last step of the pattern transfer is called *resist stripping*.

Pattern transfer: Cast moulding

Another technique for pattern transfer, particularly popular in LoC fabrication, is cast moulding or replica moulding [Xia and Whitesides, 1998]. Here, a photoresist structure build up from

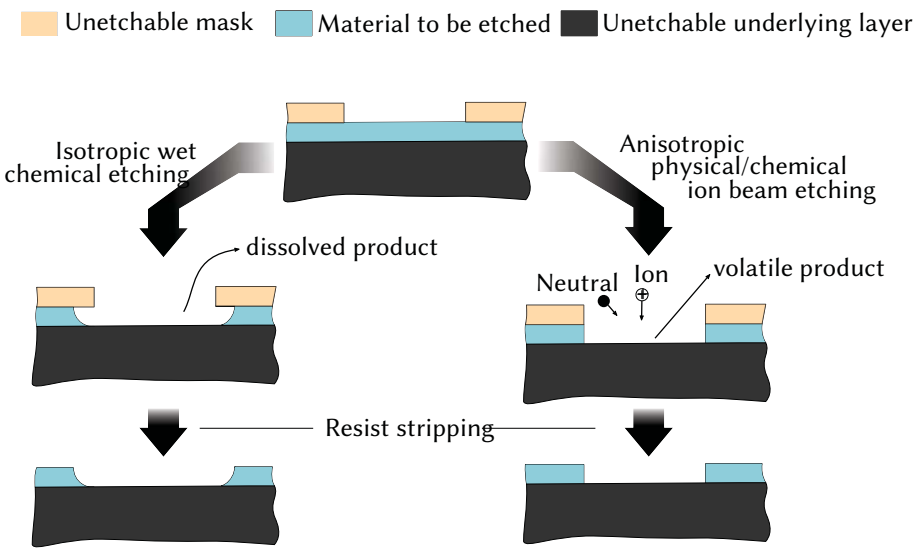

Figure 1.4: Process-schemes of bulk micromachining starting from a wafer pre-patterned with a mask material using photolithography.

one or more photolithographically patterned layers is used as a master for further replication, usually in polymers. A very common structural material for the replica is poly-dimethylsiloxane (PDMS), a transparent silicone rubber which can be cured easily at temperatures between 40°C and 80°C . A scheme of the process is shown in Fig. 1.5. As a common example, we start off with a silicon wafer that has been coated with a thin SU-8 layer exposed without photomask (the so called 'seed layer') and a subsequently deposited structural layer of SU-8, which has been patterned by PL (i). Next, a prepolymer solution is 'cast' onto the master (ii). Dispensed as a viscous liquid, it spreads as far as viscosity and wetting properties of the surface allow. In contrast to the previously explained spincoating process, no external force helps the spreading. Dispensed volume and surface tension of the prepolymer have to be adjusted to assure coverage of the entire master. Once this is achieved, the polymerisation reaction (curing) is initiated - by applying heat in the case of PDMS (iii). After curing, the now solid polymer replica can be peeled off the master ('de-moulding', iv) . As indicated in (v), the resulting three dimensional structure is a negative of the pattern contained in the master. The replication fidelity depends on the feature size, viscosity and wetting properties in each particular combination of master and replica materials. Examples of high fidelity replication of even nanometric features have been demonstrated using this technique. It should however be mentioned that many polymers present some shrinkage upon curing, so that despite geometric fidelity the overall dimensions may be affected. This shrinkage can be greatly reduced by low temperature curing in the case of PDMS, but has to taken into account in the design of the master.

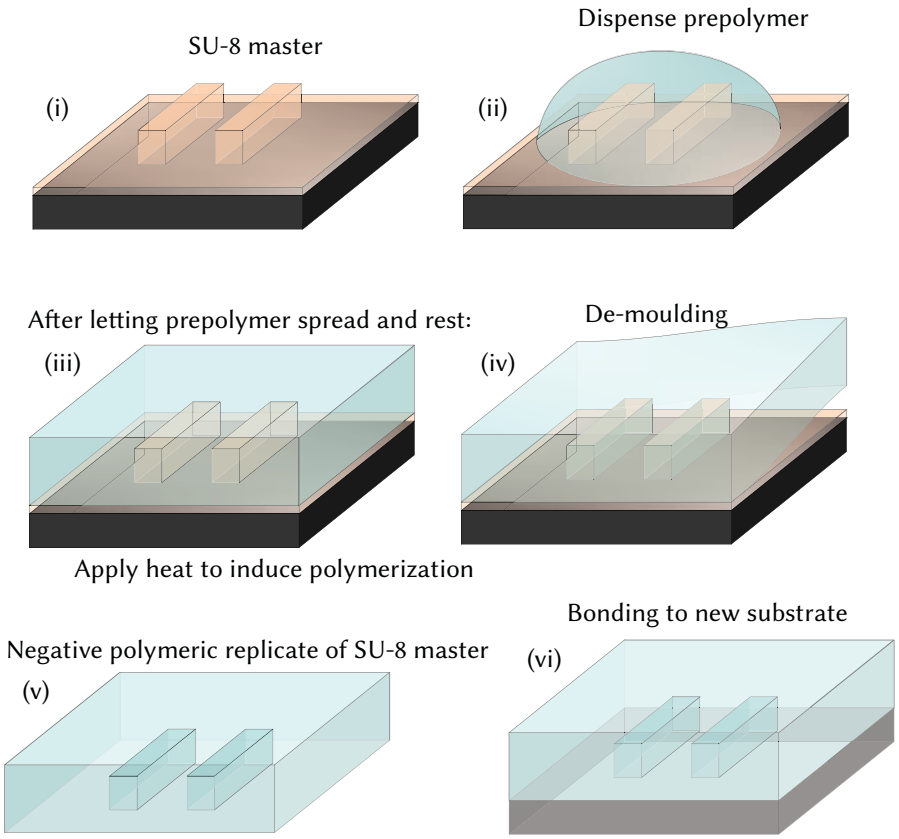

Figure 1.5: Schematic process-scheme of soft-lithography starting from a Si wafer with a thin SU-8 seed layer and a structural SU-8 layer prepatterned using photolithography as described in Fig. 1.3.

1.5.2 'Fast-prototyping'

In a research institution, where the optimum construction materials, fabrication methods and particularly designs for a given application are often 'yet to be determined', fast and flexible fabrication processes present clear advantages over the previously presented well-established cleanroom techniques for protoyping and initial testing. The commercialization of a series of relatively cheap equipments for micromachining of plastics and thermoplastics has made such techniques very popular especially in the academic sector.

Among them, CO_2-laser processing of PMMA combines the attributes low-cost, flexible design and minimum time consumption. Thus it is an ideal method for rapid prototyping in such a context.

CO_2-laser processing.

In usual a setup of a commercial CO_2-laser writer, a pulsed laser beam is focussed unto the surface of a working piece, which results in a large heat deposition in a very localised spot determined by the spot size of the beam. The spot size of a laser beam is defined generally as the minimum beam waist diameter $2W_0$ at $z = 0$. The depth of focus,

$$2z_0 = 2\pi W_0^2/\lambda, \tag{1.2}$$

is defined as the axial distance from $z = 0$, at which the beam radius lies within a factor $\sqrt{2}$ of its minimum value W_0 and directly proportional to the beam waist.

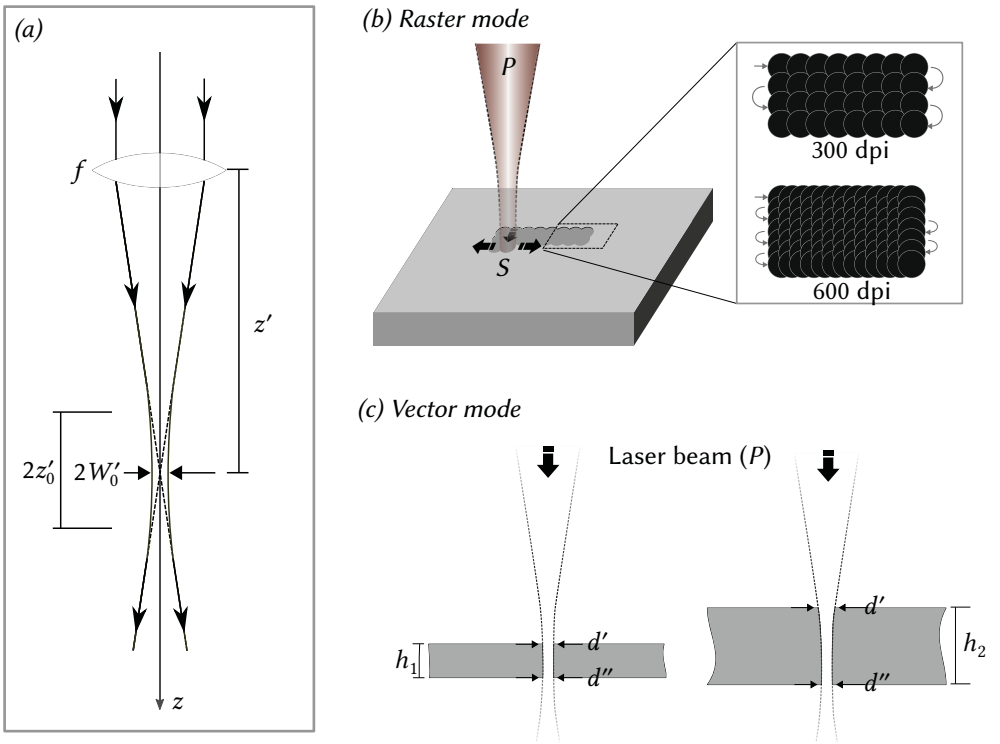

Figure 1.6: Fundamentals of CO_2 laser processing. (a) Parameters of a focussed beam after Stijns and Thienpont [2011]; (b) Characteristics of material removal in 'Raster mode' from the surface of a work-piece; (c) Cutting profiles for material thickness h smaller (left) and larger (right) than the depth of focus $2z'_0$.

If a collimated beam is transmitted through a focussing lens with focal length f as shown in Fig. 1.6 (a), the transmitted beam is reshaped according to the focal length f of the lens to a waist radius

$$W'_0 = \frac{W_0}{\sqrt{1 + (z_0/f)^2)}} \tag{1.3}$$

at a distance

$$z' = \frac{f}{1 + (f/z_0)^2} \,. \tag{1.4}$$

So, depending on the lens mounted in the laser writer, focal distance, beam waist and depth of focus can be limiting factors for certain applications, as will become clear in the following.
In the case of the Epilog 24 Mini employed during this thesis, the principal configuration parameters for the laser writer consist of beam power (P), scanning speed (S), laser pulse frequency (F) and resolution (dpi). Two 'printing' modes are available to the user; 'Raster' and 'Vector' printing. Raster engraving can be best described as high resolution dot matrix printing with a laser. The laser head scans back and forth, left to right, engraving a series of dots as indicated in Fig. 1.6 (b). For a given set of values for P, S, the pulse frequency is adjusted automatically to achieve the desired resolution. The degree of pulse overlapping is determined by the spot size in relation to the spatial density of the dot matrix as shown comparatively for the cases of 300 dpi and 600 dpi. The depth of the engraved profile is determined mainly by the deposited energy, which depends on the beam power P, scanning speed S and the materials absorptivity at the working wavelength. For further reading on these aspects, the reader interested reader may refer to Prakash and Kumar [2015].In 'Vector' mode on the other hand, the laser head follows a continuous trajectory. The beam parameters P, S and F define the impact on the material. The 'Vector' mode is usually used to cut completely through the material, as shown in Fig. 1.6 (c). As a consequence of the limited depth of focus, the linewidth d of the cut may vary along the beam axis. The examples in Fig. 1.6 (c) illustrate on the left the ideal case a material with a thickness $h_1 < 2z_0'$ and positioned properly at the focal distance z', on the right a material with a thickness h_2 exceeding the focal depth of the laser beam and positioned slightly out of focus. The results are a fairly homogeneous linewidth along the cut with $d' = d''$ in the former, an inhomogeneous cut with $d' > d''$ in the latter case.

1.6 Fundamentals of optics and spectroscopy

Light is absorbed and emitted in discrete energy bundles, today known as photons. The different manifestations of this *quantisation* of light have been described mathematically by quantum electromagnetic theory, which envelopes all of the previous 'classical' theoretical descriptions of light [Stijns and Thienpont, 2011]. In many situations though, so many photos are delivered by a beam of light that the discrete character is completely hidden within continuous phenomena [Hecht, 2001], which can be described very well using classical electromagnetic theory. According to the latter, light propagates through space in form of an electromagnetic wave, which is composed of two vectorial fields, the electric ($\vec{E}$) and magnetic field ($\vec{E}$), oscillating perpendicular to the propagation direction. It can be demonstrated mathematically that in general power flow of such a wave is in the direction of the so called Poynting vector $\vec{S} = \vec{E} \times \vec{H}$.

Light propagation in dielectric media. In a dielectric medium, the phase velocity $c = c_0/n$ of the electromagnetic wave is reduced as compared to the speed of light in vacuum, c_0. The factor by which light is 'slowed down' inside a medium is called *refractive index* (n)

$$n = \sqrt{\epsilon/\epsilon_0}, \tag{1.5}$$

where $\epsilon_0 \approx (1/36\pi) \times 10^{-9}$ is the electric permittivity of free space, ϵ that of the dielectric. In general, the electric permittivity of a medium and implicitly its refractive index n changes as a function of the frequency $\nu = c/\lambda$ of the incident electromagnetic radiation. A material is said to possess a homogeneous spatial distribution of n if variations of n occur on a much larger scale than the wavelength of interest (the opposite case will be treated separately later on). The propagation of light inside such a medium and the passage from one medium to another give rise to a series of phenomena relevant to this work, which will be summarized in the following.

Scattering and absorption. Generally, dielectric media are not completely transparent as assumed until now, but contain compositional and structural features affecting the propagation of light in form of scattering or absorption. At the level of atoms and molecules, the incoming electric field interacts with their electron cloud in one of two ways. If the frequency of the wave and in extension the energy of the incoming photons is too small to excite an electron from the ground state to a higher electronic state, the energy is re-emitted in form of another photon with the same frequency. If the incident light is unpolarised, this re-emission occurs in random direction. Light is 'scattered' *elastically*. The mathematical description of scattering phenomena differs according to the size of the scattering species. The size is in this context defined using the characteristic length $x = 2\pi r/\lambda$. Based on that definition, particles much smaller

than the wavelength behave as Rayleigh scatterers. If $x \approx 1$, so-called Mie scattering takes over. Objects with $x >> 1$ act as geometric shapes, scattering light according to their projected area. Contrariwise, if the frequency matches that of one of the atoms or molecules excited states, the incoming photon will be 'absorbed' and the electronic transition takes place. Instead of being released in form of another photon, the absorbed energy usually dissipates in form of thermal energy as the atom relaxes to the ground state.

Refraction and reflection. At the boundary between to materials with refractive indexes n_1 and n_2, part of the light is transmitted across the boundary into the adjacent, the rest is reflected back into the original medium at the same incident angle as depicted schematically in Fig. 1.7 a. To simplify the graphic representation, light propagation is illustrated in form of rays. In this representation, each ray points in the direction of the flow of energy, $\vec{S}$. This simplification, which is a good approximation as long as the objects interacting with our light beam are big compared to its wavelength λ. this model serves well to convey the general ideas. The amount of light transmitted and reflected at the interface depends on the refractive index contrast and the incident angle. Based on these parameters, reflection R and transmittance T coefficients respectively can be approximated using the Fresnel equations. In the special case of normal incidence ($\theta_i = 0$) these simplify to

$$R = (\frac{n_2 - n_1}{n_1 + n_2})^2 \tag{1.6}$$

and

$$T = \frac{4n_1 n_2}{(n_1 + n_2)^2} \tag{1.7}$$

Hecht [2001].The angle θ_t, at which the transmitted beam is *refracted* into the second medium, depends on the incident angle θ_i relative to the interface normal and the refractive indexes n_1 and n_2 of the first and second medium, respectively. This mathematical relationship is described by *Snell's law*:

$$n_1 \, sin(\theta_1) = n_2 \, sin(\theta_2) \tag{1.8}$$

Another implication of eq. 1.8 is that for a ray passing from a medium with refractive index n_1 to a medium with refractive index n_2 and $n_1 > n_2$ there exists an angle of incidence, following called the *critical angle* $\theta_c = sin^{-1}(n_1/n_2)$, at which the refraction at the interface would result in a new propagation direction parallel to the interface as depicted in Fig. 1.7b. Consequently, for angles of incidence greater than θ_c, the same ray will, instead of being split into a refracted and a reflected ray, be totally reflected back into the medium of origin. This process is called TIR.

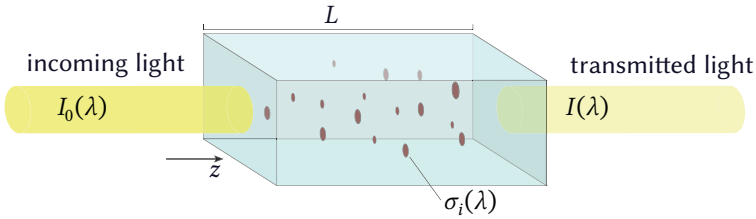

FIGURE 1.8: Schematic of a light beam with incident intensity $I_0(\lambda)$ crossing a medium containing species with a wavelength-dependent attenuation cross-section σ_i and leaving the medium with a diminished intensity $I(\lambda)$.

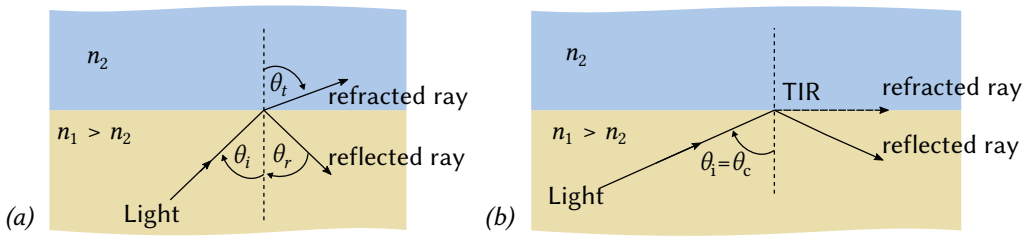

FIGURE 1.7: Refraction (a) and TIR (b) at the boundary between two transparent dielectric media.

Spectroscopy. In a general sense, the term spectroscopy is applied to any technique providing a wavelength (or frequency) dependent measurement of the effects of the interaction of electromagnetic radiation with matter. As all of the previously discussed phenomena are wavelength dependent, spectroscopic measurements can provide a host of information about a given material. The spectroscopic technique most relevant in the context of this thesis is usually referred to as *absorbance spectroscopy* and is based on the well known *Lambert's law*, which describes the transmission of light through a finite length L of material as shown in Fig.1.8. The transmittance at a given wavelength is generally defined as the ratio of the transmitted intensity $I(\lambda)$, i. e. the intensity *after* passing through a length L of the material, and the initial intensity $I_0(\lambda)$:

$$T(\lambda) = \frac{I(\lambda)}{I_0(\lambda)} = e^{\int_0^L \mu(z,\lambda)dz}, \tag{1.9}$$

where T is called the *transmittance* of the material sample, L the *optical path length* and μ is the (napierian) attenuation coefficient with

$$\mu(z,\lambda) = \sum_{i=0}^{N} \mu_i(z,\lambda) = \sum_{i=0}^{N} \sigma_i(\lambda) n_i(z), \tag{1.10}$$

where σ_i is the attenuation cross-section and n_i the number density of attenuating species i in the medium. Usually $\mu(z,\lambda)$ is reported with a decadic base as $\mu_{10}(z,\lambda) = \mu(z,\lambda)/ln(10))$ and the

attenuation along the path length L is defined as *Absorbance* A according to

$$A = log_{10}(T) = log_{10}\left(\frac{I(\lambda)}{I_0(\lambda)}\right) = \int_0^L \mu_{10}(z,\lambda)dz. \tag{1.11}$$

1.7 Light guiding

Light can be guided from one place to another by different means (compare Fig. 1.9). Combinations of lenses and mirrors are very commonly used for such purposes in free-space setups on an optical bench. One disadvantage of such assemblies is that partial reflections during refraction at the lens surfaces and partial absorption upon reflection at mirror surfaces can add up to a significant cumulative loss of optical power [Stijns and Thienpont, 2011]. Total internal reflection (TIR) at the interface of two media with different refractive index offers a way of guiding light with minimal losses, as light is 'reflected repeatedly without undergoing refraction' [Stijns and Thienpont, 2011].

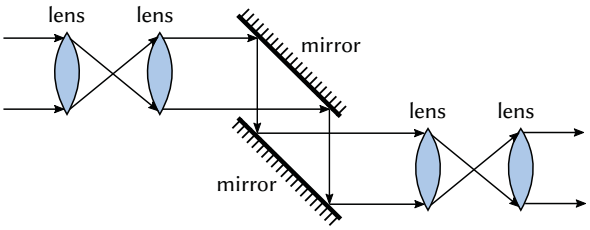

Figure 1.9: Guiding light using lenses and mirrors

Suppose a three layered (transparent) material with $n_{\text{core}} > n_{\text{clad}}$ as indicated in Fig. 1.10. In a structure like this, the centre layer with increased refractive index is called *core*, the adjacent layers are called *claddings*. For light to be guided along the structure as indicated by the rays, several conditions must apply. Firstly, the acceptance angle, the maximum angle at which a ray incident on the core will be totally internally reflected at its first encounter with the core-cladding interface, depends on the difference in refractive index between core and cladding and the refractive index of the outside medium, n_0 as:

$$n_0 sin(\theta_a) = \sqrt{n_{\text{core}}^2 - n_{\text{clad}}^2} \equiv NA. \tag{1.12}$$

NA is called the *numerical aperture* of the lightguide. Once inside the core material, each reflection at the interface between core and cladding induces a phase shift in the propagating wave associated with the ray. As the ray must reproduce itself after every second reflection (*self-consistency condition*), the phase shift induced by travelling along the path length between

reflections must correspond to an integer multiple of 2π. As a consequence, at a given wavelength and lightguide thickness d, propagation by multiple internal reflections only works for a discrete number of propagation angles. These are called the propagation *modes* of the lightguide and the light is said to be *confined* in the z-direction. In this simplified case of one-dimensional confinement, the number M of modes can be estimated based on the previously defined numericalfiber-probe aperture:

$$M_{1D} = \frac{2d}{\lambda} NA. \tag{1.13}$$

In the more general case of two-dimensional confinement, e. g. in a lightguide of rectangular cross-section, this number increases to approximately

$$M_{2D} = \frac{\pi}{4} \left(\frac{2d}{\lambda} \right)^2 NA^2. \tag{1.14}$$

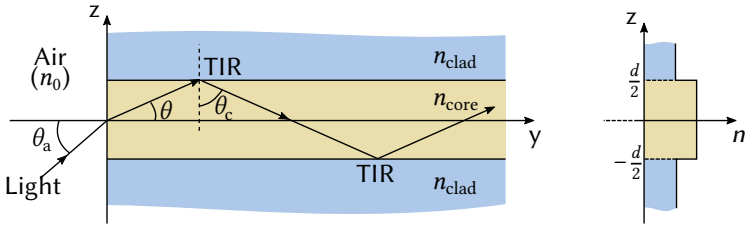

Figure 1.10: lightguiding in TIR conditions.

1.8 Biomaterials as lightguides

As stated in the beginning, the implementation of living biological specimen as optical transducers may provide a host of unprecedented information, as the light transmission would be affected in one way or another if changes in composition and structure occur.

Light guiding in biology has been discovered in various environments. The most inituitive examples are plant optics, which are amply studied and reported [Vogelmann, 1993], and vertebrate eyes [Franze et al., 2007]. Even in the deep sea some species have evolved light guiding structural features acting very similarly to an optical fiber in telecommunication [Aizenberg et al., 2004]. In these examples, the biological systems themselves have evolved the necessary fine structure and refractive index environment to allow coupling and guiding of incident ambient light.

To impose such conditions on a biological system artificially is another matter entirely. Nevertheless, a few examples have been reported. These examples confirm that the minimal conditions to be met to achieve some extent of light guiding in cell layers are first to achieve a biomaterial

as "uniform" as possible, at least in terms of tight intercellular contact, and a higher refractive index of the cells than the surrounding media. Yashunsky et al. [2012] for instance identified waveguide modes coupled into a monolayer of polarised epithelial cells as resonant reflectivity minima in infrared reflectivity experiments as depicted schematically in Fig. 1.11 (a). As they put it, 'several factors conspired to enable the propagation' of these modes: the tight junctions maintained between cells, the cell monolayer featuring a higher refractive index than the aqeous growth medium covering it and the infrared wavelength being of the order of the height of the monolayer. In a quite different approach, Xin et al. [2013] managed to string a number of bacteria by optical trapping between two abruptly tapered fiber probes and thus create a 'biophotonic waveguides' operated with visible and near infrared light (compare schematic in Fig. 1.11 (b)). The optical trapping allows for both tight connections between individual bacteria and the suspension of the entire structure, so that a suitable refractive index contrast between biomatter and water can be taken advantage of to achieve light guiding.

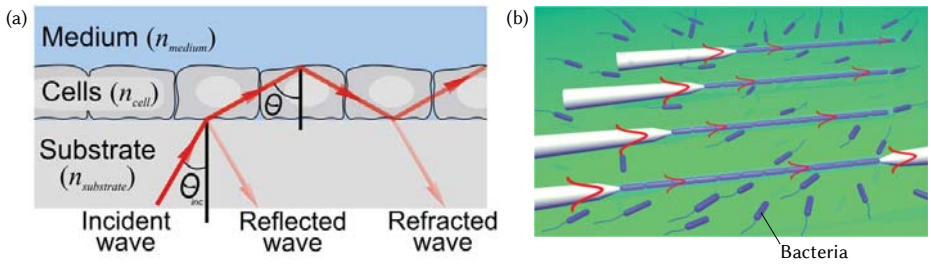

Figure 1.11: (a) Schematic of intracellular leaky waveguide mode propagation in a living cell monolayer, reprinted from [Yashunsky et al., 2012]. (b) Schematic of light coupling and propagation along optically trapped E. coli cells, reprinted from [Xin et al., 2013].

Objectives 2

The main objective of this thesis was the development of LoC technologies enabling light coupling into biological cell layers like bacterial biofilms or monolayers of eukaryotes, with the aim of making the cells act as *living photonic* components in the dual role of optical transducer and reporter. In particular, we focussed on monitoring bacterial biofilms and mammalian cell monolayers for their relevance in public health. Bacterial biofilms are a major risk due to their ubiquity, resistance to biocides and dynamism and therefore require an intensive control, for which miniaturised and affordable instrumentation would be ideal, very few though is available. Cell monolayers on the other hand are studied extensively in relation with chronic conditions like cardiovascular diseases or diabetes

The planning of this thesis was based on the technological know-how of the chemical transducers group (http://gtq.imb-cnm.csic.es/) at IMB-CNM and in particular that of the 'hybrid photonics' department lead by Dr. Andreu Llobera. The ample prior work of this department in the area of PhLoC together with the vast cleanroom facilities present at IMB-CNM provided a host of technological tools and protocols as a starting point to for *living photonics* project.
Unfortunately, the sensing of species settled on the channel-bottom or attached to channel-walls was very challenging in the available PhLoC configurations. The latter however is specifically the expected situation in cell cultures and biofilm colonisation. This project therefore started by developing strategies towards the adequate modification and adaptation of the original PhLoC paradigm for measurement and on-chip monitoring of biological systems, i. e. bacterial biofilms and monolayers of eukaryote cells, with the ultimate goal of implementing them as living pho-

tonic elements. As every biological system has its own structure and requirements for survival, adapted strategies were needed in each case to achieve the latter. For instance, bacterial biofilms may reach a thickness of several hundred of micrometers, whereas an optimistic estimate for the thickness of eukaryote monolayers places the maximum thickness in the range of some hundred nanometers to a few micrometers. As the latter thickness may be of the of a wavelength in the visible light regime, different optical effects manifest in this case than in the case o the biofilms. Another big difference is the robustness of the biological system. While biofilms can form nearly everywhere, eukaryotes and especially mammalien cells are extremely sensible to culture conditions such as pH or temperature. Furthermore, due to the area of application in microbiology and biomedicine the technological solutions had to cope with the need for transport and operation in the framework of corresponding specialised laboratories.

The following formulation of concrete objectives for this work is therefore organised in three blocks:

- *The chip-to-world interface*

    1. Assess the strengths and weaknesses of current photonic lab-on-a-chip architectures and implementations in terms of operation in biological laboratories.
    2. Develop of a physical interface providing robust optical connections, preferably plug&play, enabling long-term installation and on-site monitoring and acting as a bridge between the *on chip* photonic components and standard connectors of external light-sources and detectors.
    3. Explore possible solutions for automation of long term measurements.

- *Biofilms Monitoring*

    1. Develop affordable miniaturised monitoring platform integrating photonic components enabling the light coupling to and from bacterial biofilms.
    2. Study the spectral response of biofilms in different stages of surface colonisation.

- *Confinement in Monolayers*

    1. Assess the requirements for monoayer living photonics from an optical point of view: Numerical simulations
    2. Translate the determined optical requirements into a technological solution in terms of
        - Suitable optical design
        - Adequate materials
        - Bio-compatibility

Thesis overview

The organisation of the thesis is as follows:

According to the objectives defined above, the main body of the thesis is divided in three chapters. The first one, entitled *The Chip-to-World Interface* (Chapter 3), contains the results obtained regarding the development of a miniaturized system facilitating robust optical coupling of light to and from a PhLoC, which is based on a plug&play philosophy, allowing the user to couple

and decouple a photonic device without the need for specific alignment. In addition, a software interface based on the interpreted programming language Python is presented, which bears the possibility of creating a unified front end for the control and automated actuation of different laboratory equipments such as light sources and spectrometers.

The following chapter, entitled *Optical sensing of microbial surface colonization on-chip* (Chapter 4), details the efforts invested in the early detection of biofilms by optical measurements and the development of a PhLoC permitting the formation of a biofilm in flow conditions as connecting element between two integrated polymeric waveguides.

The concluding chapter, entitled *Low refractive index PhLoCs for light confinement in cell monolayers* (Chapter 5), deals with the technological advances required for the successful implementation of cell monolayers as living photonic components and presents several different approaches to that end as well as some preliminary results.

Following that, the general conclusions and arising perspectives are discussed, after which relevant publications derived from this work or elaborated during the course of this thesis are presented. The appendixes further contain additional information related to the aforementioned content chapters, as well as the collection of bibliography.

The Chip-to-World Interface 3

Due to the collaborations with several research groups working in the field of biology and medicine who kindly provided laboratory space and assistance to carry out the measurements presented throughout this thesis, the pending issue of robust optical connections and portable setups became evident right from the start of my research. Therefore I dedicated a good deal of time to explore the possibilities of achieving as much by means of a fast and flexible fabrication technique. In the end I settled on a fast prototyping approach using a CO_2-laser for the fabrication of optical connectors tailored specifically for the measurement configuration at hand. In addition, the need to correct the measurements in terms of the continuously changing ambient light conditions in spaces other than the confinements of an optic laboratory lead to the development of custom made software tools dealing with such problems automatically and 'behind the scenes'. The following chapter deals with the results obtained in both aspects.

3.1 Introduction

The main obstacle regarding a practical, user-friendly implementation of LoCs with any detection scheme remains in the development of robust connections from the device to the outside world (hereafter named 'interface'), allowing effective handling also by non-experts [Fredrickson and Fan, 2004, Mohammed et al., 2015]. Regarding fluidic handling, a variety of robust connectors have been reported during the last decade [Fredrickson and Fan, 2004, Wilhelm et al., 2013, van Swaay et al., 2014, Temiz et al., 2015]. Companies like *microfluidic ChipShop*, *Cellix*

or *Dolomite* [Blow, 2007] offer entire series of already functionalised LoCs with fluidic connectors directly attached and compatible with their respective pumping systems. Most of the current commercialization models are directed towards a business-to-business (B2B) strategy involving the research and academic market instead of the development of a real end-user product. [Becker, 2009] According to Blow [2007] developers are now moving away from the idea of the single 'killer app' and are instead focusing their efforts on bridging the divide between industry and academia in the hopes of using microfluidics as an enabling technology for a wide range of life-science applications.

The integration of detection mechanisms with microfluidics may be one of the most promising routes towards widespread application of LoC devices. Photonic detection methods in particular have the advantage to be non-invasive, easy to sterilize and highly sensitive even with short integration times and thus allow in-situ monitoring and quantification of biological and chemical processes. Unfortunately, the execution and readout of optical detection methods usually requires special training of potential users, as in most cases they are confronted with the need of establishing fiber-optics connections to and from the PhLoC and/or rely on the use of complex laboratory equipment.

The following chapter treats the efforts undertaken during this thesis towards technology transfer, i. e. the development of tools and design guidelines that could make PhLoCs more apt for on-site measurements and ultimately for being handed over to collaborators for the execution of spectroscopic measurements. These efforts encompass two main building blocks: Easy-to-use physical connections to and from the PhLoC and the software interface dealing with the data manipulation and real-time feedback to facilitate the operation. The first part was covered using fast prototyping of low-cost and robust physical Chip-to-World Interface (CWI) for PhLoCs. The design was focussed on establishing robust and easy-to-use connections of the *on-chip* photonic components with the *off-chip* fiber-optics, using standard SMA-connectors (non-pigtailed), such that PhLoCs and fiber-optics can be plugged into the Chip-to-World Interface (CWI) without the need for further adjustments by the (unskilled) user. After introducing the involved design schemes and fabrication methodology, the performance of a low-cost fiber-coupler was compared to that of a commercial counterpart and an experimental study exploring robustness and required alignment margins of the fully assembled CWI was carried out. The results shown in this chapter are meant to showcase the reliability of such low-cost optical interconnects and discuss the benefits as well as the limitations of the approach. The second part, the implementation of a software interface to facilitate data acquisition and interpretation for the end-user, was

realised as a flexible cross-platform software solution based on Python[1] and the open source branch of the Qt[2] SDK as opposed to the commercial laboratory standard of LabVIEW[3]

3.2 The physical interface: Plug & Measure

The gross of the results presented in this section have been published as a Technical Innovation in the Lab on a Chip Journal [Ackermann et al., 2016a]. The article is reprinted in Appendix A.

3.2.1 Design and working principle

Fig. 3.1a shows an emulator of a PhLoC only comprising a bent dielectric Waveguide (WG) on a transparent substrate, which will serve us as a model for proof-of-concept. As illustrated, effective coupling to and from the WG occurs at specific relative coordinates and incident angles of 90° to the respective edges of the PhLoC.

The proposed CWI for such PhLoCs is depicted in Fig. 3.1b-d. The required precise relative positioning of fiber-optics connections and PhLoC is achieved by splitting the design-scheme in several independent building blocks. That way every unit can be fabricated separately in-plane, which makes it possible to take advantage of the full lateral resolution of the planar technologies used in this work. As shown in Fig. 3.1b, a robust outer frame composed of four interlocked blocks confines the PhLoC in the y-axis. To facilitate the insertion and removal of the PhLoC, an additional movable block is used to confine the space in x-direction and push the PhLoC in position after insertion - aligned with the fiber-optics Figs. 3.1b-c depict the design-schemes of the blocks for the input (y-z) and output (x-z) plane respectively. A thin platform is anchored here at the required height level (z-position) to align the end-facets of the WG with the center of the circular opening representing the fiber-connector. The fiber-connections are optimized to facilitate plugging in and out of industrial standard SMA-connectors in order to increase the versatility and ease of use of the interface. As those connectors have standardized dimensions,

[1] Python Software Foundation. Python Language Reference, version 3.x. Available at python.org

[2] Cross-platform SDK available at www.qt.io under a creative commons share alike license

[3] "LabVIEW is systems engineering software for applications that require test, measurement, and control with rapid access to hardware and data insights", available from National Instruments™

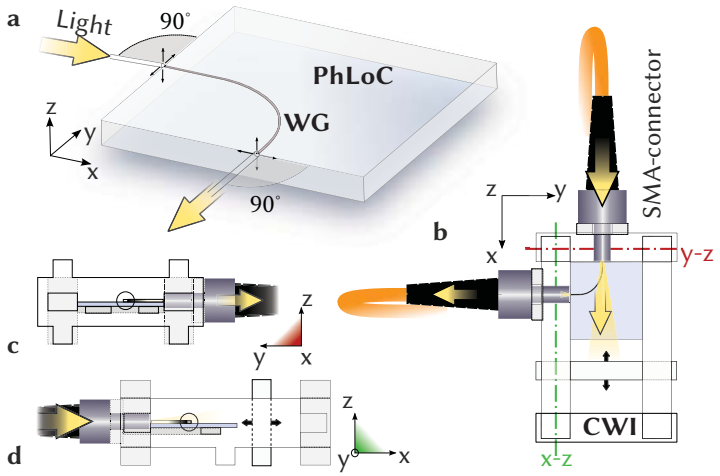

Figure 3.1: Schematic illustration of chip-to-world interface concept.

the user can choose between a variety of fiber diameters without changing the design.

The design of the CWI and the photonic structures on the PhLoC respectively is coupled and based on the idea of trading coupling losses for a high signal-to-noise ratio. Concretely, we introduce the 90° bends in the WGs to achieve an optical output perpendicular to the optical input. In that way, independently of the in-coupling efficiency, the output will result from the light coupled into the photonic structure of the PhLoC (signal), while the non-confined light (noise) should not reach the readout. This approach allows us to use integrated photonic structures with far smaller dimensions than those of the input fiber-optics without spoiling the signal-to-noise ratio. Thus, the required alignment precision can be met by low-cost (and high throughput) fabrication while maintaining full functionality. A detailed model of the initially proposed fiber-connections (hereafter called 'plug-optics') is included in the following section in Fig. 3.4. The concrete building block design as well as the 'plug optics' have evolved in the course of this thesis, as will be shown with a few examples at the end of this chapter.

3.2.2 Materials and Methods

Materials

SU-8 2005 was purchased from *MicroChem Corp* and used as received. 4" borosilicate wafers were purchased from *SCHOTT Suisse SA* with a thickness of 0.7 mm. (30 × 30) cm^2 PMMA plates were purchased from *Ferreteria Maranges S.A.* in thicknesses of 1 mm, 3 mm, and 5 mm and flexible polyurethane foam was purchased from *RS Components Ltd.*

PhLoC fabrication

For the fabrication of the dielectric waveguides, a 6 µm thick SU-8 layer was spincoated at 3000 rpm on O_2-plasma activated borosilicate (Pyrex®) wafers. The 90 µm wide waveguides (bend radius = 4 mm) were then defined via direct photo-lithography (compare section ??) as follows:

First, a borosilicate (Pyrex®) wafer was exposed to O_2-plasma during 18 seconds at 480 W to activate the surface. SU-8 2005 was spincoated at 3000 rpm and submitted to a soft-bake (soft-bake (SB)) for 20 min at 95°C after an initial temperature ramp from (65 to 95)°C during 15 min. Waveguides were defined by exposing the soft-baked SU-8 through a Film Mask ordered from JD PHOTO DATA in a KS A6 mask aligner (SÜSS MICROTEC AG) with a dose of 330 mJ/cm^3. The exposed structures were post-exposure baked (post exposure bake (PEB)) for 10 min at 95°C with ramp as before.

The process yielded WG with cross-section of (90 × 6 µm ^{2} as confirmed by a mechanical profiler. The wafer was cut using a diamond blade cutting machine, maintaining a safety distance of 25 µm from the WG facets, to release the individual PhLoCs.

CO_2-laser processing of poly-methylmetacrylate (PMMA)

CO_2-laser processing of PMMA combines the attributes low-cost and minimum time consumption (being a one step process). Thus it is an ideal method for rapid prototyping as well as industrial level fabrication of the final product.

PMMA, while being highly transparent in the visible spectrum, acts as an excellent absorber in the far infrared and can therefore be very effectively processed by a CO_2-laser. In addition, its low weight together with reasonable hardness and low cost are perfect characteristics for a cheap and robust CWI.

In this work we used a commercially available Epilog Mini 24 laser writer employing a CO_2-laser (see Table 3.1 for specifications) for the fabrication. It can be directly addressed by a computer as one would a conventional printer. 2D-patterns designed as vector graphics are sent to the

Table 3.1: Characteristics of Epilog Mini 24.

working wavelength	10.62 µm
maximum power	30 W
maximum cutting speed	88.9 mm/s
resolution	1200 dpi max.
precision of xy-positioning	±12.7 µm

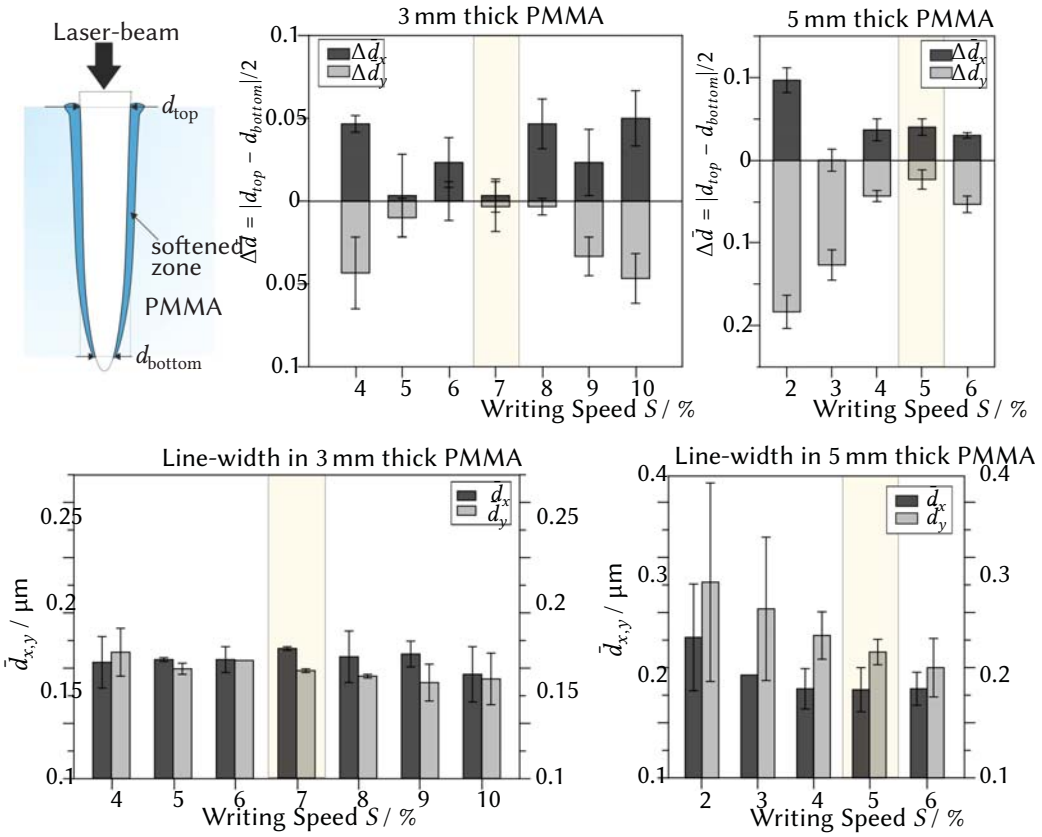

Figure 3.2: Differences of d_{top} and d_{bottom} for a series of cutting speeds in 5 mm and 3 mm thick PMMA respectively, keeping $P = 100$ and $F = 5000$ constant. The condition in which this difference was smallest and less dependent on the writing direction is highlighted and was used to set the design dimensions.

machine together with the desired configurations of power (P), writing speed (S) and laser pulse frequency (F). The combination of the latter parameters controls the gaussian beam shape of the laser and thus the line-width as a function of the penetration depth as described in detail by Prakash and Kumar [2015]. Please refer to section 1.5.2 for a more extensive discussion on the subject.

For the fabrication of the CWI building blocks, 1 mm, 3 mm and 5 mm thick PMMA sheets were employed. As shown on a conceptual basis in 1.5.2, the variation of the line-width as a function of depth becomes more important, with increasing thickness of the PMMA. The consequence is a measurable difference between the line-width d_{top} at the top and d_{bottom} at the bottom of the PMMA sheet respectively. The variations induced by different cutting conditions were therefore studied at length with the results presented in Fig. 3.2

We found that due to different mechanisms for the motion-control in x- and z-axis of the laser writer, the average line-width $\bar{d} = (d_{top} + d_{bottom})/2$ also differs depending on the direction of the cut. Thus, cutting conditions have been optimized for the 3 mm and 5 mm thick PMMA sheets with the aim to minimize this variation and approximate vertical walls as much as possible.

Table 3.2: Optimal cutting conditions and corresponding line-widths for PMMA based on the characterisation shown in Fig. 3.2 as used in the fabrication of the CWI elements. F is the laser pulse frequency in Hz, P the percentage of maximum power and S the percentage of maximum speed.

PMMA thickness	Conditions	Resulting average line-width $\bar{d}$
5 mm	F = 5000 P = 100 S = 5	$\bar{d}_x$ = 160 µm ± 30 µm $\bar{d}_y$ = 220 µm ± 25 µm
3 mm	F = 5000 P = 100 S = 7	$\bar{d}_x$ = 235 µm ± 20 µm $\bar{d}_y$ = 195 µm ± 10 µm

Resulting optimal conditions are listed in Table 3.2.

Interlocks for robust assembly

The crucial part for robust interlocks between adjoining building blocks are the corresponding plugs and sockets. The relative dimensions were empirically optimized under consideration of the previous characterization of direction-dependent line-width as shown in Fig. 3.3. For the best fitting of adjoining parts, a tolerance value of 150 µm was added to the desired dimension in x or y respectively according to $w_{\text{design}} = w_{\text{real}} \pm \bar{d} + 150\,\mu\text{m}$, where w_{real} is the desired dimension after fabrication and w_{design} the respective length introduced in the design scheme. The sign of $\bar{d}$ is positive when designing outer structures (plugs) and negative for inner structures (sockets).

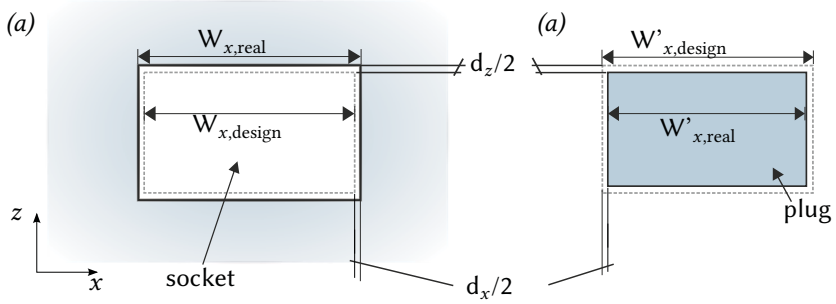

Figure 3.3: (a) Schematic illustration of the design schemes for the laser cutting of plugs and sockets.

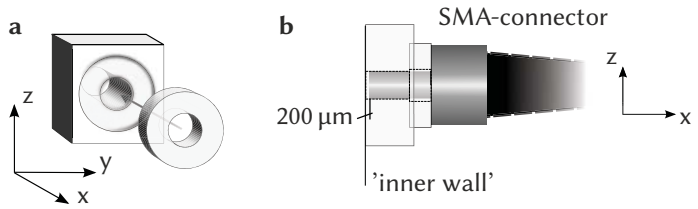

Figure 3.4: a) Detail of plug-optics assembly. b) An SMA fiber-connector plugged into the described unit is firmly clamped, leaving the end-facet at a distance of approximately 200 µm *from the 'inner wall'.*

'Plug-optics'

Based on the same interlock concept, sockets for *SMA* fiber-optics connectors were optimised empirically and implemented according to the model depicted in Fig. 3.4. To fabricate the proposed custom fiber-connectors (hereafter called 'plug-optics'), a cylindrical socket with a design-diameter of 3 mm is laser-cut into 5 mm thick PMMA applying the optimized conditions $P = 100, S = 5$ and $F = 5000$ at 1200 dpi using the Epilog Mini 24 laser writer. Subsequently, the thickness of the block is reduced in a concentric circular area by laser engraving applying 'raster' conditions of $P = 35, S = 12$ and $F = 5000$ at 1200 dpi. A 3 mm thick PMMA disk comprising a cylindrical socket with 3.5 mm design-diameter cut applying $P = 100, S = 5$ and $F = 5000$ and equally reduced in thickness by laser-engraving. The disk is glued into the pre-structured area on the 5 mm thick PMMA.

CWI assembly

The assembly of the complete CWI is illustrated schematically in Fig. 3.5 (a). The arrows indicate how the interconnects comprised of plugs and sockets are fit into each other respectively. The concrete function of each building block is detailed in the figure caption. Some examples of fabricated individual building blocks and a completely assembled CWI are shown in Fig 3.5 (b).

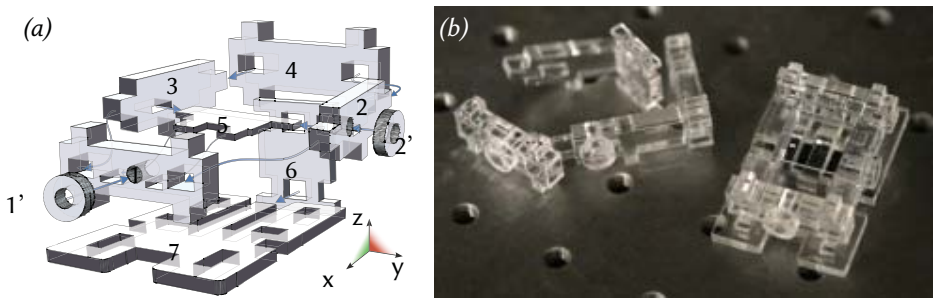

Figure 3.5: (a) Model of the individual building blocks and their assembly. 1, 2*: Primary building blocks defining the input and output plane comprising sockets for SMA-connectors and platform* 5*;* 5*: Platform to sustain the PhLoC at the corresponding height relative to the fiber-optics;* 1′, 2′*: Spacer disks adjusting the distance from fiber-optics to edge of PhLoC;* 3*: Side-wall comprising socket to sustain* 5*;* 4*: Back-piece completing the outer frame; Blocks* 1 – 4 *are anchored in the base to assure right angles and provide additional stability;* 6*: Base of CWI comprising track to guide movement of unit* 6*;* 6*: Mobile unit anchored to tracks in the base in order to be moved back and forth clamping the PhLoC in place or releasing it. (b) Photograph of the laser fabricated constituent parts and the fully assembled CWI.*

PhLoC insertion

Once the CWI is fully assembled, a PhLoC can be inserted easily as illustrated in Fig. 3.6.

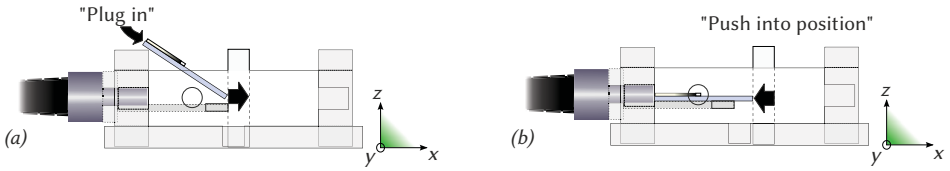

Figure 3.6: Schematic illustration of how the PhLoC is plugged into the CWI (a) and pushed in position aligned with the SMA fiber-connector (b)

Optical characterisation

In all experiments, a fiber-coupled red laser (635 nm, 2.5 mW, Thorlabs, Inc.) connected to a FC/PC-SMA multimode fiber (Thorlabs, Inc.) with core/cladding diameter of 200/230 µm and numerical aperture NA of 0.22 was employed as light source. A QE Pro 65000 photo-spectrometer (Ocean Optics) served as detector. To obtain a 2D-mapping of the output plane, a pig-tailed 50/125 µm fiber was mounted on a motorized xz-stage (Micos VT80, Eschenbach, Germany) perpendicular to the edge of the PhLoC to scan the area around the WG end-facet with a step size of 10 µm. Movement and intensity acquisition were controlled by a LabVIEW script to obtain the complete mapping of the optical output plane. The intensity at 635 nm was collected at each point for constant input power of 0.25 mW and with an integration time of 25 ms. SMA-SMA

multimode fiber-optics (Thorlabs, Inc.) with core/cladding diameters of 50/125 µm, 105/125 µm and 200/230 µm and numerical aperture NA of 0.22 were used to evaluate the plug-optics individually and in their function as chip-to-world interface.

Simulations

Ray-tracing simulations emulating the experimental conditions were performed using TracePro (Lambda Research) for comparison. To that effect $8{\cdot}10^5$ rays with a wavelength of 635 nm were traced through a 3D-model of the PhLoC from a perfectly aligned, 2 m long input fiber-optics with NA of 0.22. The waveguide's modal profile was examined in form of the irradiance map on the output plane at 200 µm distance from the edge of the PhLoC.

3.2.3 Results and discussion

Plug-optics evaluation

In order to assess the reproducibility and performance of the proposed plug-optics connectors, three sets of plug-optics were fabricated and assembled in all possible combinations to form a three-slot fiber-to-fiber connector. To that end, they were interlocked with and held together by auxiliary bottom- and top-pieces made of PMMA. Fiber-to-fiber coupling was evaluated by averaging the coupled intensity over the three combinations and the resulting plug-optics triplets. For constant input intensity, the average output intensity was recorded as a function of the size of the output fiber-optics. The architecture and results compared to a commercial two-slot fiber-connector are presented in Fig. 3.7. The statistical evaluation shows that there are no significant differences between coupled intensities obtained using either of the connectors. The plug-optics connectors though show more variation as a result of low-cost fabrication and assembly. This variation becomes more important, the more similar the diameters of input and output fiber-optics.

Plug and Measure

From the evaluation of the plug-optics coupler it would seem that size mismatch between emitting and receiving end ensures reliable and reproducible, if inefficient coupling. Robust fiber-to-chip coupling should therefore be viable using the proposed CWI in the case of sufficient size mismatch between on-chip photonics and fiber-optics. As another consequence, an important fraction of the incoming light would not be coupled to the WG, but propagate as stray light through the structure and may thus to some extent contribute as noise to the optical readout.

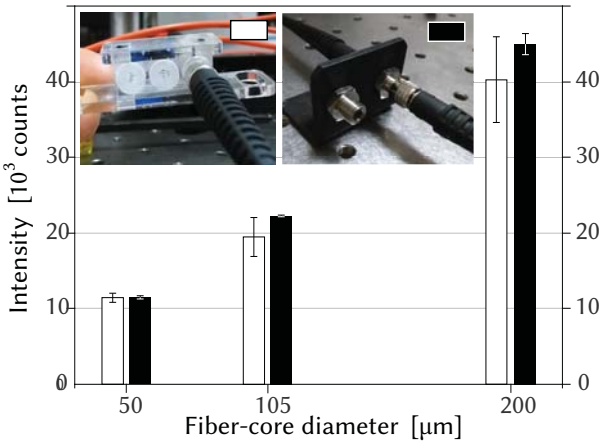

Figure 3.7: Evaluation of the 'plug optics' concept. Average intensities coupled from fiber-optics to fiber-optics using plug-optics and a two-slot commercial fiber-connector are compared.

Signal-to-Noise Ratio (SNR). In this context, as a next step we assessed the contribution of stray light to the output signal on the basis of the previously described PhLoC. An intensity mapping of the output plane was used to assess the Signal-to-Noise Ratio (SNR). To obtain this 2D-mapping, a pig-tailed 50/125 µm fiber was mounted on a motorized xz-stage (Micos VT80, Eschenbach, Germany) perpendicular to the edge of the PhLoC as shown in Fig. 3.8. The area around the WG end-facet was scanned with a step size of 10 µm in an area A of (500 x 500) µm^2 around the center of the WG and at a distance of 200 µm from the edge of the PhLoC. Movement and intensity acquisition were controlled by a LabVIEW script to obtain the complete mapping

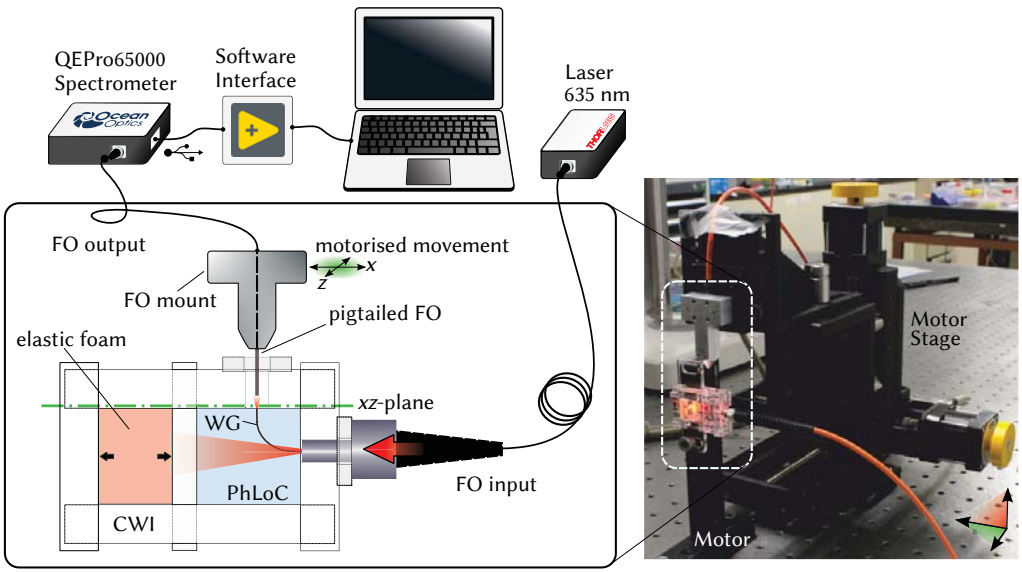

Figure 3.8: Experimental setup used for the 2D-mapping of the WG output.

of the optical output plane. The intensity at 635 nm was collected at each point for constant input power of 0.25 mW and with an integration time of 25 ms. Simulated and experimental results are presented in Fig. 3.9.

Fig. 3.9a shows the light propagation through the model PhLoC according to the ray-tracing simulation conducted with TracePro. Due to inefficient coupling (insertion losses of 15.4 dB are to be expected according to the simulation), a large portion of incoming rays result in stray light. Yet, no stray light reaches the output plane: The irradiance map obtained from the rays incident on *A* shows no measurable incident radiation apart from a localized and sharply peaked intensity profile corresponding to the multi-modal SU-8 waveguide with (90 x 6) μm^2 cross-section.

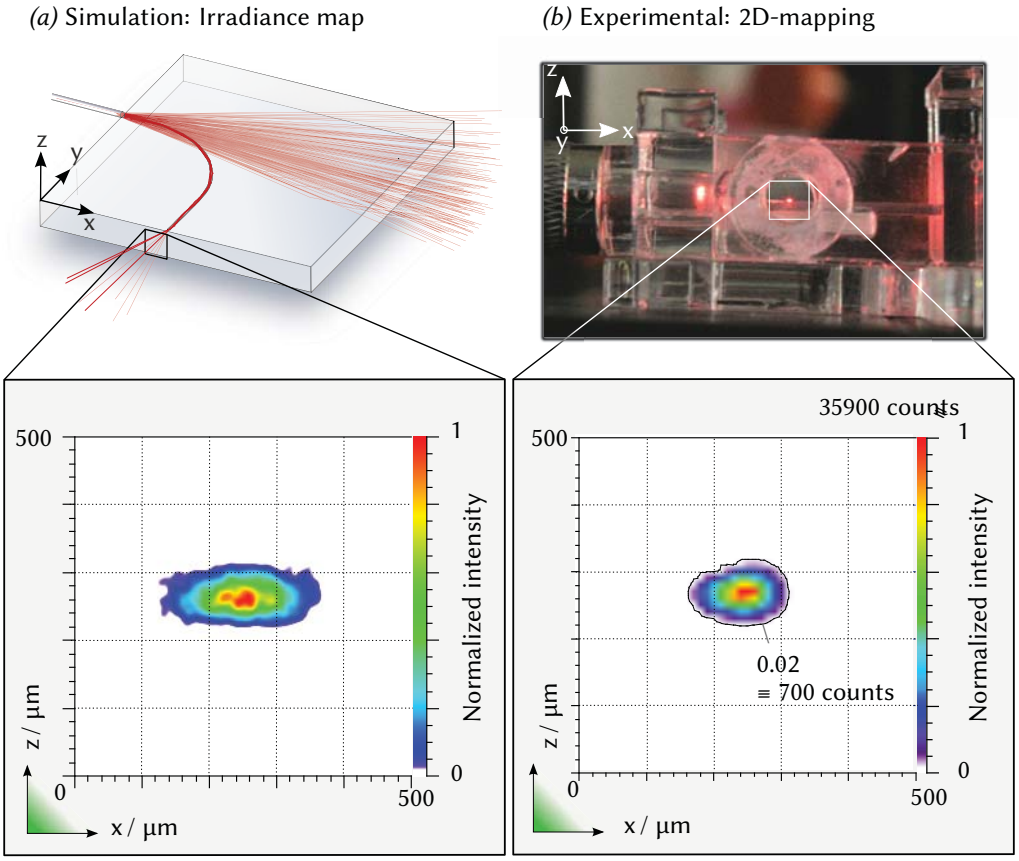

Figure 3.9: a) Ray-tracing simulation (using TracePro, Lambda Research) of a 90° bent SU-8 waveguide (cross-section (6x90) μm^2) on glass substrate. $8 \cdot 10^5$ rays with a wavelength of 635 nm are traced through the model via a 2 m long fiber-optics (200/230 µm, NA = 0.22) aligned with the waveguide. An irradiance map shows the intensity profile of the waveguide output on the x-z plane at 200 µm distance from the waveguides end-facet. b) (500 x 500) μm^2 2D-mapping around the WG output obtained by pig-tailed 50/125 µm fiber-optics mounted on a motorized stage and the resulting 3D-profile.

As a result of the high numerical aperture of the WG, an extensive expansion of this profile with the distance from the end-facet of the waveguide could be expected. This is reflected in the profile's dimensions of roughly 200 µm in x-direction and 70 µm in z-direction found in the irradiance map.

Fig. 3.9b shows the experimental fiber-to-chip coupling using the proposed CWI and 2D-mapping of the resulting output profile. In the photograph, the end facet of the WG can be identified as a confined bright spot in the center of the small square, which corresponds to the scanning area A. The picture demonstrates that light is coupled successfully via the plug-optics to the thin SU-8 waveguide and guided through the bend to the output. The mapping result shows a localized and sharply peaked region of high intensity (signal S) with a maximum peak intensity of $S_{\text{max}} = 35900\,\text{counts} \equiv 1$ corresponding to the WG output. It is worth noting that the experimental output profile is more localized than the simulated one. This can be attributed to the low numerical aperture of the scanning fiber-optics. While in the simulation all rays incident on A contribute to the profile, radiation at large angles is discarded in the experiment. The contour line in the 2D-profile marks the threshold between what can be considered waveguide output and background noise N and defines profile with effective width of ≈ 160 µm in x-dimension. In the scanned area outside the contour line, the recollected intensity does not exceed a maximum of $N_{\text{max}} = 700\,\text{counts} \equiv 0.02$. We therefore assume that as a consequence of the introduced WG bend, stray-light indeed does not contribute as noise to the readout on the output plane. Hence, in the case of optimal alignment of the receiving 50/125 µm fiber-optics with the waveguide output and relatively low input power of 0.25 mW, we achieve a signal-to-noise ratio of $\text{SNR} = S_{\text{max}}/N_{\text{max}} = 50$.

The sharpness of the intensity profile indicates that, depending on the diameter of the fiber-optics employed as output, small deviations in alignment and positioning may result in significant variations of the readout. On the other hand, in sight of the measured SNR fiber-optics with large (up to 500 µm) core diameters could be used for the readout in order to provide sufficient alignment margins and achieve maximum output without significant noise contribution. In the following, we explore the robustness and repeatability of the readout provided by the proposed CWI applying different alignment margins.

Robustness and repeatability of measurements. The completely assembled CWI, with PhLoC as well as fiber-optics input and output plugged in, is shown in Fig. 3.10a. In this configuration we studied the influence of fabrication precision, assembly/disassembly and repeated positioning and alignment of PhLoC and fiber-optics on the output signal. The input unit (compare Fig. 3.1c) was fabricated twice and, exchanging this part between each measurement

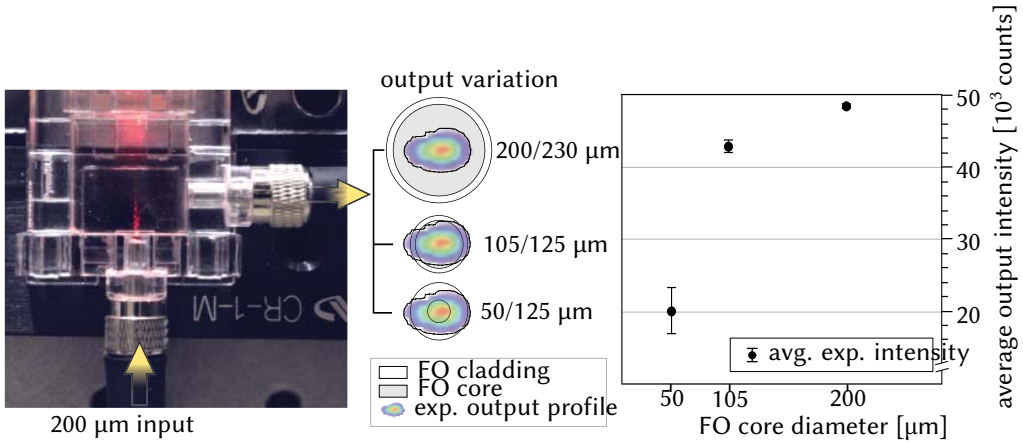

Figure 3.10: a Plug and measure. Photograph of CWI with plugged PhLoC and fiber-optics showing fiber-connection and light coupling to and from the PhLoC. For different output fiber-optics, the relative dimensions of the experimental output intensity profile at 200 µm distance from the WG and the fiber-optics cross-sections are shown schematically. b Measured intensities corresponding to different fiber-optics configurations. The error bars correspond to experimental intensity variations of 7.5 % using 50/125 µm, 3.3 % using 105/125 µm and 0.6 % using 200/230 µm fiber-optics as output respectively.

and plugging the PhLoC in anew, the output intensity was collected subsequently by different output fiber-optics. Varying the diameter of the output fiber-optics results in different overlap situations of fiber-optics and the intensity profile originating from the WG. As apparent from Fig. 3.10a, misalignment may produce strong variations of signal intensity using a 50/125 µm fiber as output, while using a 200/230 µm fiber the intensity may well be invariable to small misalignments.

As shown in Fig. 3.10b, the experimental value obtained by the 50/125 µm fiber-optics indeed shows significant variation. Using 105/125 µm fiber-optics this variation is greatly reduced and using the 200/230 µm fiber-optics, no significant signal variation was obtained. These results are in line with the previous findings and show that the combined alignment variations induced by fabrication precision (compare Table ??), repeated assembly/disassembly and plugging in and out of the PhLoC are fully compensated by the alignment margins of ±20 µm provided by using 200/230 µm fiber-optics for input and output. Together with the obtained SNR = 50, this validates the proposed methodology of fabrication and assembly as a robust and cheap solution for PhLoC-to-world connections which could be employed beneficially in a series of already developed PhLoCs with different approaches integrating for instance optical spectroscopyRodríguez-Ruiz et al. [2016], Prabhakar and Mukherji [2010], flow cytometryWatts et al. [2012], Fei et al. [2012], Godin et al. [2008, 2006], Wang et al. [2004] or photonic whispering gallery mode (WGM) structures for label-free molecular detectionWienhold et al. [2015], Bog et al. [2015] in microfluidic systems.

3.3 Modular software interface

3.3.1 Motivation

The development of a modular software interface encompassing all the components and routines of the optical measurements in the same interface was motivated from different sides in the context of this thesis. Several motives arose already at the stage of laboratory use as a result of trying fruitlessly to synchronise equipments from different manufacturers - or more frustratingly more than one piece of equipment from the same manufacturer - while executing a joint task. Others arose in the event of moving an experiment from the well known ground of the optics laboratory out into the world, where suddenly changing ambient light conditions do not bother anyone. Again others are related to the vast amount of data, which is created when, instead of performing a measurement at a particular point in time, the process to be followed spectroscopically can take from hours to several weeks but important changes can occur on the time scale of minutes. In such a scenario it is of particular interest that the data is fed back to the user in an understandable format and in real time. And then there is the convenience of automation of measurement routines, which not only saves the scientist a lot of time but also greatly reduces the human error.
Given this context, a solution to even one the aforementioned difficulties can save the scientist a lot of time and headache on the long run. On the other hand, if aspiring to hand a PhLoCs to an untrained person, a simple graphical front-end may be the key to success.

3.3.2 Protoyping with LabVIEW

The first software prototype was based on the LabVIEW programming language. The primary motivation here was to automatize the monitorization of cell cultures as far as possible, thus facilitating the use of the employed specialized equipment like photo-spectrometers and light-sources. Additionally this brings about the possibility to instantly post-process the obtained data into physically relevant units, which together with the control over the output format results in a major reduction of time, considering the amount of data accumulated during a 3 to 5 days experiment, which otherwise has to be invested by the user.
Concretely, the program guides the user through the setting up of the measurement via text-messages displayed in the front panel and so defines a standardized measurement protocol: *Configuration.* In the first stage, 'Configuration', the user can test the optical connections by turning the lamp on and off via the switches in the software and observing the resulting spectral response received by the spectrometer. Also, he is asked to specify the location on disk,

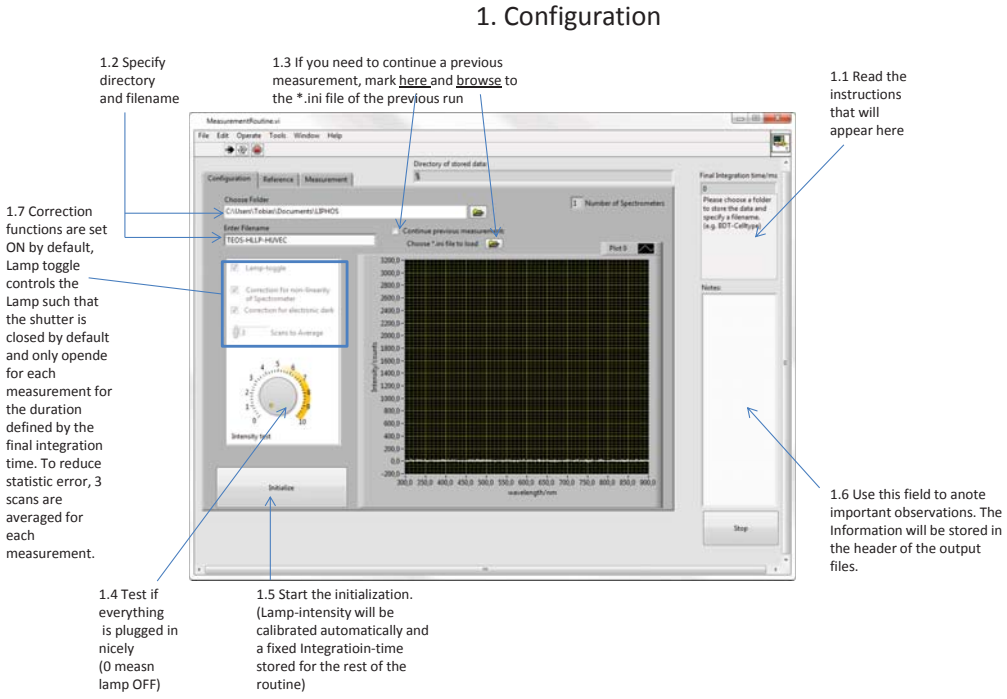

Figure 3.11: Front end of the LabVIEW protoype software defining a measurement routine for an untrained user.

where the data is to be stored as well as a 'filename'. The only other parameter which has to be set by the user at this point is the integration time and the number of spectra to average for every measurement, the choice of which is supported by the real-time spectral response provided to the user, allowing for an adjustment which provides sufficient light to conduct the measurement. In order to continue, the button 'Initialize' has to be pushed, which fixes the parameters directory and integration time for the rest of the experiment.

Reference. The next step in the routine is to store a reference spectrum, which is necessary for the post-processing of the data and indispensable for the interpretation of results. To that end, the user is encouraged - again via the text box - to inject the culture medium which will be used in the course of the experiment and only after this step is completed to proceed to storing the reference spectrum. This step is performed by activating the 'Obtain Reference' button in the second tab of the program. The obtained reference spectrum will be displayed for approval by the user and stored to a file named *.ini located in the working directory previously specified. This file also contains the initialized parameters (i.e. integration time). So alternatively to storing a new reference, the user can also continue a previous measurement by loading its *.ini file (e. g. if an error occurred and the measurement has to be continued using the previous reference).

This option can be ticked on the configuration tab previous to initialization.

Monitorization. Once obtained/loaded a reference spectrum, the user is referred to the 'Measurement' tab, where the measurement routine can be started. This tabs has three sub-tabs, namely 'Intensity', 'Transmission' and 'Absorbance'. Here, the acquired data is post-processed and displayed in real-time until interrupted ('Pause/Resume') or stopped ('Stop') by the user. The absorbance values can be displayed in absorbance units (A.U.) or converted to dB (default). Once the measurement is started by pressing the respective button, the program will acquire a spectral response periodically with a standby time specified by 'time between measurements'. This parameter can be introduced in seconds or minutes and re-adjusted while the measurement is in course. The light-source is switched on automatically for the duration of the measurement ('integration time' x 'number of scans') and switched off during standby in order to not disturb the cell culture. *Data storage.* The acquired data is stored in the specified location in a folder named 'filename'. Apart from the aforementioned *.ini file, separate *.txt files containing the raw data (named with the date of the measurement and 'filename') as well as the processed data (Absorbance, Transmission and a timeline for every wavelength) will be stored in this folder. During the measurement, temporary files *.tmp are created to accumulatively store the data in order to prevent data loss. The temporary files are converted into *.txt files after the 'Stop' button is activated and the experiment finished. All data files contain a header with all the initialized parameters, a first column containing the wavelengths, a second column containing the reference and subsequent columns labeled with the corresponding timestamp (e.g. "@ 15min"). The timelines first column is the time passed after the start of the experiment, while the subsequent columns contain the corresponding unprocessed intensity values for every measured wavelength. These formats ensure easy data import in scientific graphing and data analysis software (e.g. Origin, QtiPlot, ...).

A large part of the code for this software interface was adapted from previous work by Joan Juvert and Alfredo Gonzales, replacing their spectrometer driver implementation with the OmniDriver package provided by Ocean Optics[4] and adding the framework for the previously described measurement steps. Although providing a relatively fast way to create an intuitive user interface, the LabVIEW approach has several drawbacks. First of all, the wire-coding gets very messy very fast. So, while the method of visually connecting different elements is very intuitive while building the program, the maintenance of a rather elaborate program as the one presenting its shiny front-end in Fig. 3.11 was a major challenge. In addition, the drivers were based on outdated 32-bit libraries, which were at risk of being overwritten with every Windows[5]

[4] see the OmniDriver website for more information
[5] Microsoft Windows

update, and on 64-bit machines the installation required, apart from running 32-bit LabVIEW, an elaborate installation protocol including different driver versions for the spectrometers to be recognised.

Given the many Windows flavours out there, the portability of this software solution would probably require trained personnel only to get the program up and running.

3.3.3 The Python implementation

The Python implementation presented in this thesis is a fork of the well documented PySeabreeze Library by Andreas Poehlman available at github For the sake of completeness, the schematic of the internal structure of this library as it appears on *Github* is reprinted here (see Fig. **??**).

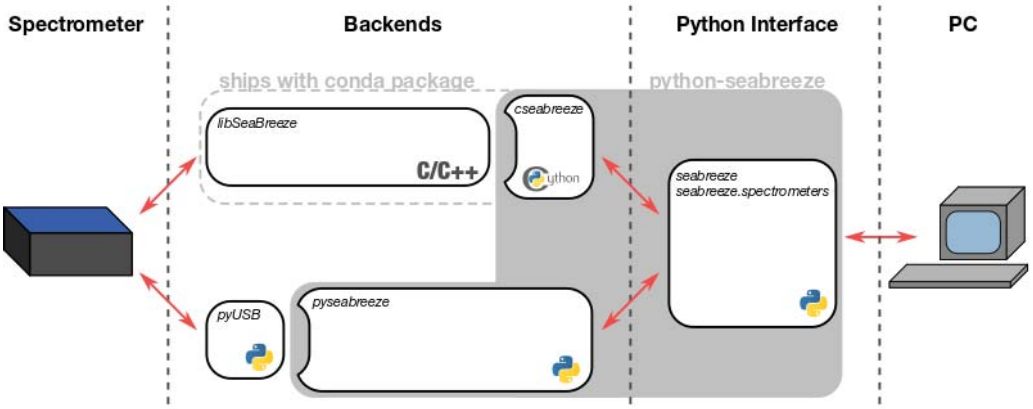

Figure 3.12

The 'My Optics Laboratory' class

The Python class *MyOpticsLab.py* provides a set of functions designed to query for all possible predefined pieces of equipment, which are defined as their own Python classes with corresponding functions and routines, list and initialise them. Starting from there, the modular syntax of Python is ideal for quick programming of adapted routines on a daily basis in the laboratory. Another very convenient point in the Python data structure are the *dictionaries*, which allow intuitive indexing, e. g. a dictionary can store data under a certain *keyword*. Take for instance a dictionary initiated as

Absorbance = {}

and at each point in time *t* add an entry with the time key *Absorbance['@t']* as opposed to other datastructures such as lists, where indexing works using integer numbers as in *Absorbance[0]* or *Absorbance[223]* for instance,

considering a somewhat longer experiment. These are just some of the many advantages that Python can offer apart from being free, as in ”freedom”. For the full code of the module, please refer to the appendix section ”Software Code” (??).

Cross-platform front end

”On the fly” coding is nice enough for the usual laboratory use, but again, if a setup is meant to be handed over to someone else, the explanation of the module-intern functions for every piece of equipment might get a bit cumbersome. Fortunately, the Qt SDK is fully compatible with the code above and is available as an open source branch. The nice thing about SDKs like Qt is that they usually provide a graphical designer greatly facilitating the process of creating a user-friendly front end. In Fig. 3.13, an exemplary front end created with said designer is showcased, featuring two Python cseabreeze-controlled spectrometers, a panel with some buttons for the configuration, some heavy post-processing to cross-reference one spectrometer with the other and thus correct, for instance, the ambient light in real time and a PyQTGraph ViewPort in order to visualize the processed data in real time.

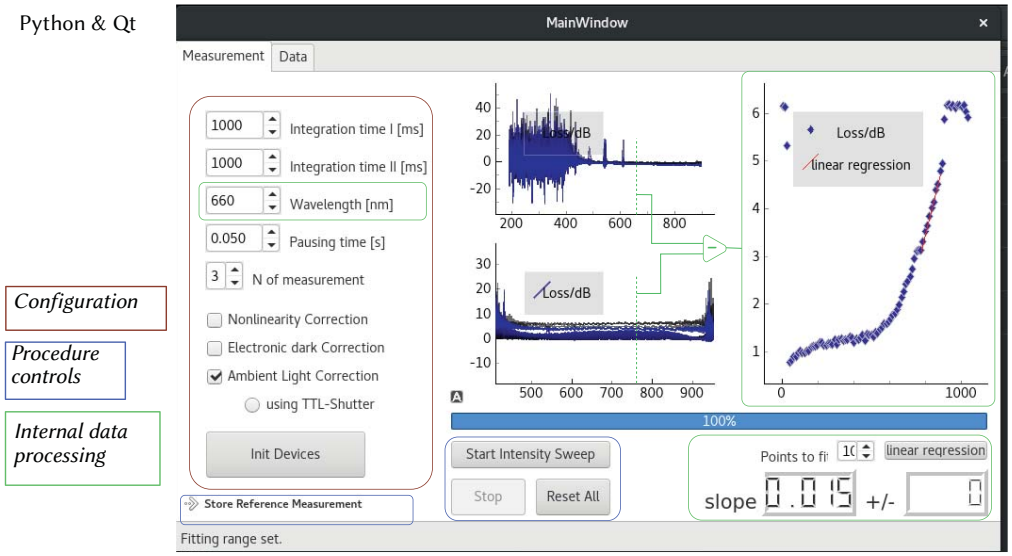

Figure 3.13: Cross-platform graphical front end for the laboratory modules provided by the MyLabOptica class powered by PyQt and PyQtgraph.

3.4 Conclusions

We have presented a cheap, robust and easy-to-use chip-to-world interface for photonic lab-on-a-chip devices (PhLoCs). Comparing the proposed plug-optics SMA fiber-connections by themselves to a commercial fiber-to-fiber connector, we found that the performance was not significantly different. This standardization gives great versatility to the interface, providing a direct link between PhLoCs and a wide range of light sources and photo-detectors.

Experimental evaluation of the fully assembled CWI showed that the introduction of bends in the photonic structure allowed to efficiently discard stray-light artefacts and obtain a clean signal with good signal-to-noise ratio (SNR = 50). In this optimized configuration it could be shown that alignment margins of ±20 suffice to fully compensate misalignments induced by fabrication or assembly. Even through different cycles of fabrication and assembly as well as plugging in and out of the PhLoC, coupling to SU-8 multimode waveguides as thin as 6 µm has been demonstrated without significant signal variation.

The fact that PhLoCs can be easily plugged in and out by a user without a special skill-set while obtaining full functionality is a big step forward in terms of user-friendliness and potentially brings PhLoCs one step closer towards practical applications. In addition, we have demonstrated that Python is a real alternative to LabVIEW for laboratory programming especially in terms of creating and maintaining front ends for final applications. The cross platform and open source character of Python also opens pathways towards more portable equipment.

Optical sensing of microbial surface colonization on-chip 4

The following chapter details the efforts invested in the early detection of bacterial biofilms by optical measurements using visible light and the development of a low-cost PhLoC platform to that effect permitting the formation of a biofilm in flow conditions as connecting photonic element between two integrated waveguides.

4.1 Introduction

Biofilms are biological structures resulting from the microbial colonization of surfaces and mainly composed of micro-organisms and self-produced biopolymers (the extracellular polymeric substances (EPS)). Biofilms are considered a risk for public h°ealth for their ubiquity [Hall-Stoodley et al., 2004, Popham et al., 2012], resistance to biocides [Molin and Tolker-Nielsen, 2003, Stewart, 2002] and dynamism. In biofilms, bacteria and bacterial layers are recruited from and released to the medium over time, thus acting as microbial sources in natural environments. This is of particular relevance when pathogenic bacteria are present in the biofilm. Biofilms in natural environments may contain pathogenic bacteria, e.g. *Legionella spp.* even when these strains are not able to grow a biofilm by themselves [Stewart, 2002, Murga et al., 2001]. To guarantee health safety, biofilms require an intensive control, with sensitivity and selectivity, from the initial stages of surface colonization.

Surface colonisation can be divided in several stages, which are detailed in Fig. 4.1. Colonization and biofilm formation starts with the reversible attachment of suspended bacteria to a surface through weak Van der Waals forces (Fig. 4.1 (1)). The constant contact between bacteria and surface initiate quorum sensing mechanisms resulting in changes in the phenotypic expression of the microorganism [An and Parsek, 2007].

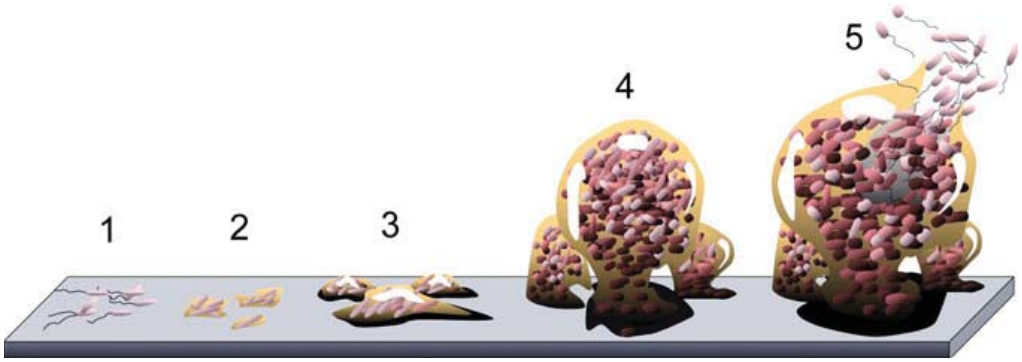

Figure 4.1: Stages of biofilm formation (reprinted from [Unosson, 2015]). (1) Initial adhesion, (2) Cell agregation and excretion of extracellular polymeric substances (EPS); the attachment becomes irreversible. (3) A biofilms is formed. (4) Three dimensional growth and maturation. (5) The biofilm reaches a critcal mass and disperses planktonic bacteria to colonise other surfaces.

Microorganisms then begin producing and secreting biopolymers, mainly polysaccharides and lipids, that generate an external polymeric matrix where bacteria are irreversibly attached [Whitchurch, 2002] (Fig. 4.1 (2)). Successive adhesion of bacteria, cell divisions and secretion of biopolymers lead to the formation of a mature porous biofilm, which grows until eventually releasing aggregates of planktonic bacteria to colonise other surfaces (Fig. 4.1 (3-5).

Common systems for biofilm monitoring use thermal, mechanical or electrical transduction. Thermal and mechanical systems are indirect and report on biofilm formation through the changes that biofilms produce in the flow in water distribution networks. These systems are therefore restricted in their application and present limitations such as low sensibility (i.e. detection limits > 40 µm, which corresponds to late stages of maturation) and no selectivity, as it is impossible to differentiate between biofilms and other adhered compounds like inorganic salts. In electrical methods, the growing of the biofilm between two electrodes produces a capacitive change as a result of the differences in the effective dielectric constant of biofilms and medium. Capacitive sensors are sensitive but present important stability, durability and reliability limitations due to their sensitivity to external factors, biofouling and positioning of the electrodes.

Optical systems are advantageous for being label-free, sensitive, selective, non-invasive and contactless, while less influenced by environmental factors. Apart from those based on imaging, which require laboratory equipment not able to operate in situ, some biofilm field optical

sensors have been developed based on light scattering analysis, intrinsic fluorescence and the combination of fluorescence, refraction, transmission and scattering. More optical transduction methods are investigated for the development of new tools for in situ analysis based on near infrared spectroscopy, Raman spectroscopy, SERS or pulse photoacoustic spectroscopy. Available non-laboratory based optical sensors still rely on costly equipment and fabrication protocols, large instrumentation and lack of selectivity to specific bacterial strains.

The research detailed in this chapter was therefore focussed on the development of an affordable miniaturised monitoring platform integrating photonic components and enabling light coupling to and from bacterial biofilms. In terms of methodology, our efforts to this end were guided by the following premises: The use of microfabrication protocols, materials and architectures compatible with mass production procedures in combination with the unprecedented measurement strategy proposed in this thesis; the implementation of biofilms as living photonic transducer and reporter. By directly coupling light with a broad spectrum of wavelengths in the visible light spectrum into the biofilm, biofilm-light interaction may be maximised without interfering negatively with the bacteria and provide an *Absorbance* measurement with enhanced sensitivity and selectivity by means of absorption bands of biofilm components which are not usually observed due to predominant scattering effects. The chapter is divided in three blocks: The first one describes technological advances achieved with different strategies for integrating waveguides with thermoplastic materials and corresponding fabrication methods like thermoforming and laser-trimming with the aim of creating PhLoCs for experimental evaluation of the concept. The second block details the characterisation of bacterial surface colonisation dynamics on the materials previously established. Here, a low-cost approach for the physical modification of the materials surface topography with laser-engraved micro-patterns was explored as a means to favourably influence bacterial attachment and biofilm formation in pre-defined surface areas as compared to untreated substrates. The third block envelopes the optical characterisation and first results from biofilm monitoring using the PhLoC configurations that resulted from the previous technological development.

4.2 Integration of waveguides into thermoplastic poly-methylmetacrylate (PMMA) LoCs

The integration of waveguides into a PhLoC as opposed to providing self-alignment elements for the insertion of fiber-optics (FO) provides vast design flexibility as well as the possibility of robust optical connections to the outside world, as has been shown in the previous chapter. Thermoplastic materials as substrates offer some particular advantages in that aspect in contrast to materials like PDMS, which are explored in the following.

4.2.1 Materials

For thermoplastic substrates, poly-methylmetacrylate (PMMA) was chosen as one of the most widely used polymeric materials in industry and due its compatibility with CO_2-laser processing. $(30 \times 30)\,cm^2$ PMMA plates were purchased from *Ferreteria Maranges S.A.* in thicknesses of 1 mm, 2 mm, 3 mm and 10 mm, and from *Microplanet Laboratorios, S,L.* with a thickness of 0.25 mm.

Optical fibers with 200 µm core- and 230 µm cladding-diameter (200/230 µm fiber-optics) were purchased from Thorlabs, Inc. and cleaved using a diamond blade fiber cleaver.

Polymeric waveguides were fabricated on wafer-scale from SU-8 2025, purchased from *MicroChem Corp* and used as received.

4.2.2 Embedded fiber-optics segments

The simplest approach pursued here for the integration of waveguiding structures in thermoplastics was using laser-engraving (as described in section 1.5.2) of aligment-grooves in PMMA substrates for permanently embedding pigtailed commercial fiber-optics. The design of the grooves was adjusted to compensate for the linewidth of the laser beam, the combination of laser power P and scanning speed S optimised to achieve enough engraving depth for embedding 200/230 µm FO. Fig.4.2 shows an excerpt of the vector design used to fabricate the FO-grooves and scanning electron microscope (SEM) images of the resulting engravings on a 10 mm thick PMMA workpiece using optimised working conditions of scanning speed $S = 8\%$ and power $P = 16\%$ for the grooves and $S = 4\%$ and $P = 100\%$ for the trimming, respectively. Due to the thickness of the workpiece, the trimming required two passes of the laser. The prolongation of the groove engravings beyond the trimming edge shown in the design helped to reduce clogging of the

groove by material redeposited in the trimming process. The groove shown in the detail on the left-hand side of Fig. 4.2was engraved in between trimming passes. As can be appreciated in the SEM image, the fold of molten material produced along the edge during the second trimming pass only extends to the edge of the previously engraved groove. The SEM detail on the right-hand side shows the opposite end of one of the fabricated FO-grooves. From the image it can be appreciated that the engraving process results in much less redeposited material than the laser-trimming. Further, the side-walls of the resulting groove are slightly inclined, which will result in a corresponding offset once inserting a FO-segment. As indicated in the schematic, the designed width w of the grooves was set to 180 µm in order to achieve grooves with the approximate 230 µm widths indicated in the SEM details. Fig. 4.3 shows the same grooves engraved under the detailed conditions after inserting 200/230 µm double pigtailed fiber-segments and glueing them in place using a UV-curable optical adhesive (NOA 68, *Norland Products, Inc.*). As a result, about half of the cross-sections of the FO end-facets were located above the surface of the PMMA.

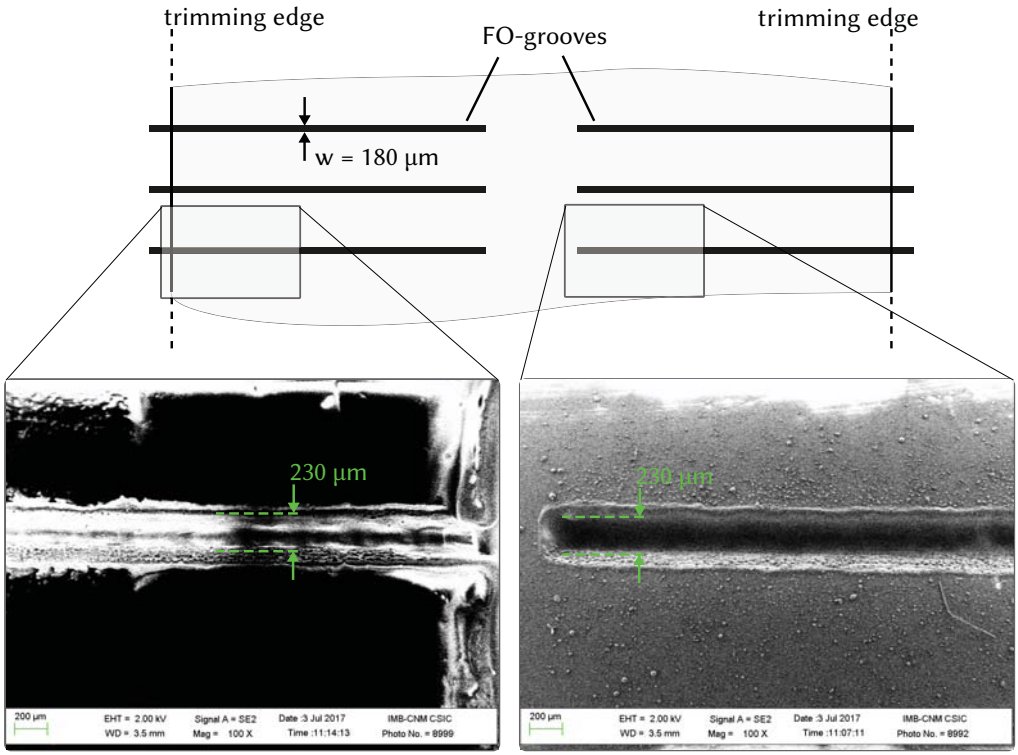

Figure 4.2: Vector design scheme for the fabrication of laser-engraved grooves for fiber-optics (FO) positioning in PMMA. Insets show results of scanning electron microscope (SEM) inspection of fabricated grooves.

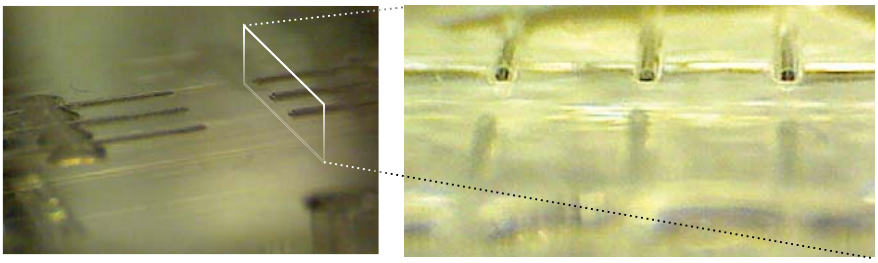

Figure 4.3: Details of embedded fibers in the laser-fabricated PMMA substrate for biofilm monitoring as well as SEM images of the micro-nanometric surface patterning,

4.2.3 Encapsulated SU-8 waveguides

Polymer micromachining technologies have played a major role in miniaturization engineering in recent years. SU-8 in particular has been widely used in the fabrication of microelectromechanical systems (MEMS), whether as structural or functional element. In relation with LoC devices, one very common usage of SU-8 is the photo-lithographic definition of master moulds for replica moulding. Its chemical resistance, mechanical strength together with very well-established fabrication processes, which allow achieving high aspect ratio micro-structures with vertical side-walls, also have made it a common choice as a structural material. Its high refractive index (n = 1.59 at λ = 633 nm, [Bilenberg et al., 2004]) and optical transparency in a wide wavelength range, including a good part of the visible light regime, make it ideal for the definition of integrated photonic elements [Balslev et al., 2006, **?**, De Pedro et al., 2014, Kim and Meng, 2016]. While the photopatterning of SU-8 on silicon is very well known, the continuing trend towards cost-reduction in MEMS and lab-on-a-chip fabrication demands solutions, where silicon is no longer structural component of the final device. Despite efforts to achieve micropatterning of SU-8 on different substrates[TRUONG and NGUYEN, 2003, Bubendorfer et al., 2007], still most of the processes involving SU-8 are carried out on silicon (Si) wafers. This is not least due to the fact, that the properties of SU-8 can vary strongly depending on the processing conditions. In the following, the results using two approaches for the fabrication of SU-8 waveguides and subsequent encapsulation into PMMA are discussed: The use of commercial grade PMMA sheets as low-cost replacement for silicon wafers in standard photolithographic processes and alternatively the transfer and encapsulation of SU-8 structures from silicon to PMMA layers following a standard photolithography (PL) on silicon.

Fig. 4.4 (a) and (b) show the design footprints of the two PhLoCs comprising SU-8 waveguides developed in the course of this thesis for the monitoring of biofilm formation. Both designs comprise a microfluidic channel (µ-channel) to circulate a bacterial culture as well as input and output waveguides. The latter were implemented at opposite sides of the µ-channel for optical

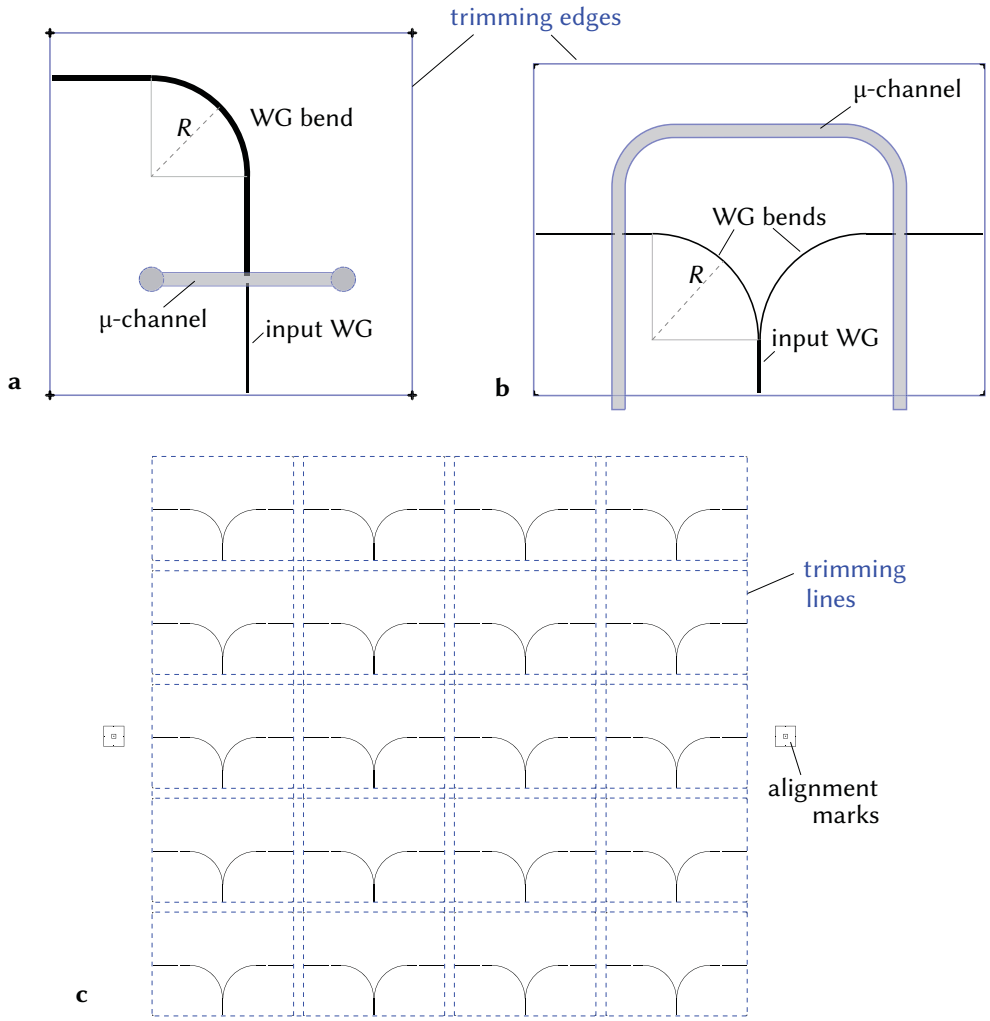

FIGURE 4.4: PhLoC design for integrated waveguides. (a) Footprint of 1st generation PhLoC comprising a single straight in- and bent output waveguide as well as out-of-plane fluidic in- and outlets. (b) Footprint of 2nd generation PhLoC comprising a single WG input splitting into two bend WGs and subsequent straight output WGs for a dual measurement. (c) Periodic repetition of footprint in (b) for wafer-scale fabrication. Alignment marks and trimming lines for final release of individual PhLoCs are also indicated.

measurements across the width of the µ-channel. The waveguide ends by design pierced the side-walls at the level of the µ-channel bottom in order to avoid reflections at the µ-channel walls and enable close contact with the colonising bacteria. Waveguide design was inspired by that used in the previous chapter to evaluate the proposed chip-to-world interface (CWI). Both footprints therefore contain bent waveguide sections with bend radii $R = 4\,\text{mm}$. The motives for the addition of a second measurement site by splitting the optical input in Fig. 4.4 (b) and

the change to lateral fluidic in- and outlets will be clarified in the corresponding sections later on.

4.2.3.1 Photolithography on commercial grade PMMA

Direct PL on PMMA has been reported by TRUONG and NGUYEN [2003], who identify poor solvent resistance and 'bowing' during baking steps as the main problematic aspects of this material as a substrate for SU-8 photolithography and Bubendorfer et al. [2007], who used a 'high grade UV blocking polymer with an antireflective surface' to reduce internal reflection during exposure. Here in contrast, we employed low-cost 'extruded' polymer sheets supplied by a local provider (*Ferreteria Maranges S.A.*). In an initial assessment of suitability we tested the chemical resistance of our commercial substrates against the standard SU-8 developer (mr-Dev 600, Microresist) during a reasonable amount of time. To that end, a laser-trimmed substrate was submerged in the developer solution during increasing time intervals (30 s, 50 s, 100 s and a final 240 s) and dried in a stream of nitrogen for visual inspection. The only visible effect of the treatment after the total 420 s submerged in the developer, which is more than enough to develop SU-8 layers with thickness below 100 µm , were small cracks along the trimming edges, so-called 'stress crazing', appearing first at points of high surface energy like small notches caused by small ignitions of the vaporised PMMA during the laser trimming process. This undesired

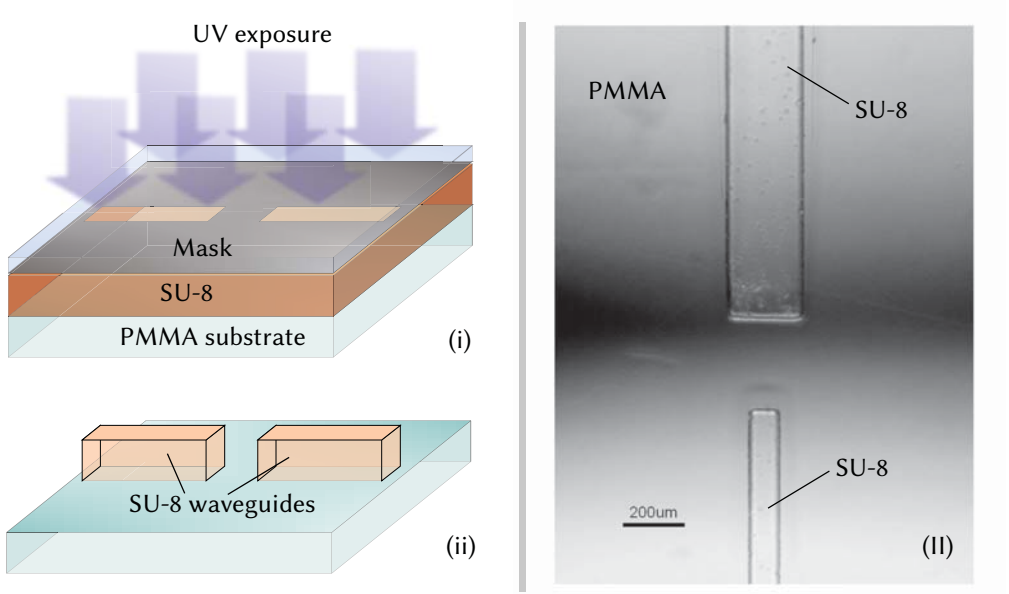

Figure 4.5: Full process scheme for PhLoC fabrication using direct photolithography to create SU-8 waveguides on PMMA substrates. The subsequent thermal embossing of the top-layer unto the bottom layer and laser cutting for PhLoC release produced flame polished optically clear edges.

effect is known to happen as a result of the internal stresses in the material induced during laser cutting and can be reduced by annealing the substrate prior to the application of solvents. In the final PL, this annealing would be covered by the several baking processes. After development it is common in photolithographic processes to rinse samples first with isopropanol for visual inspection and finally with deionised water to stop the reaction. In contact with water however a very thick white precipitate formed on the whole surface of the samples, which could not be removed either by renewed rinsing in developer, nor by rinsing in isopropanol. Water was therefore eliminated from the process. The overall chemical resistance was deemed enough to attempt a direct photolithography on such PMMA substrates. SU-8 waveguides were fabricated on PMMA following the steps of photolithography detailed in the introduction with several modifications to the concrete process parameters. Fig. 4.5 summarises the process in which the essential difference to the one detailed in the introduction (section 1.5.1) is the substrate. As shown in the schematic representation, only the structural layer of SU-8 was spincoated unto the substrate for the definition of waveguides. A set of different spin-coating conditions according to Table **??** was applied to characterise the resulting layer thickness under the modified process conditions. For the soft-bake, the baking temperature was ramped in two steps from 35°C to 50°C with a relaxation time of 10 min and from 50°C to 70°C , at which it was kept during another 30 min to 60 min depending on the layer thickness. The exposure dose was doubled as compared to the recommended one for processing on silicon wafers to compensate for the transparent substrate. The PEB was also performed in two steps; 35°C to 50°C ramp, 10 min relaxation and a subsequent ramp from 50°C to 75°C , followed by another 20 min at 75°C . Development was performed as previously established by submerging the exposed samples in mr-Dev 600 (maximum development time 5 min and 30 s), subsequently rinsing with isopropanol and drying in a stream of nitrogen. The resulting layer thickness was assessed after development using a mechanical profiler (Tercor alphastep 200). The microscope image on the right-hand side of Fig. 4.5 shows two of the SU-8 waveguides fabricated on PMMA as descibed.

It should be mentioned at this point, that the overall yield of the process was not as good as could be expected in sight of this data. Several attempts failed upon development, where albeit

Resist	Spin-coating (closed lid)	Sof-bake at 70°C (min)	Exposure dose ($mJ\,cm^{-2}$)	Film thickness (µm)
SU-8 2005	15 s at 400 rpm, 30 s at 3000 rpm	30	200	2.87
	15 s at 400 rpm, 30 s at 1000 rpm	30	200	4.39
	2×(15 s at 400 rpm, 30 s at 1000 rpm)	40	300	9.23
	2×(15 s at 400 rpm, 30 s at 500 rpm)	40	300	13.35
SU-8 2025	15 s at 400 rpm, 30 s at 3000 rpm	60	400	29.95
	15 s at 400 rpm, 30 s at 1000 rpm	60	400	89.07

Table 4.1: Photolithography on PMMA: Process conditions and resulting layer thickness.

unexposed material not yet being fully removed, the waveguide structures were 'lifted off' the substrates. This effect increased with decreasing contact area of the waveguides as well as for shorter exposure times, suggesting that the substrate surface may indeed not be as chemically resistant to the developer as assumed. Between batches of purchased PMMA substrate sheets in particular the chemical resistance varied considerably. This strong variation between batches was mainly due to purchasing not from the manufacturer directly, but from a local intermediary, who purchases from different sources depending on the current market price. The concrete factors leading to failure could therefore unfortunately not pinned down to concrete differences in materials. We therefore proposed an alternative and more predictable fabrication strategy, also with a higher degree of novelty, which is presented following.

4.2.3.2 Transfer from silicon wafers to PMMA

> The content of this and the following two subsections was successfully submitted as an abstract to MNE conference 2017 in Portugal and will be presented there as a poster.

In contrast to the prior approach, the photolithography process itself was not altered, but carried out as previously described (compare section 1.5.1) on silicon wafers. Instead, we propose the transfer of the fabricated waveguide by encapsulation into PMMA via thermoforming and subsequent de-lamination.

To process SU-8 in the traditional way on silicon and subsequently transfer the patterned structures to a more convenient and less costly substrate like the PMMA used in this work may be a promising compromise, which has the positive side-effect that the silicon wafers may be recycled after a short rinsing in acetone and re-used. Typical approaches to separate SU-8 structures from the substrate include the use of sacrificial release layers consisting of metal films or other polymers, which are removed by a wet chemical process [Kim and Meng, 2016]. Here, we make use of the relatively poor adhesion strength between SU-8 and Si/SiO_2 promoting delamination [Larsson et al., 2005], which is often reported as a cause for failure in SU-8 moulds for soft-lithography [Bubendorfer et al., 2007] or hot-embossing [Shamsi et al., 2014], combined with the strong adhesion to poly-methylmetacrylate (PMMA) [Bilenberg et al., 2004] to transfer SU-8 micro-structures from silicon wafers onto thermoplastic PMMA and encapsulate them as integrated waveguides in an all-polymeric photonic lab-on-a-chip.

In a first step, 60 µm thick SU-8 waveguides (SU-8 2025, MicroChem Corp.) were defined on a

4" silicon wafer with 4000 Å thermally grown oxide (SiO_2) by standard photolithography. Note that no seed layer was applied before spin-coating of the structural layer. The resulting waveguides (compare Fig. 4.6 (i) and (I)) were at this point directly adhered to the thermal oxide of the substrate. A 2 mm thick top-layer with 500 µm wide microfluidic channels was prepared from a commercial grade PMMA sheet by micro-milling with a Roland MDX-40A bench-top milling machine and cut to size with the Epilog Mini 24 CO_2 laser. Once aligned such that the microfluidic channels connected the waveguide end-facets on both sides (see Fig. 4.6 (ii/II)), substrate and top-layer were inserted in a press (P.O. Weber) with temperature control on both plates (see Fig. 4.7 (b)). Alignment throughout the process was assured by applying UV-curable glue (NOA 68, *Norland Products, Inc.*) on both sides of the wafer.

Waveguide encapsulation in the top-layer PMMA was achieved by applying the temperature

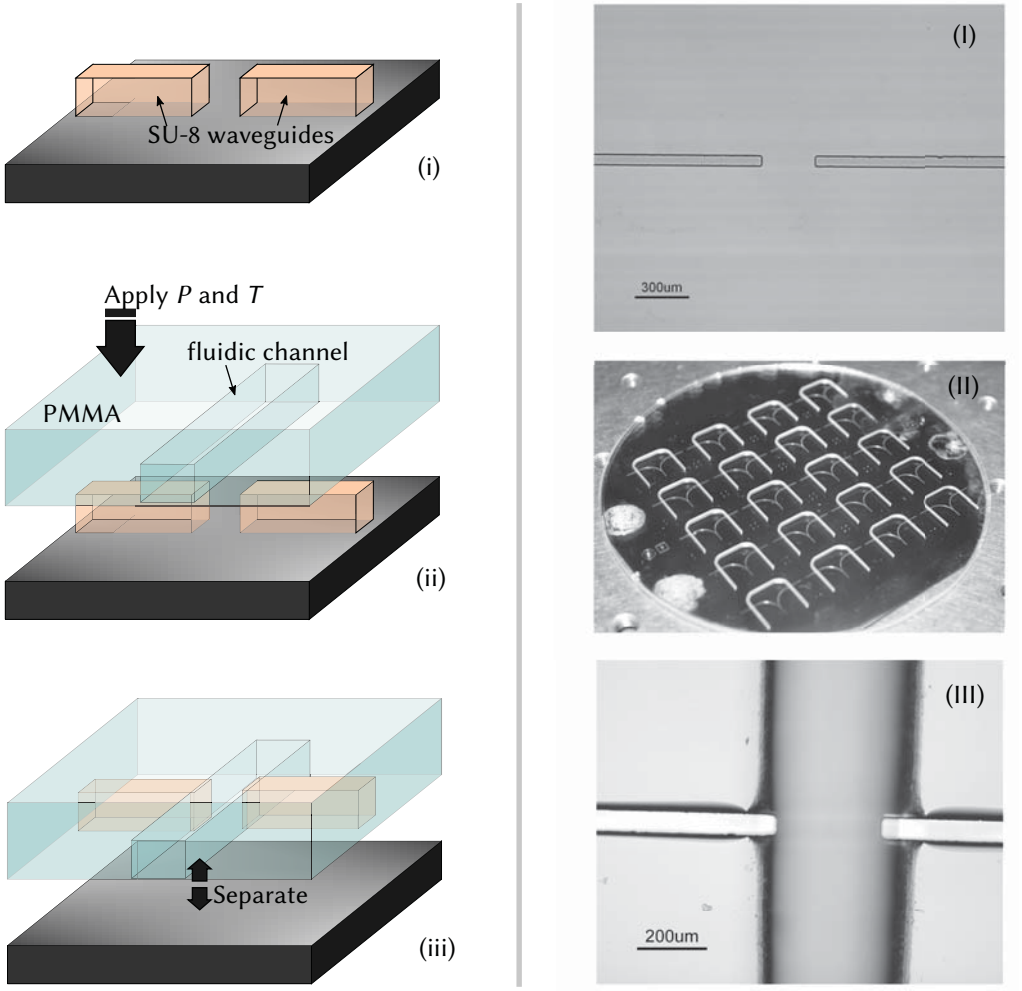

Figure 4.6: Summary of the waveguide transfer process. Left: Schematic representation of the process flow; Right: Microscopy images and photographs of individual steps during fabrication.

and pressure profile detailed in Fig. 4.7. By raising the temperature of the plate in contact with the Si substrate above the glass transition temperature T_g(≈ 105° C) of PMMA and keeping the other plate well below T_g, the geometric integrity of the microchannels was maintained while the waveguides were fully embedded in the PMMA matrix. After slow cooling, the PMMA sheet could be easily released from the Si substrate. The SU-8 waveguides remained enclosed on three sides by the PMMA matrix and thus also detached from the Si wafer (see Fig. 4.6 (iii/III)). The latter was cleansed with acetone to remove polymer residuals and could be re-used as a substrate.

4.2.4 Wafer-scale alignment

To perform the alignment of layers outside of the cleanroom, the alignment setup shown in Fig. 4.8 was assembled. The setup comprised all the necessary elements for that purpose as they are present in every cleanroom mask-aligner. The motorised stage as well as the cameras were controlled via the python modules implemented in *MyOpticsLab.py*, which was introduced earlier in section 3.3.3 and optionally loads the stage module *MyStage.py*, which can be found in the appenices in section B.

Two problems arose upon application to the thermoplastic layers: On the one hand, alignment

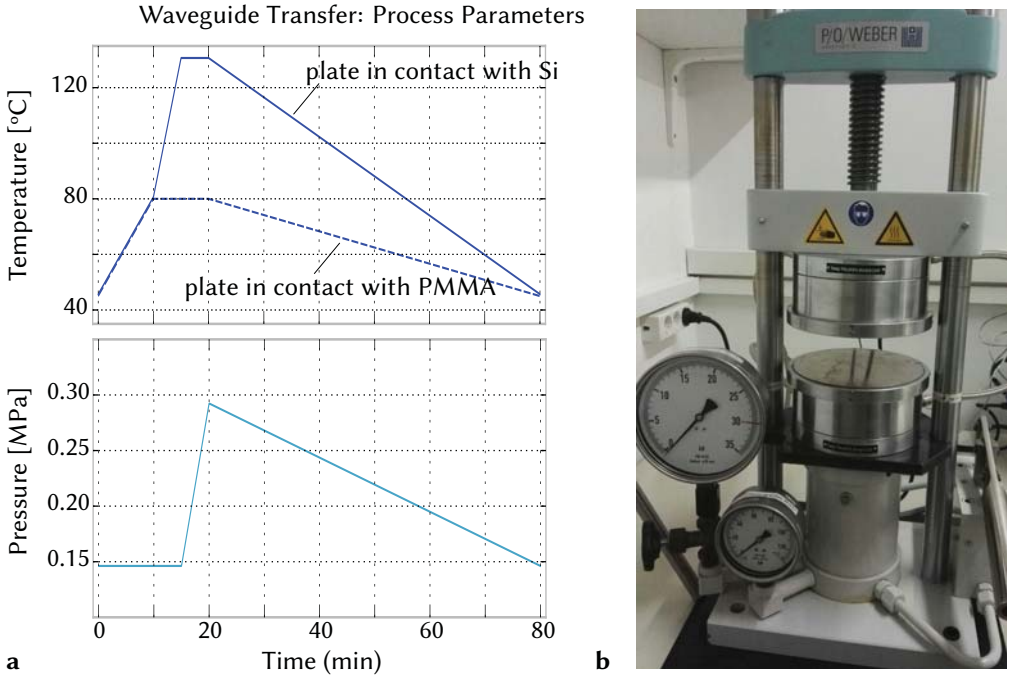

Figure 4.7: a) Temperature and pressure profile applied in step (iii, Fig. 4.6) of the process flow; the embedding of SU-8 waveguides in the PMMA toplayer. b) Photograph of the thermal press used in the process.

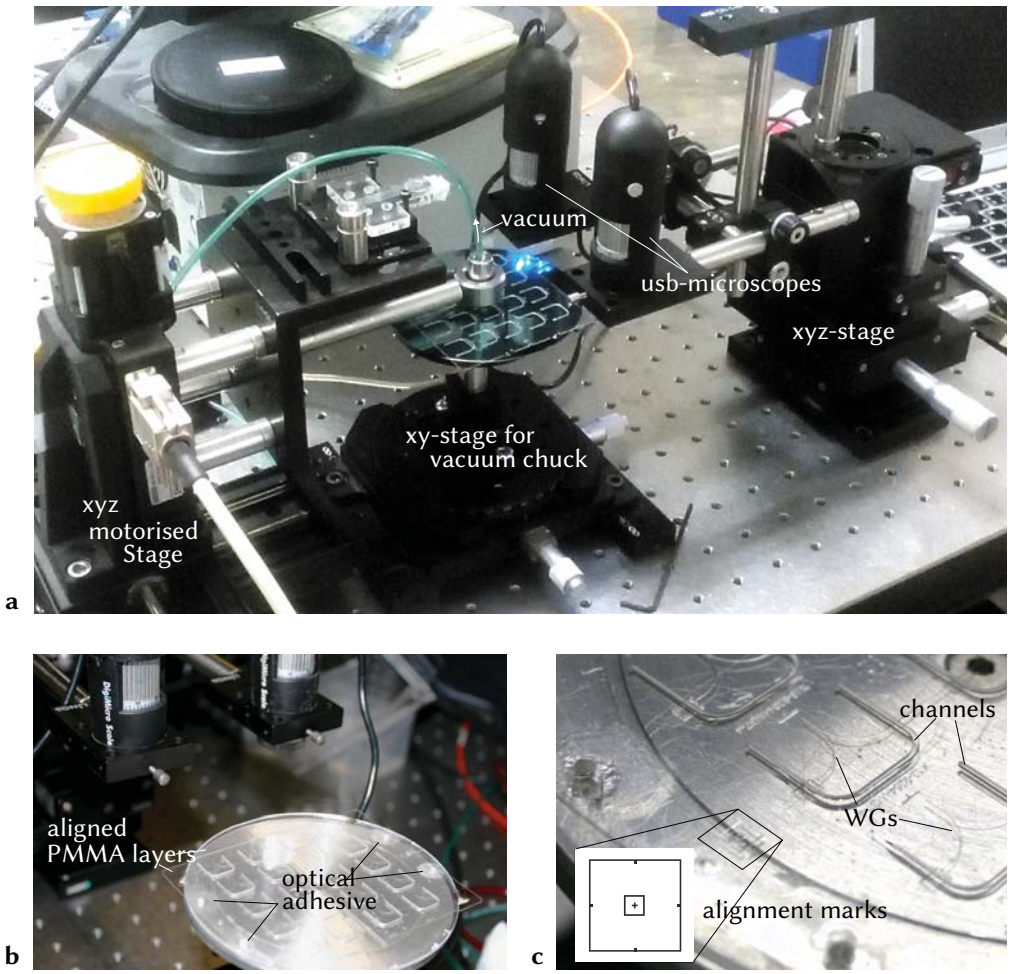

Figure 4.8: Setup for alignment of layers. a) Photograph of the complete setup comprising micro-controllers and vacuum for controlled xyz-movement of both layers (here a silicon wafer with SU-8 waveguides on the bottom and a PMMA top-layer to be aligned) and two usb-microscopes for visual feedback of coincidence of alignment marks; b) Detailed photograph of the chuck holding aligned and fixed PMMA bottom and top-layers after successful waveguide transfer; c) Detail of (b) showing the individual elements contained in the layers.

elements had been applied into the PMMA layers together with the fluidic channels. The precision of positioning and the fidelity in shape of these elements was unfortunately not good enough using the available equipment to achieve well-aligned motives on the scale of the whole wafer. In particular, rotational inaccuracy was difficult to appreciate beforehand (while aligning) despite the elaborate setup. On the other hand, using extruded PMMA sheets, the thermal treatment involved in the waveguide transfer or photolithography process previously described made structural inhomogeneities apparent in form of non-uniform thermal expansion. The slight deformations of substrates induced by such effects were in some cases enough to inhibit proper alignment across more than $(5 \times 5)\,\mathrm{cm}^2$. These two factors in particular reduced the overall yield of the fabrication process.

In spite of the inconvenience they caused in this particular work, the solution of these problems appears quite straight-forward in terms of a more industrial fabrication with a switch to better quality 'cast' PMMA and the use of more precise equipment for laser-processing or milling.

4.2.5 Thermal bonding vs. thermoforming to seal µ-channels

Depending on the fabrication strategy followed for the SU-8 waveguides, a second PMMA layer had to be aligned bonded to the first. Direct PL left us with a PMMA substrate with SU-8 waveguides defined on the surface but without microfluidic channels (µ-channels), waveguide transfer with a PMMA top-layer with SU-8 waveguides already embedded in the walls of their respective microfluidic channels. Consequently, in the first case a top-layer containing microfluidic channels needed to be bonded and thermoformed at the same time to encapsulate the SU-8 waveguides, in the second case only a flat bottom-layer needed to be added to seal the microfluidic channels. This difference, for now a mere case-dependent technological requisite, will become more relevant later-on. Fig. 4.9 shows a schematic representation of the two situations and the corresponding temperatures T and pressures P applied with the thermal press previously depicted in Fig. 4.7. The pressure profile $P(t)$ applied to 'thermoform' and bond the layers depicted on the left-hand side was the same as shown previously in Fig. 4.6 in relation with the WG-transfer. In the situation on the right-hand side, applying a pressure of $P = 7kN$,raising the temperature to 95°C ($< T_g \approx 105$°C) and keeping those conditions for 20 min was enough to ensure leak-free µ-channels without compromising the shape of the - at that point hollow - structures. Fig. 4.10 shows microscope images both described situations after thermoforming (Fig. 4.10 a) and bonding (Fig. 4.10 b), respectively. The apparent difference in µ-channel width stems from the usage of laser-engraving for the definition of µ-channels in the former and micro-milling in the latter case.

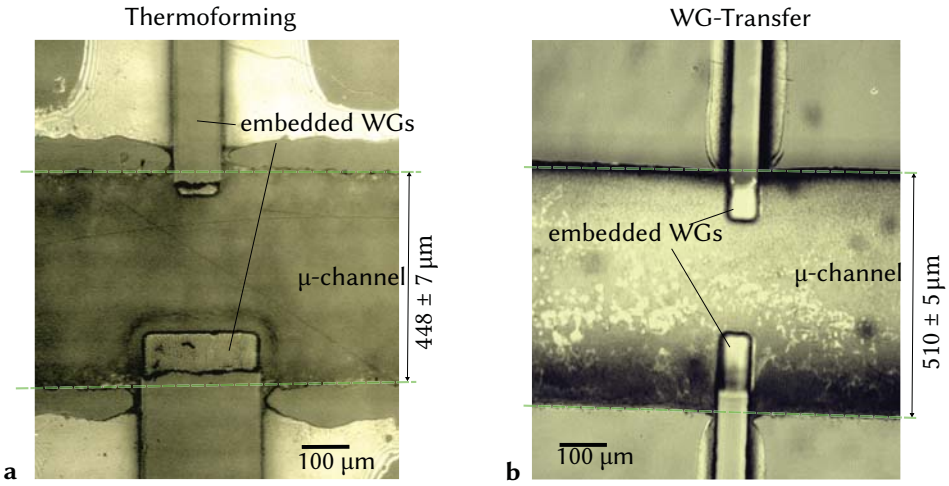

Figure 4.10: Microscope images of sealed PhLoCs comprising SU-8 waveguides integrated using direct PL (left) or WG-transfer (right), respectively.

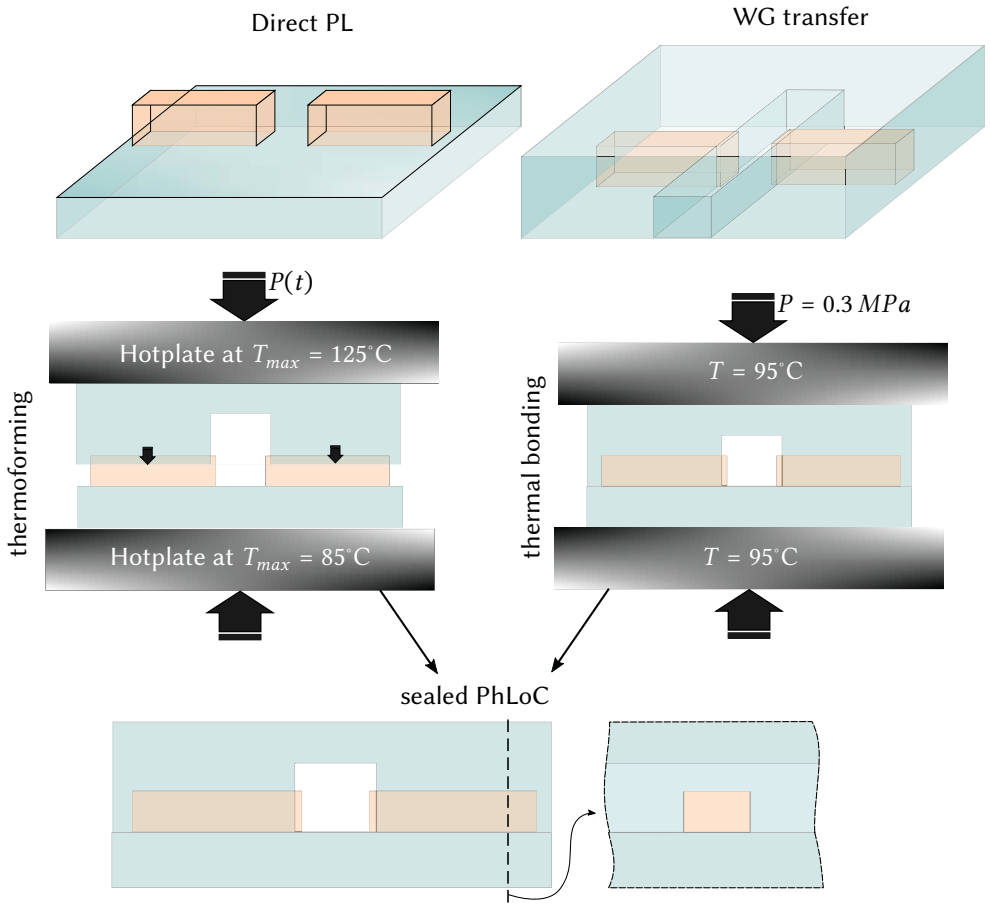

Figure 4.9: Schematic representation of bonding and sealing of PhLoCs comprising SU-8 waveguides integrated using direct PL or WG-transfer, respectively.

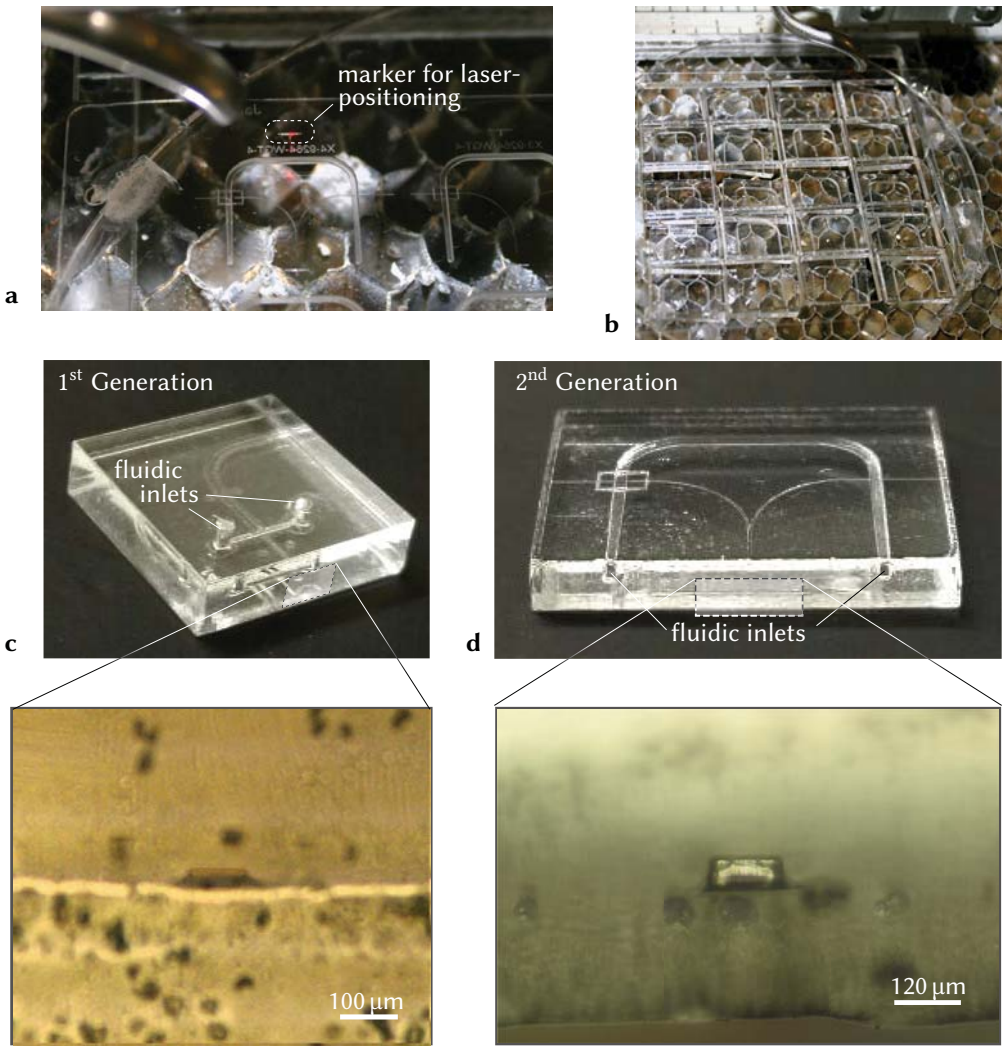

Figure 4.11: Photographs of the trimming process (a, b) and examples of the released PhLoCs with flame-polished optical quality edges.

4.2.6 Laser-trimming

As shown in Fig. 4.11 (a) and (b), individual chips were released subsequently by CO_2 laser cutting. By positioning the laser-head via an incorporated red laser-diode in the xy-plane on the alignment marks as indicated in Fig. 4.11 (a), subsequent trimming could be realized semi-automatically at relative positions. For best results, every column was newly aligned manually. Again, the accuracy of the process could be greatly enhanced using a laser-cutter with alignment functionality already implemented. In this last step, the edges of the individual PhLoCs were fused. Apart from adding robustness to the bonding achieved in the prior sealing procedures described above, the laser-cutting resulted in optically clear side-facets, as can be appreciated

in Fig. 4.11 (c) and (d) and the respective microscope images detailing the end-facets of the encapsulated input waveguides.
The possibility of achieving such optically clear cutting edges in the same step as separating individual PhLoCs with no need of further post-processing was one of the main motives for the choice of PMMA as structural material in the first place.

4.2.7 Optical characterisation

In order to demonstrate the performance of devices fabricated with the proposed process flow, optical calibrations were performed using aqueous solutions of different analytes to measure particle scattering, absorption and emission. Optical and fluidic connections were established using a chip-to-world interface designed and fabricated like the one presented previously in chapter 3. Aqueous solutions of fluorescein, crystal violet (CV) and latex beads purchased at *Sigma-Aldrich Co. LLC* as well as blue food colorant E-131 were used for device evaluation.

First generation

Fig. 4.13 shows the results of scattering and absorption assays, Fig.4.12 the emission detection calibration performed with the first generation PhLoC. In each case, the analyte was introduced in aqueous solution at different concentrations and the absorbance signal obtained in the visible range as a function of the wavelength. The presented spectra were smoothed using a Savitzky-Golay filter[1] with a polynomial order of 5 and a filter window of 105 pixels (at 1044 pixels total array length). Subsequently, the absorbance values as a function of analyte concentration were evaluated for each wavelength using a best fit (based on R^2 of the linear regression) criterion and calculating the Limit of Quantification (LOQ) as

$$LOQ = 10\sigma_i/S \ , \tag{4.1}$$

[1]Savitzky-Golay filter from the Scipy.Signal module (see website docs.scipy.org)

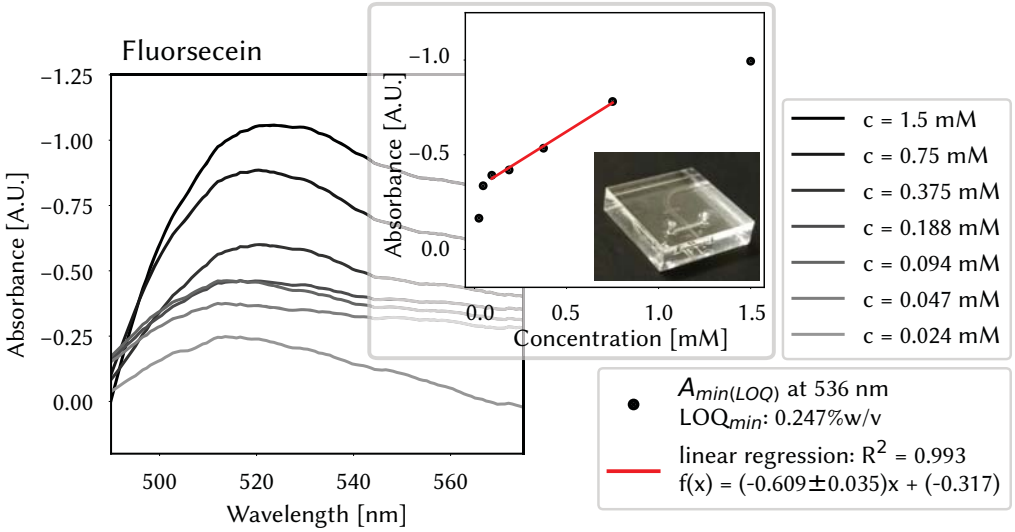

Figure 4.12: Absorbance spectra of aqueous dilutions of a 1.5 mM solution of Fluorescein injected in the PhLoC and measured across the μ-channel.

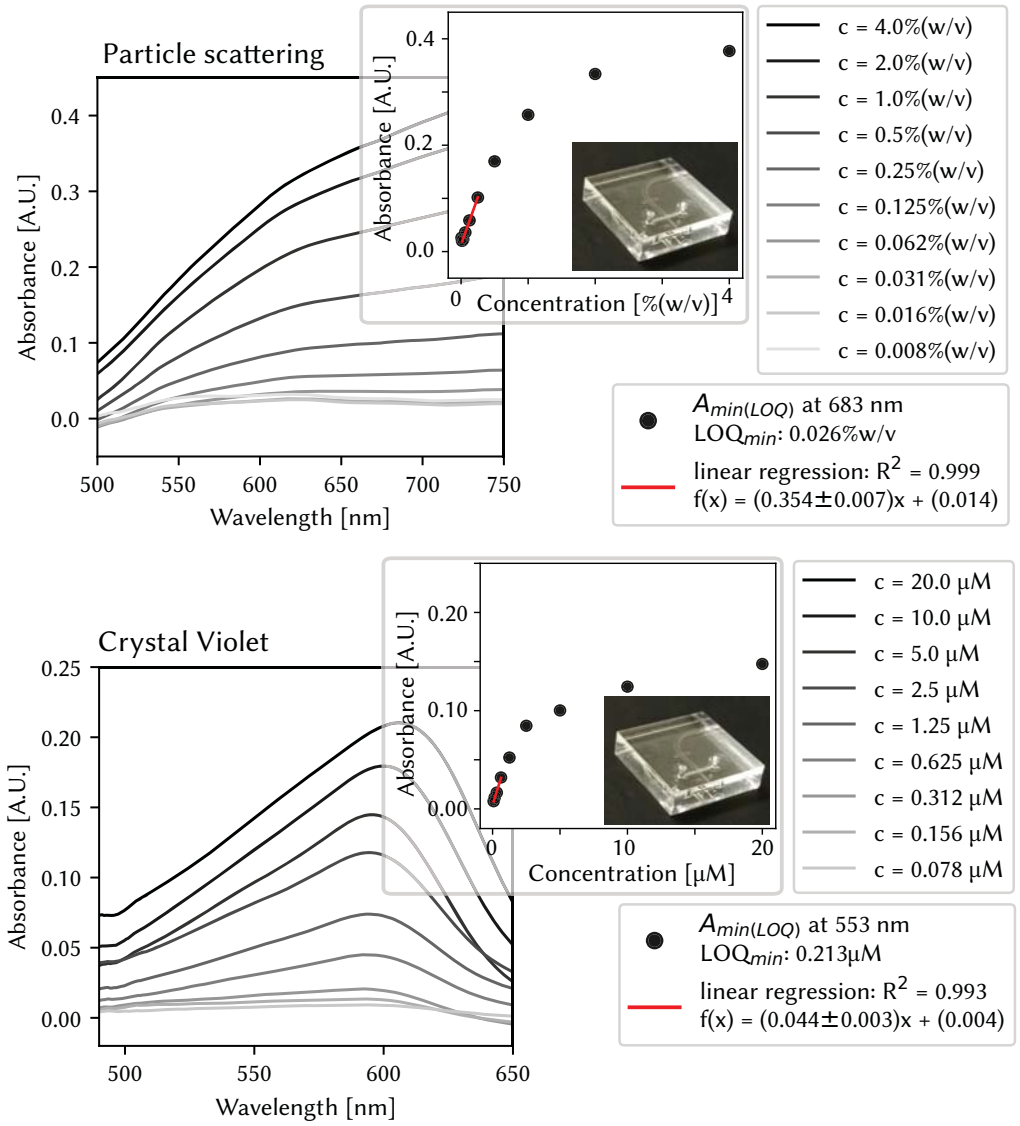

FIGURE 4.13: Top: Absorbance spectra of aqueous suspensions of 2 µm diameter polystyrene beads with indicated weight/volume fractions injected in the PhLoC and measured across the µ-channel. Bottom: Absorbance spectra of aqueous dilutions of a 20 µM solution of Crystal violet (CV) injected in the PhLoC and measured across the µ-channel.

where σ_i is the intercept error of the linear regression and S the sensitivity to the given analyte, obtained from the slope of the linear regression. The calibration curve for the wavelength yielding the best value for LOQ is plotted in each case as an inset to the absorbance spectrum. As can be seen from the plots, the first generation PhLoC yields the best $LOQ = 0.026\%(w/v)$ for the 2 µm sized polystyrene beads at 623 nm at a sensitivity of $S = (0.354 \pm 0.007)$ A.U./%(w/v).

For Crystal Violet detection, the minimum $LOQ = 0.213\,\mu M$ was obtained at a wavelength of 533 nm at a sensitivity of $S = (0.044 \pm 0.003)$ A.U./µM. Finally, for fluorescence emission detection the minimum $LOQ = 0.247$ mM was measured at a wavelength of 536 nm and the obtained sensitivity was $S = (-0.609 \pm 0.035)$ A.U./mM.

Second generation

Absorption detection. For the evaluation of the second generation PhLoC, the absorbance of food colorant E131 was measured in different concentrations and in this case the results were compared to cuvette measurements of the same solutions. Optical and fluidic connections were again established using a chip-to-world interface designed and fabricated like the one presented previously in chapter 3. The results, normalized to absorbance units per centimeter (A.U. cm^{-1}) for better comparison with the data measured in the cuvette are shown in Fig. 4.14. As apparent from the plots, after extrapolating the absorbance signal obtained using the PhLoC to an optical path length of 1 cm as present in the cuvette, the maximum absorbance measured in the experiment was almost 1.5 times higher than the one measured with a conventional cuvette and yielded a sensitivity of $S = 0.15$ A.U./(mg L^{-1}) for the PhLoC as opposed to $S = 0.09$ A.U./(mg L^{-1}) for the cuvette. However, the in this case not smoothed absorbance spectra reveal that the shorter optical path results in a much lower signal-to-noise ratio in the PhLoC than in the cuvette.

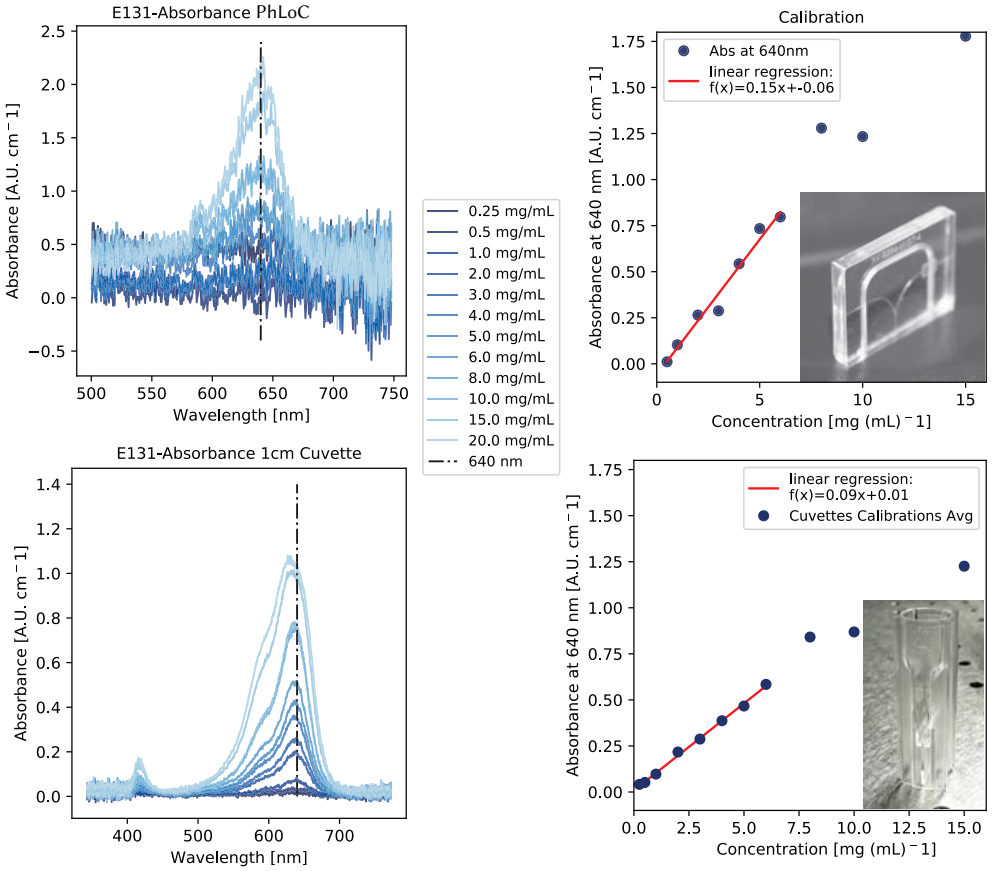

Figure 4.14: Colorimetric measurements of food colorant E131 in aqueous solutions. Left: Absorbance spectra obtained at different concentrations of E131. Right: Corresponding calibration at the wavelength of the absorption peak; 640 nm. The wavelength is indicated by the dashed line. The data in the first row corresponds to the PhLoC shown in the inset of the calibration graph, the second row to comparable measurements in a commercial cuvette. Units are normalized to an optical path of 1 cm.

4.3 Surface colonisation kinetics on PMMA

Now that the fabrication strategies and materials were determined, the next development step was the proper characterisation of the (living) species to be studied. In the case of living specimen it is of paramount concern how the organism will react upon contact with the particular materials involved in the device fabrication. As biofilms are famous for their ubiquity, we were in this case not so much concerned with *if* the bacteria would colonize a PMMA surface, but rather *how* and especially: *How fast?* .

4.3.1 Bacterial culture

Pseudomona putida (*P. putida*) was chosen as one model bacterium for presenting high capacity to colonize surfaces and to create thick biofilms after short exposition times. On the other hand, a strain of Escherichia coli (*E. coli 25922GFP*) expressing a green fluorescent protein (GFP) mutation (GFPmut3) with main excitation band at 501 nm and main emission at 511 nm was purchased at ATCC and employed to correlate biofilm growth with a specific spectral response, as the inherent fluorescence allowed for label-free microscopic inspection parallel to optical measurements. Bacterial suspensions were grown overnight in minimum medium AB (MMAB) supplemented with 0.2% glucose (w/v) at 30°C in a thermal bath agitator. Overnight cultures were centrifuged and re-suspended in MMAB. The optical density of the final suspension was adjusted by dilution with deionised water to 1 absorbance unit (A.U.) at 550 nm with MMAB, which corresponded to a bacterial concentration around 10^8 colony forming units per mL (CFU/mL).

4.3.2 Bacterial surface colonisation of untreated PMMA

As an initial assay, we immersed a series of laser cut but otherwise untreated samples in said over night culture containing 10^8 CFU/mL *Pseudomona Putida (P. putida)* during one week without addition of further nutrients.

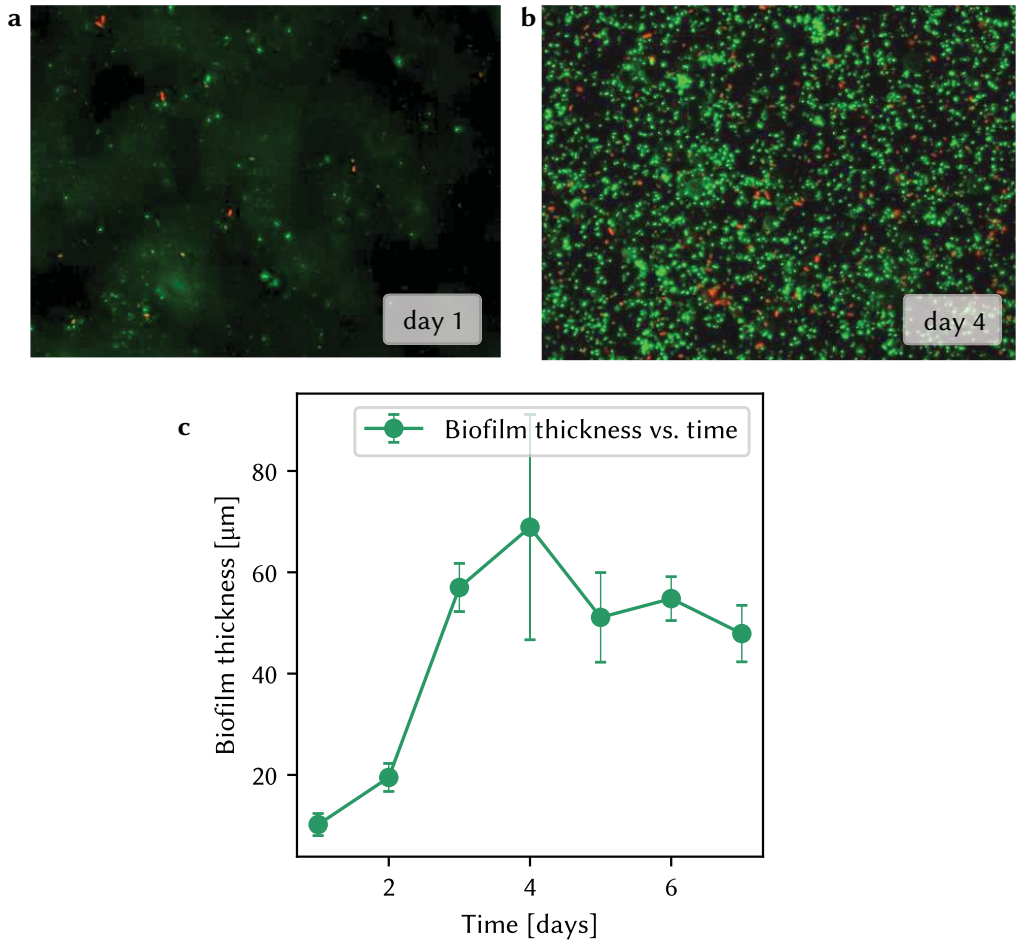

Figure 4.15: Biofilm growth kinetics on laser-trimmed but otherwise untreated PMMA. Biofilm thickness is plotted as a function of time, the error bars indicated the standard deviation of the measurement ($N = 10$). Examples of microscope images at two different times are shown at the top.

The use of a nutrients depleted medium such as MMAB, without additional nutrient delivery or oxygenation, promoted bacterial colonization of surfaces and biofilm formation. Each day one sample was retrieved, flushed with deionised water, stained with a live/dead kit (Invitrogen) consisting of a green and a red fluorescent stain and inspected in a pseudo-confocal microscope to determine the biofilm thickness at 10 different positions across the surface. Green stain is a membrane permeant and non-fluorescent until activated by intracellular activity whilst red stain only penetrates the damaged membranes of non-viable cells and is activated when fixed to the DNA. Fluorescent emission for activated stains is 30 times greater for red, thus UV illumination was enough to obtain the characteristic green/red images. Determining the position of top and bottom biofilm layers by focussing them allowed an approximate measurement of biofilm thickness. The results are shown in Fig. 4.15.

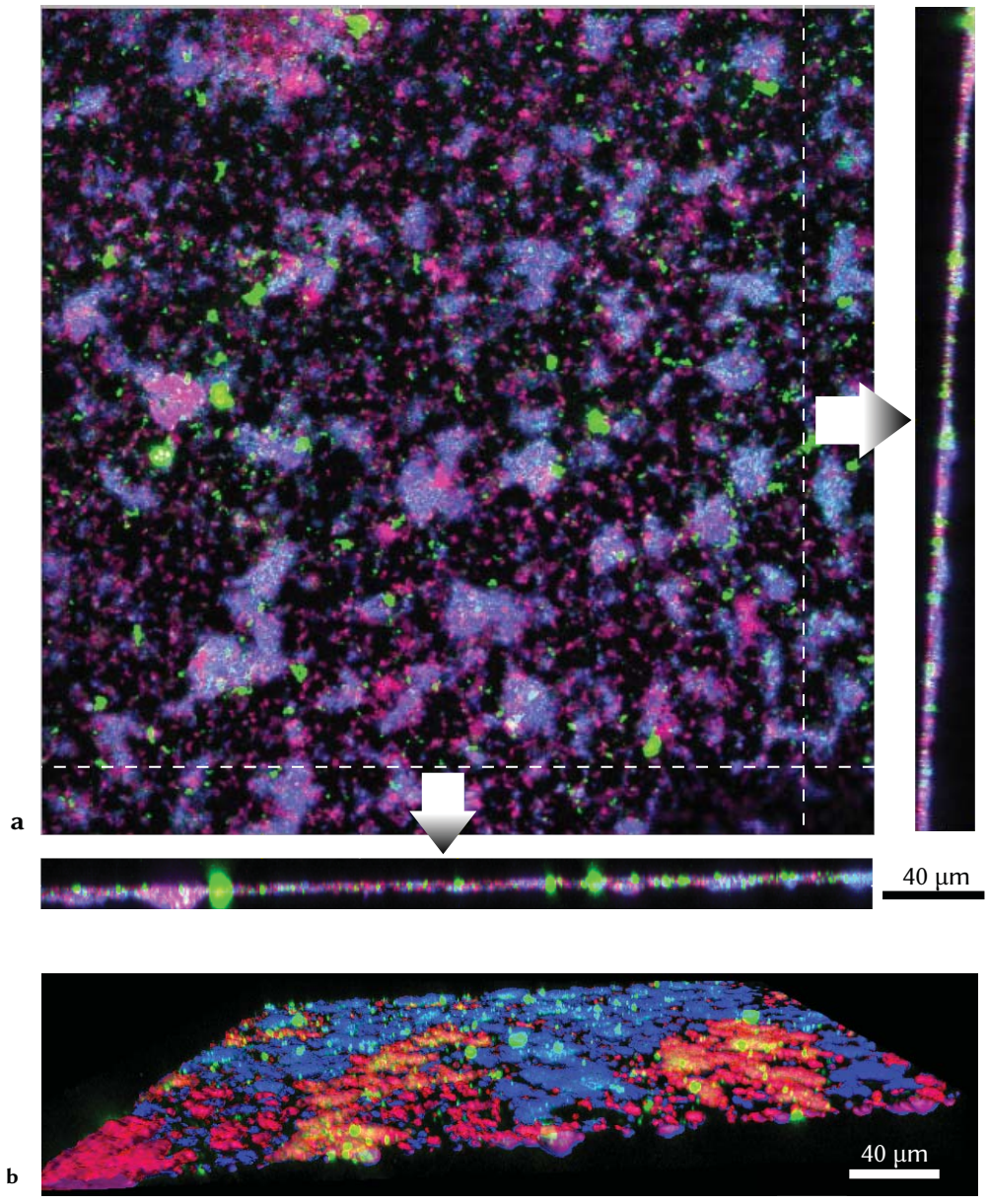

Figure 4.16: Confocal microscope images of stained biofilm with blended colorcode. Three different staining methods have been used in order to stain all the constituen parts of the biofilm: Wheat germ agglutinin (WGA) binds sialic acid and N-acetylglucosaminyl sugar residues (red tones), Concanavalin A binds to alpha-mannopyranosyl and alpha-glucopyranosil residues (green tones) and Hoechst stains bind to DNA (blue tones). (a) Top view with profiles on each edge, (b) 3D representation.

After an initial exponential growth during the first three days, the biofilm thickness stabilized at approximately 60 µm . Subsequent measurements oscillated between 70 µm and 50 µm . We therefore associated the first two to three days with the initial stages of biofilm formation as pre-

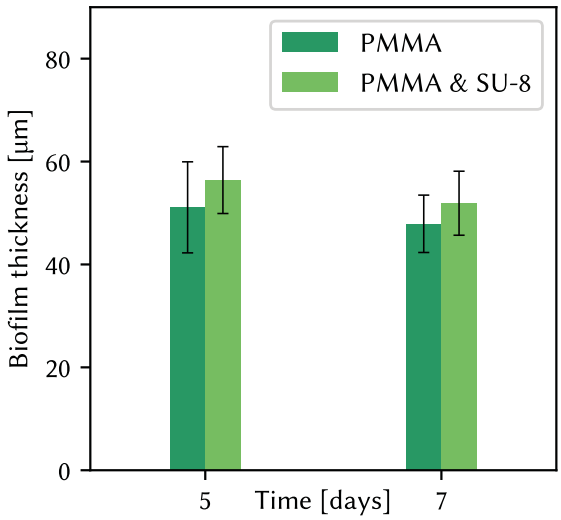

Figure 4.17: Comparison of biofilm thickness on an untreated PMMA surface as opposed to a substrate with photolithographically defined SU-8 micro-structures.

sented previously in Fig. 4.1; initial adhesion, irreversible attachment and completion of biofilm formation. The oscillation in biofilm thickness observed afterwards are typical for biofilms during three dimensional growth, as parts of the mature biofilm are released as planktonic bacteria or aggregates upon reaching a critical mass. While the staining with the live/dead kit provides valuable information about the state of the bacteria, it does not provide much information about the overall structure of the biofilm, which consists apart from bacteria also of a variety of extracellular polymeric substances. Fig.4.16 shows a completely stained biofilm formed as before of *Pseudomona Putida (P. putida)* on an untreated surface of commercial grade PMMA in a static solution of growth medium and bacteria after 5 days. The reconstruction obtained from confocal microscope images at different heights inside the biofilm allowed viewing the overall structure from different perspectives. The blue stains visible in the picture bind to DNA, which should make it possible to appreciate where bacteria are located, the red and green stain binds to different components in the EPS. The colors are overlayed in the representation, so that composite colors inform about the presence of multiple stained biofilm components in the same are. Fig. 4.16 (a) contains a 2D top-view of a biofilm section as well as transverse profiles along the edges. In the latter especially it can be appreciated nicely how the biofilm, albeit heterogeneous in composition, covers the surface in a continuous layer of biomass. Fig. 4.16 (b) displays a complete three dimensional representation.

4.3.3 Effects of photolithography and SU-8 micro-structures

In order to explore if and how biofilm growth on such surfaces may be affected by the photolithography process proposed earlier, a PMMA substrate carrying already developed SU-8 waveguides fabricated according to the protocol in section 4.2.3.1was submitted to an overnight bacterial culture as in the previous experiment together with an untreated PMMA substrate for comparison. We determined biofilm thickness on both substrates after 5 and 7 days in the culture medium as described above. The resulting measurements ($N = 10$) are shown in Fig. 4.17. Taking into account the standard deviation indicated by the error bars, the graph shows no significant differences between the two substrates. Also, the bacterial population was distributed uniformly across the surface and according to the live/dead staining mainly live cells were present. Hence, the photolithography process and the presence of cured SU-8 micro-structures do not appear to have a measurable effect on biofilm colonisation, as far as this microscopic method of measurement is able to resolve.

4.3.4 CO_2-laser micro-patterns for preferential adhesion

In a further characterisation step, the effect of superficial micro-patterns engraved on the PMMA surface by CO_2-laser in different process conditions was explored. Surface roughness and electrostatic interactions have been reported as principal factors promoting bacterial adhesion in the initial stage of surface colonisation Karatan and Watnick [2009]. If applied in localised areas, this fact could be made use of for the early detection of surface colonisation. CO_2-laser ablation offers an easy way of achieving the latter without adding further technological complexity to the proposed microfabrication processes. The effects of such laser-induced surface alterations were therefore investigated in a similar way as described in the previous sections. A design-wise uniform triangular engraving pattern was applied to 1 mm thick PMMA substrates using different sets of the process parameters laser power P and scanning speed S, which will be denominated in the following as PX/SY, X being a percentage of the maximum laser-power and Y a percentage of the maximum scanning speed, respectively. Concretely, parameter sets chosen to span the range between resulting in a quite pronounced engraving (visible well with the bare eye) and barely scratching the surface (engraving barely visible under optical microscope). Fig. 4.18 (a) shows microscope images of the four engravings, labelled with their respective process parameters. The kinetics of biofilm formation were assessed as previously described. For microscopy imaging, PMMA samples were introduced in individual 25 mL flasks containing 15 mL of 10^8 CFU/mL bacteria in MMAB (supplemented with 0.2% w/v glucose) and incubated in a thermal bath agitator at 30°C . As before, nutrients-depleted medium MMAB was used without

additional nutrient delivery or oxygenation to promote bacterial colonization of the surfaces and biofilm formation. After two days, the samples were retrieved for microscope inspection, gently washed three times with distilled water to eliminate non-adhered bacteria and stained with the live/dead kit. An example of the resulting microscope image is shown in Fig. 4.18 (b) for each engraving condition. According to these images, there was indeed a visual increment of cell population in some areas, which we associate with the engraved patterns. Curiously, the optically less visible pattern produced by process parameters *P*05*S*20 appeared to provoke the a far more pronounced effect. For a quantitative assessment of these facts, the thickness of the biofilm layers was estimated as before using the focal plane of the pseudo-confocal microscope in patterned as well as un-patterned areas. Additionally, the density of micro-organisms in the biofilm was assessed using imageJ[2] to process areas corresponding in the microscope images to areas in- and outside the pattern. Graphic representations of the results are shown in Fig. 4.19. As can be seen in Fig. 4.19, the micro-patterning via CO_2 laser ablation induced significant differences between engraved and not engraved areas in each of the investigated process conditions after two days of incubation. The statistical significance applies to biofilm thickness as well as and in particular to the density of viable cells. According to the results, surface colonisation was apparently favourably influenced already after two days. Furthermore, according to these results the optimum condition for preferential adhesion and growth was *P*05*S*20. As a general note, it should be mentioned at this point that due to frequent use of the CO_2-laser and the random error in the focal adjustment of the laser beam with respect to the surface induced by the human factor in the fabrication, comparability of the micro-patterns between batches is not

[2]Open source Image processing software written in Java. (see website)

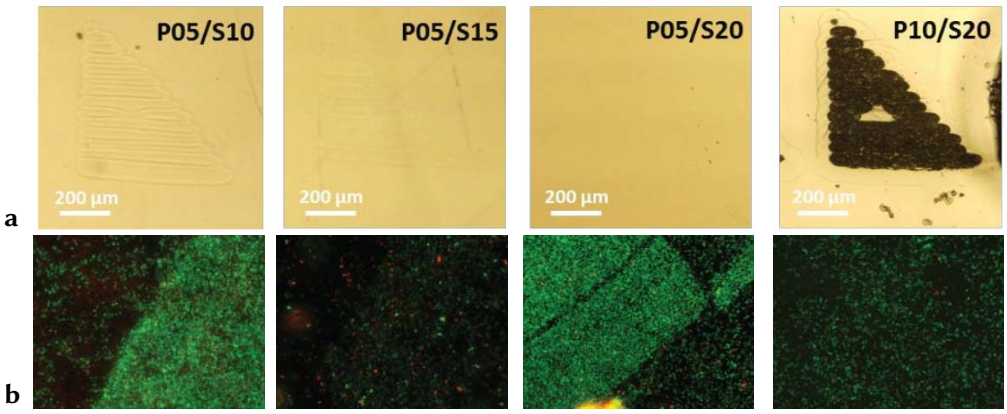

Figure 4.18: Confocal evaluation of biofilm formation kinetics on laser-engraved PMMA substrates. (a) Optical microscope images of the patterns after fabrication. (b) Biofilm grown on the same surfaces after two days of incubation.

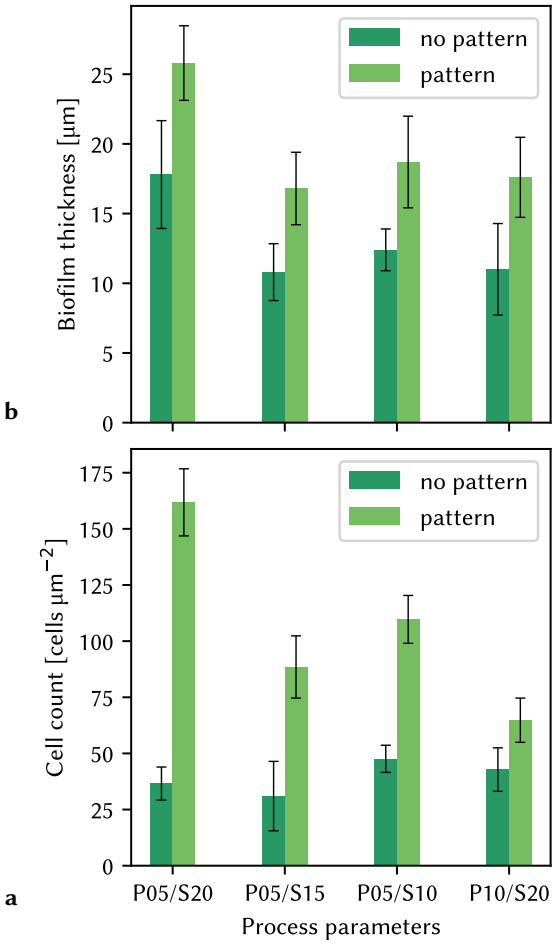

Figure 4.19: Results obtained from confocal evaluation of biofilm formation kinetics on laser-patterned PMMA substrates after two days of incubation. Biofilm thickness (a) and population density (b) were compared in- and outside of the patterns for different process parameters.

safe to assume. Analysis of growth acceleration as a function of patterning conditions as shown here may therefore yield quite different results from batch to batch.

4.4 Monitoring of biofilm colonization: Static conditions.

4.4.1 Experimental design

In order to correlate the prior observations concerning surface colonisation kinetics in static conditions with an optical signal, a *spectral response*, PMMA substrates like the ones previously employed was equipped with embedded fiber-optics, following the fabrication protocol described above in section 4.2.3. The sensing principle would be based on the changes in the visible spectra during bacterial colonization, which may vary from a highly-dispersive scattering spectra for free-floating bacteria and bacterial aggregates to selective absorbance bands for mature biofilms. The chip, fabricated in 10 mm thick poly(methyl methacrylate) to allow easier handling, incorporated thus several sets of fiber-optics (FO) segments facing one another at a distance of 3 mm and aligned in height with the PMMA surface between them.

Micropatterns for preferential adhesion. Based on these prior observations, the experimental design for spectroscopic monitoring of biofilm growth was arranged as depicted in Fig. 4.20. Three measurement zones were created by embedding segments of cleaved 200/230 µm fiber-optics, each zone allowing for triplicate acquisition of the spectral response of the biofilm growing on a surface patterned using the conditions determined previously as 'optimal' for growth acceleration, one not so favourable condition and on the untreated smooth substrate surface.

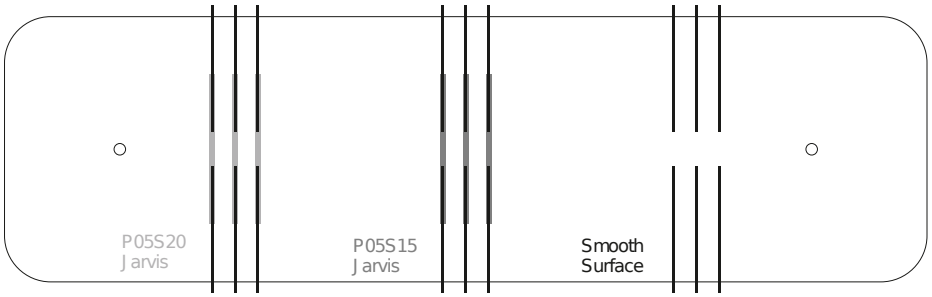

Figure 4.20: Vector-graphics design of the PhLoC comprising triplets of grooves for embedding fiber-optics for each of three different surface conditions.

Bacterial culture. A strain of Escherichia coli (*E. coli*) expressing green fluorescent protein (GFP) was employed to correlate biofilm growth with a specific spectral response, as the inherent fluorescence allowed for label-free microscopic inspection parallel to optical measurements. Bacterial suspensions were grown overnight in minimum medium AB (MMAB) supplemented

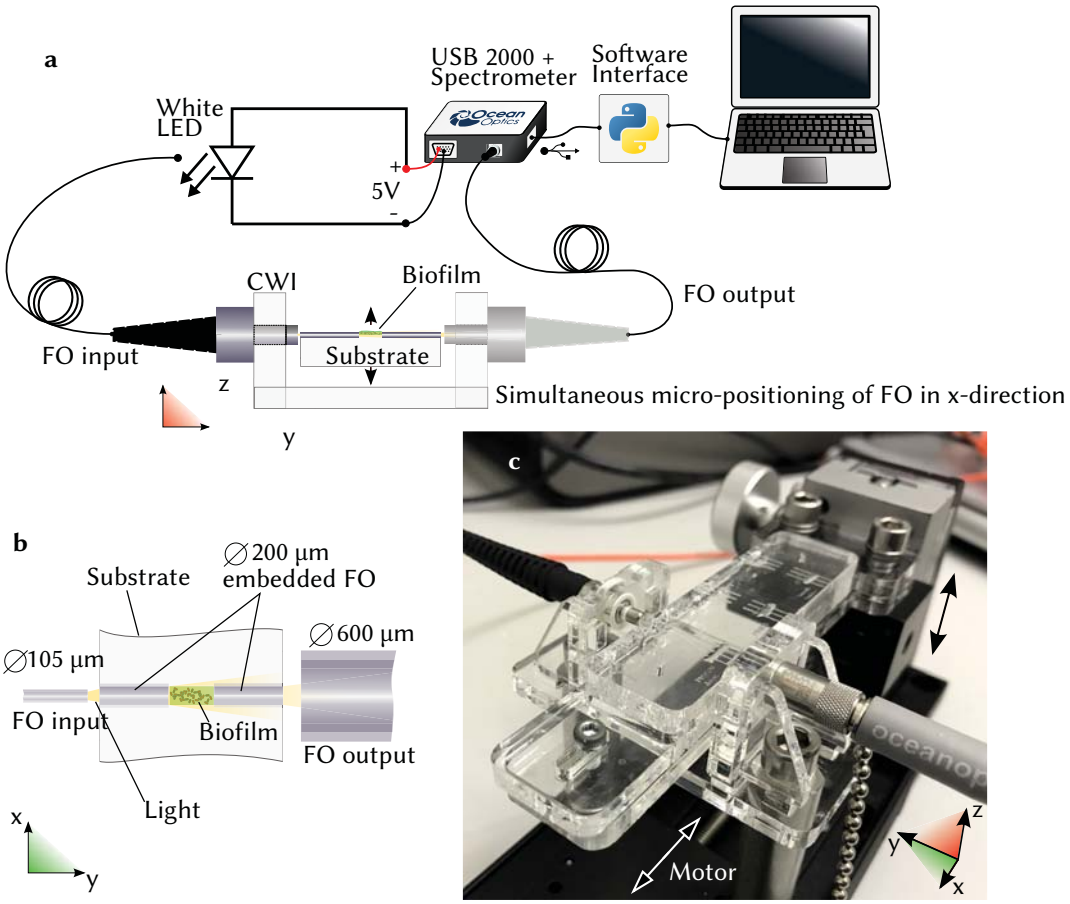

Figure 4.21: (a) Schematic of the experimental setup, specifying employed equipment. (b) Detail of embedded fibers in the laser-fabricated PMMA substrate for biofilm monitoring in static conditions, (c) Setup for robust fiber-optics coupling to and from the chip.

with 0.2% glucose (w/v) at 30°C in a thermal bath agitator. Overnight cultures were centrifuged and re-suspended in MMAB. The optical density of the final suspension was adjusted by dilution with deionised water to 1 absorbance unit (A.U.) at 550 nm with MMAB, which corresponded to a bacterial concentration around 10^8 colony forming units per mL (CFU/mL).

Setup The surface of the miniaturised device was immersed, with the surface of interest facing down, in a bacterial overnight culture under the same conditions as previously described. Here we used a strain of *E. coli* which exhibits autofluorescence when illuminated with UV light. This made it possible to do visual control using the same confocal micorscope as before, but without staining. Thus, the sample could be taken out of the culture medium, observed under the microscope, positioned on the CWI as indicated in Fig. 4.21 (c) for acquisition of the spectral response and returned to contact with the culture medium . For the optical measurements, the

experimental setup depicted in Fig.4.21 was employed. The Software interface indicated refers to the PythonSeabreeze based *MyOpticsLab* class introduced in section 3.3.3.

4.4.2 Results and discussion

The results of the optical measurements are shown in Fig. 4.22. Each plot corresponds to the average absorbance (compare eq. 1.11) of a triplicate measurement of $I(\lambda)$) performed at each of the three surface conditions and calculated with regard to their initial reference measurements $I_0(\lambda)$ acquired before immersing the surface into the bacterial culture medium for the first time. The respective surface conditions were as detailed previously and are indicated in the plot's title. According to the results in Fig. 4.22, after only 4 hours of incubation, the spectral response corresponding to the optimal surface condition $P05S20$, already shows the typical spectral behaviour of a suspension of scatterers with size-parameters close to 1 (compare Fig.D.2). At the other two interrogation sites, a similar pattern was only observed after 148 h.In all three cases, the scattering pattern was decreasing over time after its initial appearance, suggesting a reduction of refractive index contrast between isolated scatterers (e. g. bacteria in solution) and the surrounding medium, which can be assumed to be mainly extracellular substances during the late stages of biofilm formation, This is consistent with the cumulative secretion of extracellular substances like polysaccharides, which have refractive indexes far greater than that of water, thus greatly reducing the scattering efficiency (compare scattering efficiency for different refractive index contrasts in Fig.D.2).

On the other hand, several absorption bands were registered at wavelengths coinciding with the excitation and emission bands of the fluorescent protein the bacteria express (GFPmut3). Said protein features two excitation bands and two emission bands as indicated in Fig.4.22 as $\mathrm{GFP}_{Exc.1}$ at 472 nm, $\mathrm{GFP}_{Exc.2}$ at 501 nm, $\mathrm{GFP}_{Emis.1}$ at 511 nm and $\mathrm{GFP}_{Emis.2}$ at 545 nm, respectively. Although the positions of the absorption bands and the designated GFP peaks coincided, the tendency caused in the spectral response is only partially in concordance with the underlying physical effects. At 472 nm, a peak in absorbance would make sense, as the excitation of the protein implies an absorption of light at that wavelength. The two subsequent excitation and emission bands at 501 nm and 511 nm may, if detectable, counteract each other to some extent so as to not result in a pronounced peak. It should however be noted that emission is much less likely to be detected than absorption in a configuration like the present one measuring in transmission mode. Lastly, the broad absorbance band around 545 nm is completely counter intuitive in terms of the GFP emission. So, beyond the observation that specific absorbance bands have been registered in this configuration from biofilms from this particular strain of GFP-expressing

E. coli, we can draw no further conclusion based on the present results.

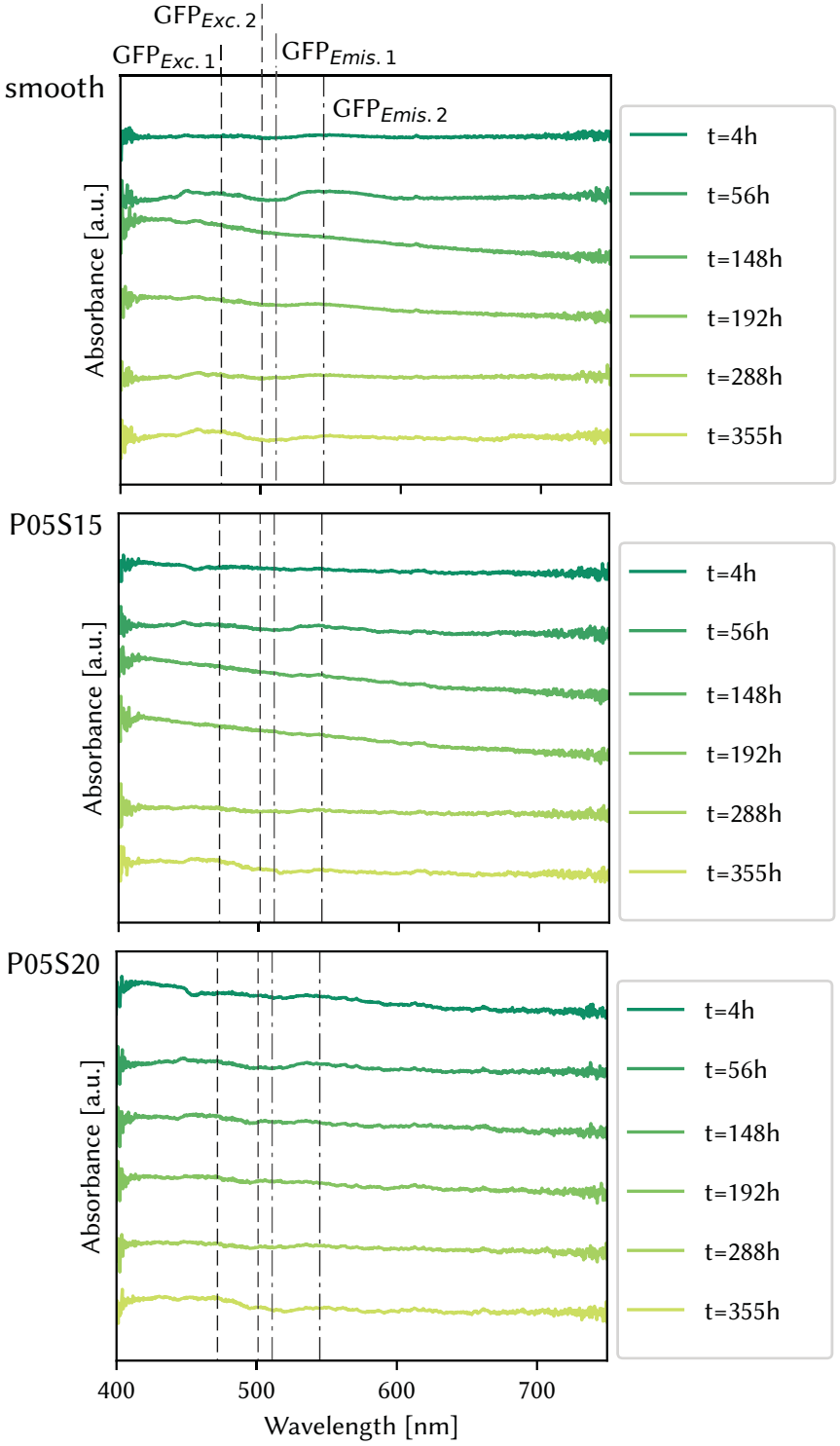

Figure 4.22: Spectral response according to surface modifications over time.

s